Università degli Studi Roma TRE

e

Consorzio Nazionale Interuniversitario per le Scienze Fisiche della Materia

Dottorato di Ricerca in Scienze Fisiche della Materia
XXV ciclo

Spin dynamics of Superparamagnetic Iron Oxide Nanoparticles investigated by Solid State NMR

Tesi di dottorato del dott. Lorenzo Bordonali

Relatore
Prof. Alessandro Lascialfari

Coordinatore Dottorato
Prof. Settimio Mobilio

a. a. 2012/2013

Contents

Introduction and overview of the thesis **5**

1 Static and dynamic properties of magnetic nanoparticles **11**
1.1 Chapter overview . . . 11
1.2 Presentation of ferrite nanoparticle samples and chemico-structural characterization . . . 12
1.3 Static magnetic characterization . . . 13
1.4 AC susceptibility on ferrite nanoparticles: interparticle interactions and spin-glass like phenomena . . . 25
1.5 Conclusions . . . 30

2 Size-dependent spin dynamics in iron oxide nanoparticles by ^{1}H-NMR **31**
2.1 Chapter overview . . . 31
2.2 Probing the dynamics . . . 32
2.3 ^{1}H-NMR and Mössbauer spectroscopy experiments on coated magnetic nanoparticles. . . . 34
2.3.1 ^{1}H-NMR Spectra . . . 35
2.3.2 Longitudinal spin-lattice nuclear relaxation rates. . . . 38
2.3.3 Theory of proton spin-lattice relaxation rates for coated superparamagnetic nanoparticles . . . 41
2.3.4 $1/T_1$ data analysis . . . 45
2.3.5 Mössbauer experiments on Sample **1** . . . 49
2.4 Conclusions . . . 53

3 Nanoparticle samples in solution: an NMRD investigation **55**
3.1 Chapter overview . . . 55
3.2 Magnetic nanoparticles in biomedicine . . . 56
3.3 Colloidal suspensions of Iron-oxide-based nanoparticles . . . 56
3.4 AC Susceptibility . . . 59
3.5 Longitudinal and transverse relaxivity measurements . . . 61
3.6 Proton relaxivity models and Roch's theory . . . 68
3.7 r_1 longitudinal relaxivity data analysis . . . 74
3.7.1 The role of size and magnetic anisotropy . . . 75
3.8 r_2 transversal relaxivity data analysis . . . 79
3.9 Conclusions . . . 82

4 Preliminary in-vivo tests with novel multi-functional magnetic nanoparticles **85**
4.1 Introduction 85
4.2 State of the art in brief 85
4.3 Experimental setup 86
4.4 Relaxometric measurements on 15_Block-M-PTX-FA 87
4.5 Experimental procedures 87

General Conclusions **95**

Appendices **99**
^{1}H-NMR study of the spin dynamics of fine superparamagnetic nanoparticles 99
Dependence of nuclear relaxation rates on composition and size in nearly monodispersed ferrite nanoparticles. 112
Redistribution of local spin density in Cr_7Ni antiferromagnetic molecular ring from ^{53}Cr-NMR 124

Publications **133**

Introduction and overview of the thesis

Assemblies of magnetic nanoparticles are model systems for the study of magnetism at the nanoscale. Due to their wide technological applications, primarily in magnetic recording media, the properties of fine and ultrafine magnetic particles have been intensively investigated since the late 1950s; after the pioneering theoretical study made by Stoner and Wohlfarth[1] on the magnetization reversal mechanism in single-domain particles, intensive theoretical and experimental work has been carried out.

Nowadays, nanoscale magnetic materials attract widespread interest because of novel effects arising from the reduction of their spatial extension. The study of this phenomenology has a major impact on modern magnetic storage technology[2, 3] as well as on the basic comprehension of magnetism on the mesoscopic scale [4, 5].

As first predicted by Frenkel and Dorfman [6] a particle of a ferromagnetic material is expected to consist of a single magnetic domain below a critical particle size. Rough estimates of the critical diameter have first been made by Kittel[7]: an approximate diameter of 30 nm is estimated for a spherical sample made of common ferro/ferrimagnetic materials, such as magnetite or maghemite. Such monodomain magnetic particles can be viewed as large magnetic units, each having a magnetic moment of thousands of Bohr magnetons.

In a system consisting of isolated, hence non-interacting, single domain particles, the magnetic moments of the particles act independently. They are characterized by the instability of the magnetization due to thermal agitation that results in the phenomenon of 'superparamagnetism', each particle behaving similarly to a paramagnetic atom with a giant magnetic moment $\mu_{SPM} \sim 10^3\mu_B$ – $10^5\mu_B$. Magnetization reversal can occur via coherent rotation of the magnetization vector from one magnetic easy axis to another along a magnetically hard direction. As a consequence of this rotation mechanism, the coercivities of magnetic nanoparticles lie between those of soft magnetic materials and normal permanent magnet materials. This unique property to control coercivity in such magnetic nano-materials has led to a number of significant technological advances, particularly in the field of information storage. Small magnetic particles are promising candidates to further increase the density of magnetic storage devices over the 16 Gbit/cm^2 limit, possibly reaching 1 Tbit/cm^2[8].

Although in an ensemble of isolated particles direct exchange may be neglected, magnetic properties are often determined by the dipolar field energy, along with the thermal and magnetic anisotropy energies[9]. At sufficiently high

packing densities, e.g. in a powder sample, the interparticle interactions have profound effects on the dynamic properties of the assembly. Firstly, they modify the energy barrier arising from the anisotropy contributions of each particle. In this case individual priority is given to the total free energy of the assembly, while single particle energy barriers are no longer solely relevant. Secondly, interparticle couplings may produce a low temperature collective behavior that is completely different from the individual blocked one. The collective state sometimes shares most of the characteristics of magnetic spin-glass-like behavior [10, 11, 12, 13]. To further complicate this scenario, one must take into account what happens at the surface of a magnetic particle: Ref. [14] and [15], for instance, discuss the role of the spin canting phenomena on the particle surface, due to the lower degree of coordination of the Fe sites. This disordered state can extend deep into the particle volume and, in the smaller particles, may cover the whole nanocrystal[16]. Characterization of the surface state is still matter of intense experimental investigation and debate.

Apart from data storage, magnetic nanoparticles show a lot of potential for other applications, such as ferrofluids[17], high-frequency electronics[18], high performance permanent magnets[19], and magnetic refrigerants[20]. Also, magnetic particles are currently successfully employed in biology and medical sciences as drug-targeting agents, for cancer therapy and Magnetic Resonance Imaging (MRI). MRI is nowadays widely applied to scan many vital organs including the heart and the brain. However, MRI with conventional contrast agents lacks the sensitivity for scanning the very small tumors or even specific solid cancer cells inside the human body because of weaknesses in the therapeutic site targeting capability. Research has been focused on developing new contrast agents for MRI diagnosis in order to enhance the contrast of MRI images. Superparamagnetic nano-structured materials have been recognized as promising contrast agents for MRI because the large spin moment of magnetic particles heavily modifies the transverse nuclear relaxation time of water protons, and enhances the sensitivity of the MRI measurement. In addition, appropriate surface modification of the magnetic nanoparticle with suitable biologically active specific functional groups, such as monoclonal antibodies or proteins, increases the specificity of the MRI diagnosis. The quality of the particles used as MRI contrast agent is determined by the magnetic properties of the core material, particle size distribution and shape, particle surface charge, stability in aqueous solvents and chemical properties of the functional groups grafted on the surface. The latest results in this field can be found in recent reviews, such as Refs. [21] and [22].

On a more fundamental level, the solid-state-NMR study here presented on magnetic nanoparticles shares a number of similarities with Iron-based molecular magnets, to which the NMR technique has already been most proficuously applied: each molecular magnets is a free standing agent responding to external stimuli independently to the other molecules in the crystal because the inter-molecular magnetic couplings are by far negligible with respect to the intra-molecular interactions [23, 24]. Relevant results have been obtained on

iron-based molecular magnets such as Fe_6,[25] Fe_8,[26, 27] Fe_{10}[28] and Fe_{30}[29] where an enhancement in the nuclear-spin-lattice relaxation rates at low temperatures (10–30) K revealed a dynamic driven by the coupling of the paramagnetic ions with the acoustic phonons [30].

With respect to the nano/mesoscopic size of a typical magnetic nanoparticle, the relatively smaller number of spins contained in an iron cluster allows for a very precise evaluation of the magnetic phenomena on a quantum-mechanical level. Indeed, the experimental results obtained in molecular magnets can be compared with the prediction from theoretical calculations based on a model Hamiltonian, with low-dimension Hilbert spaces in virtue of the low number of the spin involved. However, the same approach is simply not feasible on a spin system such as that of a magnetic nanoparticle.

On the other hand, considering that the biggest iron-based molecular magnet contains 30 iron spins and that a spherical iron oxide nanoparticle of about 1nm may contain a variable number of about $10^2 - 10^3$ spins, it appears as a natural consequence that the study of very small iron based nanoparticles would be the next step for the research on molecular clusters and mesoscopic magnetism. The long term aim of the research is to bridge the gap in the knowledge of the magnetic phenomena between the smallest of the nanoparticles and the largest of the iron clusters[31]. Starting from this basic idea, the main objective of this work is the investigation of the spin dynamics of superparamagnetic (SPM) nanoparticle ensembles using monodispersed powder samples of organic-coated ferrite particles by resorting to Nuclear Magnetic Resonance. Probing of the local dynamics is made possible by the magnetic dipolar coupling between the superparamagnetic moment of the ferrite core and hydrogen nuclear spins (proton spins) in the organic material of the encapsulating shell. Thus, even though the chosen NMR probes do not sense each single Fe spin in the inorganic core on a true local level, the dynamic magnetic behavior of the nanoparticle as a whole can still be observed.

The importance of the here discussed investigation resides in its novelty, since a complete study of magnetic nanoparticles encompassing AC susceptibility, DC magnetometry, NMR solid-state spectroscopy, NMR relaxometry and Mössbauer spectroscopy has never been attempted. This multi-technique approach allows access to key parameters such as the Saturation magnetization M_S, the average magnetic anisotropy energy E_A and its distribution, the characteristic time for the electronic magnetization relaxation τ_0, and to information about interparticle interactions. Additionally, NMR relaxometry has been exploited to obtain the frequency dependence of r_1 and r_2 and an estimation of the diffusional correlation time τ_D, three quantities which are tightly related to the MRI efficiencies of the investigated materials. The interplay of these and other parameters have been evaluated and correlated with structural parameters, such as the magnetic ion species, the particle size and the particle topology. It should also be mentioned that we attempted to experimentally estimate the field dependence of τ_0 from AC and DC data, a necessary measurement when working at relatively high fields, which is however largely neglected in the liter-

ature and not usually performed. The work carried out in Pavia represents the very first attempt at studying the spin dynamics of magnetic nanocrystals as a function of temperature with NMR: an important goal was showing that an original NMR approach to the study of the dynamic properties of fine superparamagnetic particle is possible and that the NMR approach deserves the same consideration as other experimental techniques usually selected for this kind of investigation, e.g. Mössbauer spectroscopy, Ferromagnetic spectroscopy, and AC/DC magnetometry.

The fundamental physics involved in the phenomenology of magnetic nanoparticles is of great interest for the application of iron-oxide based nanoparticles as functionalizable MRI negative contrast agents. Indeed, the magnetic properties and the spin dynamics have to be investigated in order to reach a better understanding of the underlying physical mechanisms that cause the decrease in the relaxation time of water proton spins. In particular, the role of the magnetic anisotropy in determining the contrasting efficiency as a function of the static magnetic field needs to be defined. In order to study these aspect, relaxivity curves on a wide variety of samples were analysed: r_1 has been measured to validate a descriptive physical model upon which formulate practical considerations about the selection of a certain material and particle size to be used for synthesizing a superparamagnetic nanoparticle-based contrast agent; complementary r_2 relaxivity measurements have been carried out to actually quantify the nanoparticle systems as negative contrast agents.

Relying on the good results obtained in the fundamental research, and considering how the topology and the magnetic properties (τ_0, E_A, τ_D, M_S, etc ...) come together to confer good contrasting efficiency to a magnetic nanoparticle system, a candidate material has been envisioned, created and ultimately selected for preliminary in vivo tests in mice.

This thesis is divided in four chapters: the first chapter introduces the static and dynamic magnetic properties of four nanoparticle samples of diverse core sizes. The dependence of the blocking temperature and of the single particle magnetic anisotropy energy barrier distribution on the applied magnetic field is discussed. AC susceptibility data is also presented in Chapter 1; the AC technique allowed measurement of the effective magnetic anisotropy barrier, which was found in the range 600 – 1000 K. Given the very high values for the energy barrier in some of the samples, and the out-of-scale characteristic times $\tau_0 \sim 10^{-19} - 10^{-16}$ s/rad, the possibility of an emerging spin-glass like state in the smaller samples is critically evaluated at the end of Chapter 1.

Chapter 2 is dedicated to the presentation of the analysis of the nuclear spin lattice relaxation rates, as observed by NMR, with a simple heuristic model and the discussion of the results. The main reported result consists of the observation of a peak in the temperature dependence of $1/T_1$, which was found at $T \sim 25$K on the smaller particles ($\sim$ 4 nm) and at increasingly higher temperatures for the larger samples, 120 K for $d \sim 7$ nm and 280 K for $d \sim 12$ nm. Supporting data extracted from Mössbauer experiments on the smallest sample complete this chapter.

In Chapter 3 the most significant results of the systematic NMR relaxometric study on a selection of nanostructured samples are reported: adapting the NMR theory developed by Roch et al[32] to fit the experimental data, key parameters for the characterization of the relaxometric properties for a considerable number of samples were deduced. Transverse relaxivity r_2 levels of about 300 – 500 $s^{-1}mM^{-1}$ were achieved, i.e. 3 – 5 times higher than commercial nanoparticle-based contrast agents.

Then we proceeded to select a suitable sample for in-vivo experimentation among different investigated series of magnetite/maghemite coated samples, with the aim of obtaining a multifunctional particle featuring a high MRI contrast efficiency. This sample is part of the in-vivo trial test series within the scope of the european project 'Nanother' (EU-FP7). The preliminary in-vivo results are briefly reported in the fourth and last chapter of this thesis.

Further details about the experimental investigation of ferrite nanoparticles are reported in the Appendices, which include one published paper on ferrite-based nanoparticles and one submitted paper on the comparison of relaxivity curves of various nanoparticle systems. A paper on the spin configuration in the magnetic ground state of antiferromagnetic molecular magnets has also been appended due to the close affinity between the methodology adopted for the work presented in this thesis and the contents of the article. This paper is the final result of a side project that ran in parallel with the main line of research, and it was mainly developed by the author of this thesis and undergraduate student C. Casadei (University of Pavia), in collaboration with Dr. Furukawa of the Ames Laboratory, Iowa State University in Ames (IA), USA.

Chapter 1

Static and dynamic properties of magnetic nanoparticles

1.1 Chapter overview

The following chapter presents the iron-oxide-based nanoparticles samples selected for the investigation of the spin dynamics of superparamagnetic nanoparticles; the primary concern of the study featured in this thesis is the temperature and magnetic core size dependence of the spin dynamics, although the topology of the particle system and the chemical composition of the organic coating covering the nanoparticles may indeed play a role.

The results of the preliminary investigation of static and dynamic magnetic properties of the samples are discussed in the next paragraphs: static magnetic properties of the chosen materials need to be explored prior to a NMR investigation, to gain access to complimentary information about, for instance, the superparamagnetic blocking temperatures and the evolution of the energy barrier distribution with the field. Indeed, it is of primary importance for the success of this work, to make sure that the samples present a superparamagnetic behavior up to $H = 15$ kOe, which is the highest magnetic field employed in NMR experiments. This task is conveniently accomplished by measuring both the zero-field-cooled and field-cooled Magnetization versus Temperature curves at different applied fields, as well as Magnetic Hysteresis measurements.

AC susceptibility represents an additional, excellent tool for the understanding of low-frequency dynamics of the bulk material, possibly revealing emergent criticalities or collective phenomena. Furthermore, the extraction of the temperature dependence of the electronic magnetic moment relaxation time is of great value for the validation of the dynamics seen by NMR.

As it is shown at the end of this chapter, AC susceptibility measurements confirmed the presence of a spin-glass-like state in the studied magnetic nanoparticles at low temperatures, a phenomenon which is supposed to be caused by strong dipolar interactions between particles. Both static and dynamic analysis yielded valuable information to cast light on the effects of interparticle interactions within the solid-state powder samples.

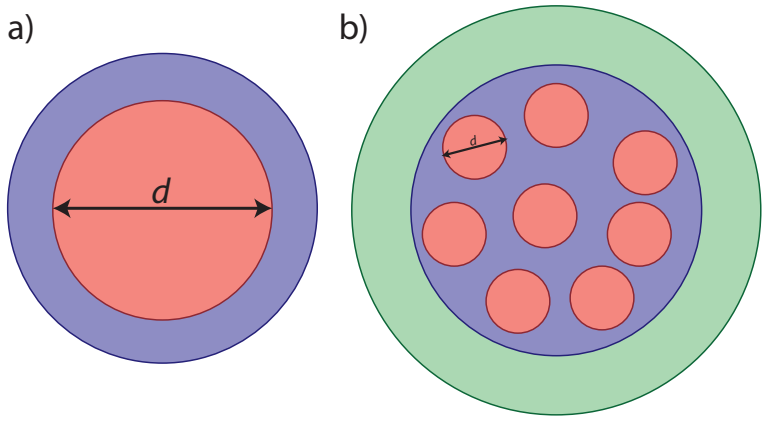

Figure 1.1 – Schematic drawing of sample particle geometry. a) Spherical configuration, with a central inorganic core and external organic shell. (Sample **1** and **3**) b) 'Bead'-like geometry: inorganic particles are first embedded in a polymeric matrix to form the bead, then the bead itself is coated with a suitable functionalizable organic compound. (Sample **2** and **4**)

1.2 Presentation of ferrite nanoparticle samples and chemico-structural characterization

In this chapter the characterization of four coated maghemite nanoparticle samples, selected to cover a size range between 3 and 12 nm, will be introduced:

- Sample **1**: maghemite nanoparticles of 3.5 nm in diameter, coated with Dextran.
- Sample **2**: maghemite nanoparticle of average size 4 nm have been employed to create Fe_3O_4@PEG@PVP beads. Each bead hosts a variable number of nanoparticles. Thus, sample **2** should be considered as a solid suspension of nanoparticles in a polymeric matrix.
- Sample **3**: this sample is composed of 7 nm maghemite nanoparticles coated with oleylamine.
- Sample **4**: 12.5 nm maghemite nanoparticles embedded in PEG@PVP beads. This sample has been synthesized following a route similar to sample **2**.

Details of the synthesis of the four samples can be found in references [33, 34] (Sample **1**), [35] (Sample **3**), and [36] (Sample **2** and **4**). The geometry of the particles is sketched out in Fig. 1.1. The first kind of capped nanoparticle is simply composed of a central inorganic magnetic core of a certain size, spherical in shape, coated with a layer of organic material whose thickness depends on the specific surfactant material (Fig. 1.1a). Sample **1** and **3** belong to this class.

Sample	d	δd	H_{coerc} at $T < T_B$	T_B
	nm	nm	Oe	K
1	2.8	0.5	1020	27
2	4.5	0.5	1482	18
3	7.4	1.0	230	65
4	12.7	3.8	460	195

Table 1.1 – Key parameters of interests for the four investigated samples. From left to right: d average particle diameters and standard deviation δd; Coercive field H_{coerc} in the completely-blocked regime, as extrapolated from the M vs H curves at $T = 5$ K; T_B, measured from the position in temperature of the maximum of the ZFC curve at the lowest applied field, $H = 50$ Oe (See section 1.3).

The basic unit of samples **2** and **4**, on the other hand, consists of an inner part formed by a single folded PVP chain entrapping the MNPs by N-Fe coordination bonds, and an outer shell of solvated PEG chains in a radial disposition (Fig. 1.1b). It is important to notice that, for the investigation of magnetic properties of the capped magnetic nanoparticles, the presence of an organic magnetically inert coating does not lead to any additional contribution to the relevant observables measured by bulk techniques, except for the influence of distance from magnetic cores, partly regulated by the organic part. Furthermore, the amount of organic material actually impacts on the strenght of the ^{1}H-NMR signal and on the width of the NMR spectra. In addition, interparticle distances may affect the strength of long-range dipolar couplings. Assuming tight packing in powders, the minimum interparticle distance corresponds to two times the coating thickness, i.e. 8 – 10 nm, while for the geometry of Fig. 1.1b the interparticle distance cannot be easily determined, although rough estimates yield an average of 3 – 5 nm. The employment of two different topologies has been dictated by sample availability and future studies should consider creating a single series of samples spanning the whole size range, possibly with an increased size resolution.

Key structural and magnetic parameters are collected in Table 1.1. Sample size distribution and TEM images are also reported in Fig. 1.2.

1.3 Static magnetic characterization

At thermodynamic equilibrium and in zero applied magnetic field, the total magnetization of a nanoparticle is directed as to minimize the anisotropy energy that, to the first order, is directly proportional to the particle volume. Directions that minimize the anisotropy energy are called anisotropy axis, or axis of easy magnetization. In the case of uniaxial anisotropy, the expression for the anisotropy energy is rather simple:

$$E_A(\theta) = KV \sin^2 \theta \tag{1.1}$$

where θ is the angle underlying the only anisotropy axis and the magnetization, K is the anisotropy constant and V is the particle volume. Thus, if no

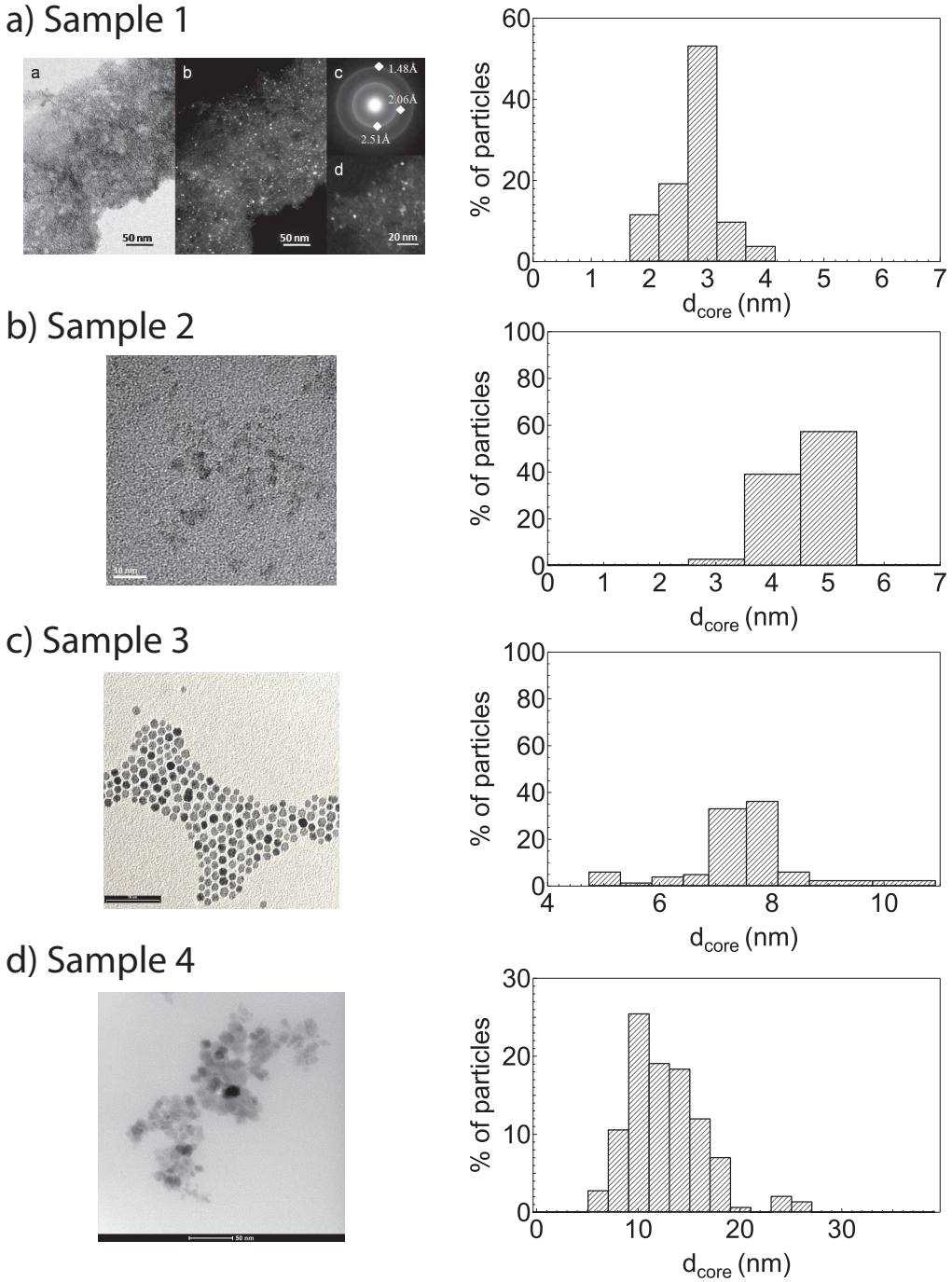

Figure 1.2 – TEM images and inorganic core size distributions for samples **1** – **4** (*a* to *d*). Samples are arranged from left to right, top to bottom, in order of increasing size. Particle size dispersion is limited and the relative error on the average particle size is bound between 15% and 30% for all samples. Aggregation and cluster formation is not observed in Samples **1**, **2** and **3**. The presence of some large cluster, however, might be the reason behind the higher dispersion observed in Sample **4**, although aggregates above 20 nm are limited to a nearly negligible amount.

magnetic field is applied and the temperature tends to zero, the only possible directions for the magnetization correspond to angles $\theta = 0$ and $\theta = 180$, i.e. the two symmetrical minima of eq. 1.1, separated by an energy barrier $E_B = KV$ (see Fig. 1.3a). The system is at the equilibrium when M lays along an axis of easy magnetization.

When an external magnetic field is applied, the field direction forming an angle ψ with the anisotropy axis. Then, equation 1.1 becomes:

$$E_A(\theta, \psi, \phi) = -KV \sin^2 \theta + HM_S(\cos\theta \sin\psi + \sin\theta \cos\psi \cos\phi) \tag{1.2}$$

where ϕ is the third polar coordinate of vector $\mathbf{M}$. Minimum of eq. 1.2 are now found when $\mathbf{M}$ is at an angle equal to $\psi - \theta$ with respect to field $\mathbf{H}$. This means that the magnetization is tilted toward the field. When the field is applied parallel to the anisotropy axis, the energy difference between the two energy minimum configuration takes the following phenomenological expression:

$$E_B(H) = E_B^0 \left(1 - \frac{H}{H_{inv}}\right)^{\frac{3}{2}} \tag{1.3}$$

As the field increases, the energy barrier decreases till the point of inversion, that is $H = H_{inv}$. At this point the barrier E_B is null and there is only one stable minimum in the angular dependence of the anisotropy energy. Figure 1.3b shows the effect of an applied magnetic field on the angular dependence of the magnetic anisotropy energy; two cases are displayed, one corresponds to the field being parallel to the main anisotropy axis (top) while the other one assumes the field perpendicular to the anisotropy axis. For both cases the activation energy barrier is bound to disappear when $H > H_{inv}$.

One of the most recognized models describing the coherent rotation of magnetization for an assembly of non-interacting single domain magnetic nanoparticles with uniaxial anisotropy is the Stoner-Wohlfarth theory.

This model describes the magnetic behavior of single particles by assuming classical single giant spin and certain magnetic anisotropies. According to this model the hysteresis cycle of a single particle critically depends on the angle between the applied field and the anisotropy axis.

If the particle anisotropy axis is perpendicular to the direction of the applied field the branches of the hysteresis cycle are superimposed, and there is no coercive field H_C and no remanence magnetization. If the particle axis is instead parallel to the applied field, the hysteresis cycle is a square and the coercive field is equal to $H_C = 2K/\mu_0 M_S$. At intermediate angles hysteresis cycles feature a coercive field and remanence magnetization that span between these two extreme positions. Also, for an assembly of randomly oriented, non interacting particles all the discontinuities in the hysteresis curve will be smoothed out.

A collection of hysteresis cycles for the investigated samples is presented in Figure 1.4. At room temperature all samples are in the unblocked regime, since the magnetization curves show no hysteresis, thus the coercive field is zero and there is no remanence magnetization. At 2K, on the other hand, the M vs H

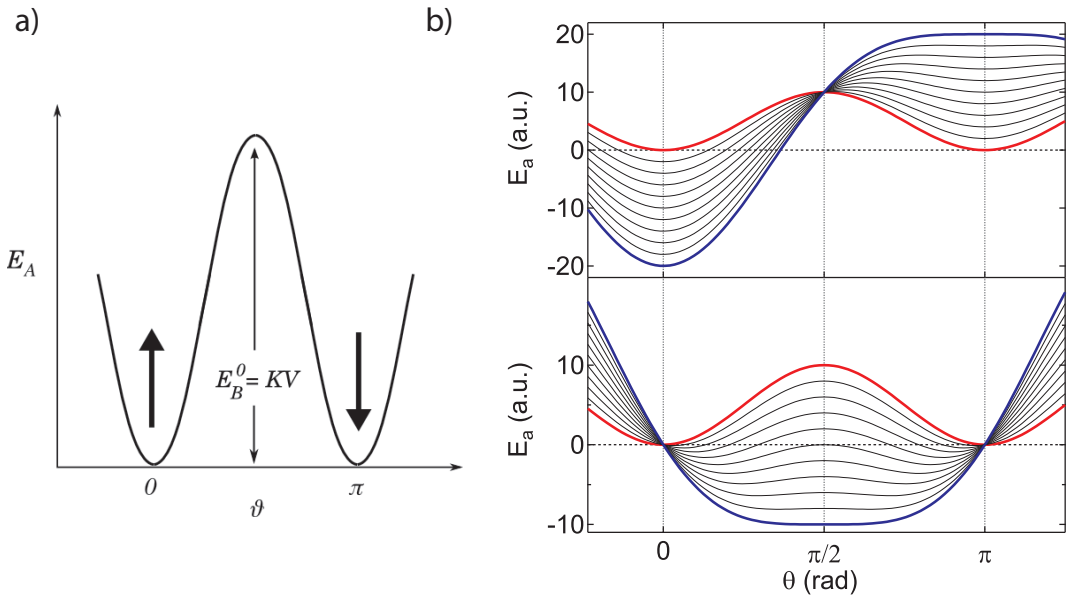

Figure 1.3 – a) Anisotropy energy E_b versus θ, the angle between the anisotropy axis and the magnetization in the case of uniaxial anisotropy (see Eq. 1.1). The two minima correspond to the two possible configuration of the magnetization along the anisotropy axis; they are separated by an energy barrier $E_B = E_B^0 = KV$. b) Angular dependence of the anisotropy energy in the case of applied magnetic field in parallel (top) and perpendicular (bottom) configurations. Red and blue thick lines correspond to $H = 0$ and $H = H_{inv}$ field values. Plots of Eq. 1.3 corresponding to intermediate fields, $0 < H < H_{inv}$, are drawn as thin black curves.

loop opens. An important striking feature of the measured loops is that the magnetization does not reach saturation even at $T = 2$ K and up to $H = 50$ kOe. Such unsaturated hysteresis cycle was observed in samples **1**, **2** and **4**, while sample **3** does not seem to be affected. In the former cases, the saturation magnetization values, M_S, are usually estimated from a fit over the high field data to the empirical formula[37]:

$$M = M_S + \frac{a}{H} + \frac{b}{H^2} \tag{1.4}$$

The non-saturation of the magnetization in the high field range can be tentatively interpreted by considering the presence of surface effects. Indeed, when the particles are particularly small, surface spins are difficult to orient and large field strengths are required to achieve a constant saturation value[38]. This is most noticeable in the smaller samples, sample **1** and **2**, because of the high surface to volume ratio. The presence of blocked particles even at very high field is further confirmed by a measurement of the zero-field-cooled and field-cooled magnetization, as explained in the following section.

For small particles at high temperatures the anisotropy energy becomes comparable to or smaller than the thermal energy. The magnetization will then fluctuate between the two energy minima with a characteristic reversal time that is given by the Néel-Brown expression:

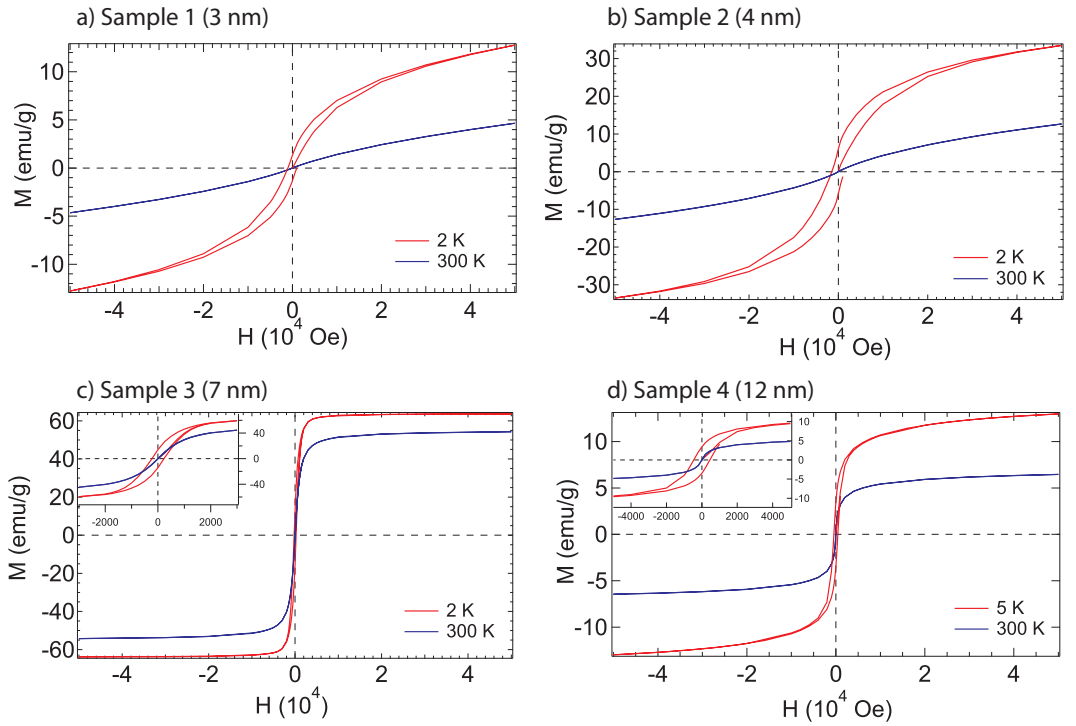

Figure 1.4 – Hysteresis M vs H measurements on ferrite nanoparticle samples, in the field range $-50 < H < 50$ kOe. Two temperatures are reported, 300K and 2K, to show the different behavior of the hysteresis loops in the unblocked and blocked regimes. All samples are blocked at the lowest temperature, as witnessed by an open hysteretic loop. Also, all samples are unblocked at room temperature and the reversible hysteresis cycle, typical of paramagnet is observed. Non-saturation of the magnetization is clearly visible at fields $H >\sim 30$ kOe for samples **1**, **2** and **4**. Magnified plots near $(M, H) = (0, 0)$ are included as insets for samples **3** and **4**.

$$\tau = \tau_0 e^{\left(\frac{K_{eff}V}{k_B T}\right)} \tag{1.5}$$

where K_{eff} is the effective magnetic anisotropy of the particle, k_B is Boltzmann's constant and the 'attempt time' τ_0 usually falls in the range $10^{-10}-10^{-12}$ typical of non-interacting superparamagnetic particles.

Deviations from this range, also accompanied by anomalous values for $K_{eff}V$ are commonly found in concentrated solutions or solid samples, where interparticle interactions are sizeable. Under such circumstance, a phenomenological Vogel-Fulcher law better suits the case:

$$\tau = \tau_0 e^{\left(\frac{K_{eff}V}{k_B(T-T_0)}\right)} \tag{1.6}$$

Parameter T_0 accounts for the effects of any particle-particle interaction.

Fluctuations of the magnetization slow down (i.e. the reversal time τ increases) as the sample is cooled to lower temperatures and the system appears static when τ becomes much longer than the experimental measuring time of the probe τ_m. When $\tau \sim \tau_m$ the particle is said to be blocked. Conversely,

in the unblocked regime, when $\tau < \tau_m$, the experimental setup is not able to resolve the fluctuations of the magnetization, yielding a zero averaged magnetization as a result. The transition between the blocked and unblocked regimes is characterized by the so-called 'blocking temperature', T_B, below which the superparamagnetic moments appear frozen on the time scale of the measurement. Thus, T_B is defined as the temperature at which the equality $\tau = \tau_m$ holds true, generally extracted from DC magnetization measurements that typically have $\tau_m \sim 1 - 10^2$ s.

The experimental measuring time τ_m is in the range $10^{-6} - 10^{-3}$ s for NMR (comparable to the inverse of the nuclear Larmor frequency), $10^{-10} - 10^{-7}$ s for Mössbauer spectroscopy (comparable to the decay time of the nuclear Mössbauer transitions), $10^{-10} - 10^{-4}$ s for μSR (a measurable fraction of muons live for up to $10\tau_\mu$ where $\tau_\mu = 2.2$ ms is the average muon lifetime), while AC susceptibility typically probes the interval $10^{-5} - 10^{-1}$ s and DC magnetometry, being a static technique, covers the range $1 - 10^2$ s.

From Eq. 1.5 it follows:

$$T_B \approx \frac{K_{eff}V}{k_B} \ln \frac{\tau_m}{\tau_0} \tag{1.7}$$

Equation 1.7 is valid for individual particles or for a system of non-interacting particles with the same size and anisotropy, and assuming the basic Stoner-Wohlfarth theory[1], according to which the spins of atoms forming a nanoparticle rotate coherently. To this respect, it must be stressed that even when a nanoparticle has a defect-free crystal structure, the different local environments of atoms located at the particle boundary and those inside the particle result in a nonuniform magnetisation and distortion of the perfect collinear magnetic structure[39, 14]. Numerical calculations have shown that magnetisation decreases along the particle radius, starting from the center and moving toward the boundary[40]. Also, the magnetic moment of each surface magnetic ion can be greater than that of the bulk atoms[41]. The increase in the magnetic moment of surface ions can be attributed, within the framework of the band theory, to the decrease in the coordination number, to the narrowing of the corresponding energy band and to the increase in the density of states. On the other hand, the decrease in the magnetisation on the particle surface compared to the bulk is due to the lower energy of surface spin wave excitations[42]; overall, this effect can be seen as a consequence of thermal spin fluctuations being more pronounced at the surface.

Now, remaining in the framework of the Stoner-Wohlfarth theory, if the particles are not monodispersed and/or interact with each other, the distribution of particle sizes results in a distribution of blocking temperatures. Thus, polydispersity leads to a complex behavior of the whole system, already in the border case of strong dilution. For these reasons, the sharp features to expected in the M vs. T curves at T_B become smeared. Moreover, for a system consisting of single-domain nanoparticles with a size, shape, etc. dispersion, the magnetization curves do not split at $T = T_B$ but at a higher point in tem-

perature $T_{irr} > T_B$, called the irreversibility point[43]. Another characteristic feature of the ZFC curve is the temperature of its maximum, T_{max}, which could be identified as the average blocking temperature $\langle T_B \rangle$. An increase in the FC curve is observed below $\langle T_B \rangle$ and then the curve reaches saturation at the lowest temperatures, although in some cases a maximum can also be observed [4]. The T_{irr} value can be identified with the blocking temperature for the largest particle.

To this date there is no highly affordable method for a precise and reliable estimation of the energy barrier distribution (from now on 'EBD'), especially in solid samples, where the presence of non-negligible interparticle interactions complicate the scenario even further. For instance, Monte Carlo simulations by Iglesias *et al.*[44] have shown that for weakly interacting systems the energy barriers relevant to the observation time window decrease with increasing interaction strength and the same behavior is expected for T_B (see also Ref. [4]). When interparticle interactions are strong enough to dominate over the disorder induced by the distribution of anisotropy axis, the EBD broadens toward higher energies as the interaction strength increases. Consequently, an increase in K_{eff} and T_B is expected.

On a general standpoint, even on quasi-monodispersed samples the evaluation of simple magnetic parameters, such as T_B or K_{eff}, is complicated by the number of relationships between the parameters that come into play when a magnetic measurement is performed. For instance: a) the initial moment $M_{ZFC}(0)$ is proportional to V and inversely proportional to K_{eff}; b) the blocking temperature and the temperature of the ZFC peak, T_{max} are proportional to K_{eff} and V; c) the width of the ZFC peak increases linearly with T_{max} and T_B, and is then proportional to both K_{eff} and V; d) the amplitude of the ZFC peak is proportional to V and inversely proportional to K_{eff}. e) The amplitude of the SQUID signal in the superparamagnetic regime is proportional to V^2.

It is then quite clear that the experimental profile of the ZFC/FC curves will strongly depend in a complicated way on the size distribution. The analysis of the ZFC curves is based on the assumption that the magnetic moment at temperature T follows this approximated expression [45]:

$$M_{ZFC}(T) = M_b e^{-\nu \delta t} + M_{eq}(1 - e^{-\nu \delta t}) \tag{1.8}$$

where ν is the particle's macrospin relaxation frequency at temperature T and δt is the effective measurement time related to the temperature sweeping rate selected for the experimental acquisition. M_b and M_{eq} are the values for the magnetic moment in the limit cases of low temperature ($M_{ZFC} = M_b$, blocked regime) and high temperature ($M_{ZFC} = M_{eq}$, superparamagnetic equilibrium):

$$M_b = \frac{\mu_0 H M_S^2 V}{3K_{eff}} \quad \text{and} \quad M_{eq} = \frac{\mu_0 H M_S^2 V^2}{3k_B T} \tag{1.9}$$

A particle of volume V will be in the blocked state as long as T is lower than the blocking temperature $T_B(V)$. This means that if a sample is characterized

by a size distribution $\rho(V)$, at a given temperature T all particles with a volume grater than a certain limit volume V_{lim} will be blocked while the smaller particles will be in the superparamagnetic state. The threshold volume, however, also depends on the temperature in a non-straightforward way. It can be shown that the following approximated expression holds[45]:

$$V_{lim} = \frac{\gamma k_B T}{K_{eff}} \quad \text{with} \quad \gamma \simeq 0.9609 \ln\left(\frac{\nu_0 T}{\nu_T}\right) - 1.629 \tag{1.10}$$

where ν_0 is an 'attempt frequency' of the order of 10^9 - 10^{11} Hz. It is then possible to express the equation for the M_{ZFC} as a function of the main parameters affecting the measurement:

$$M_{ZFC} = \frac{\mu_0 H M_S^2}{3k_B T} \int_0^{V_{lim}} V^2 \rho(V) \mathrm{d}V + \frac{\mu_0 H M_S^2}{3K_{eff}} \int_{V_{lim}}^{\infty} V \rho(V) \mathrm{d}V \tag{1.11}$$

$$M_{ZFC} = \frac{\mu_0 H M_S^2 k_B}{3K_{eff}^2} \left(\frac{1}{T} \int_0^{E_{lim}} E_B^2 \rho(E_B) \mathrm{d}E_B + \int_{E_{lim}}^{\infty} E_B \rho(E_B) \mathrm{d}E_B\right) \tag{1.12}$$

$$\rho(E_B) = \frac{1}{E_B \sqrt{2\pi\sigma^2}} e^{-\frac{(\ln E_B - \mu)^2}{2\sigma^2}} \tag{1.13}$$

The first contribution to Eq. 1.11 takes care of the superparamagnetic particles ($V < V_{lim}$) while the second contribution corresponds to the blocked ones. Equation 1.12 descends from Eq. 1.11 if the substitution $E = VK_{eff}$ is applied. Such substitutions allows to express the distribution of volumes $\rho(V)$ as the corresponding distribution of activation energy barriers $\rho(E_B)$.

ZFC magnetization curves for each sample were fitted to equation Eq. 1.12 and assuming a lognormal distribution of particle sizes with mean value $\bar{V}$ and width δ, which is the most common distribution encountered in the real experimental work. The corresponding distribution of activation energies is here presented as Eq. 1.13.

Since the NMR investigation requires fairly high fields, we first checked that the existence of a maximum in the ZFC curve still existed when NMR fields are applied to the sample. This is necessary since the application of a magnetic field has a huge impact on the EBD. Indeed, the Zeeman interaction actually decreases the magnetic anisotropy energy barrier, thus facilitating the magnetization relaxation when the particle is in the unblocked state. The effect is schematically reproduced in Fig. 1.3b: the two energy absolute minima that correspond to the possible equilibrium positions of the particle magnetic moment are tilted vertically on the energy scale so that one minimum is found to be lower than the other one, biasing the relaxation of the particle magnetization toward the co-parallel configuration of the magnetic moment with respect to the applied field. Although it would seem that both the barrier and the blocking temperature should tend to 0 as the Zeeman energy overcomes the largest single particle magnetic anisotropy energy, Monte Carlo simulations [46] and actual

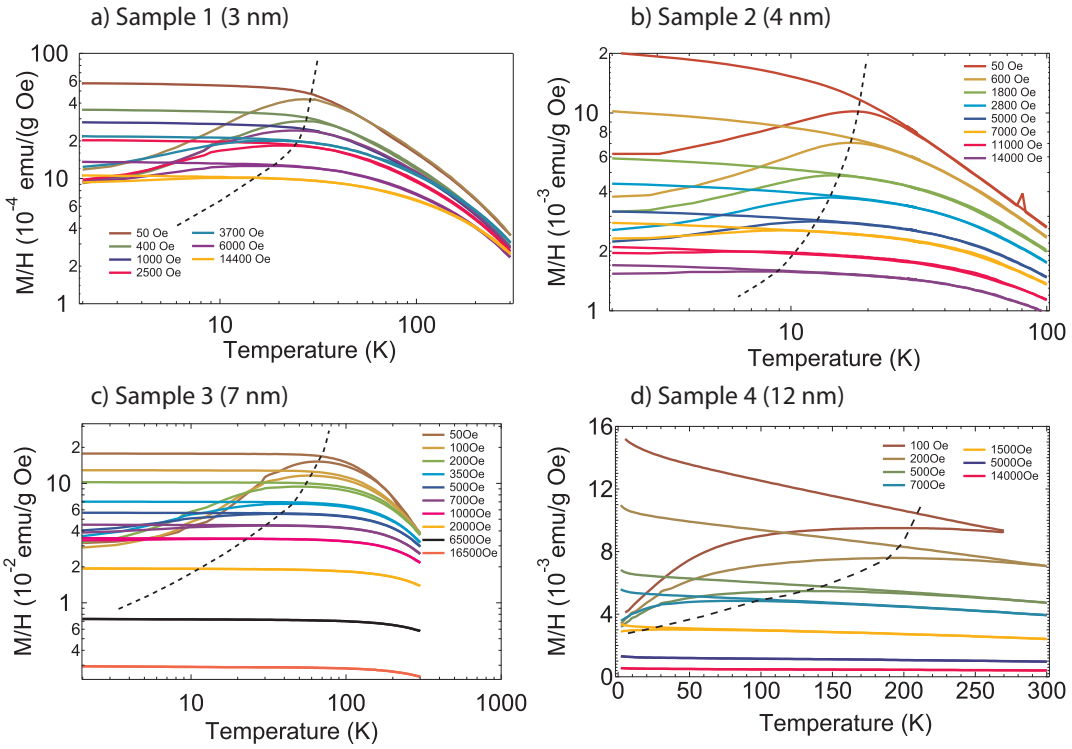

Figure 1.5 – M/H as a function of temperature, ZFC/FC curves for samples **1** – **4** (*a* to *d*). The log-log plot was chosen for a better visualization of the data. A peak in the ZFC curve can be observed even at high field values. The dashed thick line is a guide to the eye, showing the shift of the maximum in the ZFC curve toward lower temperatures when increasing the external magnetic field. Refer to Fig. 1.6 for an example of ZFC/FC curves analysis.

experiments show that the a blocking temperature can be defined even at very high fields.

In a dispersed sample the effect of the magnetic field translates to a modification of the EBD, leading to a decrease of $K_{eff}V$ to lower values. Moreover, the distribution at $H = 0$ splits into more subdistributions, reaching both higher and lower energy values, as H is increased [47]; as a consequence, results from a fitting routine with Eq. 1.11 are especially accurate when the applied field H is low, i.e. below 10^3 Oe. On this respect, it has to be noted that no direct dependence of the effective magnetic anisotropy on the applied field is present in Eq. 1.11; for this reason it was assumed that any effect due to the field would produce a modification of the EBD itself. The most critical approximation in the whole procedure is the assumption that at any time and condition, the EBD can be described by a lognormal function. Even though it would be of great interest to the static and dynamic characterization of magnetic nanoparticle ensembles in static fields, the development of a generalized and comprehensive form for the EBD that solves the inverse problem goes well beyond the scope of the present investigation.

ZFC/FC curves measured at different applied magnetic fields are reported in Fig. 1.5: the superparamagnetic character of all samples is revealed by

Sample ***1*** (3nm)

H	μ	σ	$\bar{E}$	δE
Oe	-	-	K	K
50	5.59	0.60	318.54	208.02
400	5.41	0.70	285.67	228.72
1000	4.98	0.87	211.89	225.77
2500	4.15	1.16	124.34	210.22
3700	3.64	1.31	89.22	189.51
6000	2.29	1.67	39.92	155.98
14400	-0.36	2.24	8.63	106.10

Sample ***2*** (4nm)

H	μ	σ	$\bar{E}$	δE
Oe	-	-	K	K
50	5.24	0.55	199.75	130.15
600	4.84	0.77	141.88	152.65
1800	3.91	1.13	64.55	152.24
2800	3.51	1.28	46.41	153.22
5000	2.40	1.57	18.02	124.17
7000	0.83	1.90	4.74	84.35

Sample ***3*** (7nm)

H	μ	σ	$\bar{E}$	δE
Oe	-	-	K	K
50	6.32	0.73	728.63	611.84
100	5.64	0.99	458.99	593.15
200	4.63	1.33	246.57	539.50
350	2.90	1.81	92.79	463.98
500	1.57	2.08	41.79	361.57

Sample ***4*** (12nm)

H	μ	σ	$\bar{E}$	δE
Oe	-	-	K	K
100	6.06	1.30	1002.61	2109.43
200	5.86	1.35	871.78	1988.73
500	5.63	1.33	678.97	1499.89
700	4.09	1.68	246.67	983.67

Table 1.2 – Fit parameters relative to the data fit of $\chi_{DC,ZFC}(T)$ to Eq. 1.11 for all samples. From left to right: applied magnetic field$H$; μ and σ parameters of the lognormal distribution; average barrier value $\bar{E}$ extracted from the distribution and standard deviation δE.

the observed maximum in the ZFC curve while the FC curve saturates at the lowest temperature. The difference between ZFC and FC curves is primarily due to the magnetic moment being oriented by an applied field when lowering the temperature while the field is active. Conversely, raising the temperature after a zero applied field cooling allows the nanoparticles magnetic moment to gradually un-block, reaching the (super)paramagnetic regime, right after the maximum in the ZFC curve. Indeed both ZFC and FC curves exhibit the same Curie-like trend for $T > T_{max}$.

Fits to eq. 1.11 in the ZFC peak region and the extracted lognormal energy barriers only for the exemplary case of sample **1**, are shown in Fig. 1.6 a) and b), respectively. $\nu_T = 0.033$ has been assumed, which corresponds to the experimental temperature sweeping rate of 2 K/s, and fixed parameter ν_0 to 10^{10}. Parameters of the lognormal distribution, μ and σ, are listed in Table 1.2, along with the average energy barrier $\bar{E}$ and standard deviation δE. The effect of the application of a magnetic field is that of moving the average barrier toward lower energies, meanwhile spreading the higher energy contributions on a broader range. The peak in the ZFC curve for samples **3** and **4** disappears when the field is raised above $\sim$ 1000 Oe, because all contributions to the energy barriers are suppressed by the field. For this reason it was not possible to fit the complete data set to eq. 1.11 for these two samples.

A comparison with the few results found in literature can be attempted, on the basis of the excellent results of the static magnetic investigation: it is

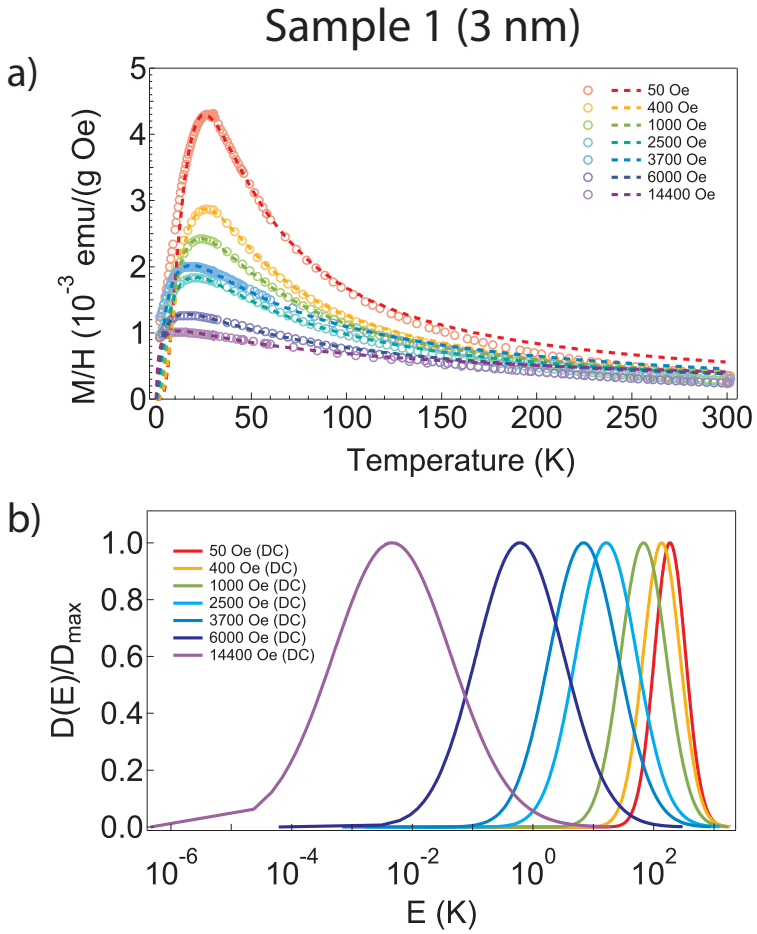

Figure 1.6 – (a) Best-fit curves of the ZFC M/H curves of Sample **1**, obtained from the fit to Eq. 1.11. (b) Calculated anisotropy energy barrier distributions for sample **1**. Each curve is a log-normal distribution normalized to its peak value, to better illustrate the evolution of the distribution as a function of the applied field.

possible to describe the evolution of the blocking temperature, estimated as the maximum of the ZFC curves, with the value of the applied field by resorting to a power law dependence of the form

$$H^{3/2} \propto (1 - T_B/T_0), \tag{1.14}$$

where T_0 represents the blocking temperature at, or near, zero field. This dependence holds true only up to a certain critical field H_T, above which the dependence on the reduced parameter $1 - T_B/T_0$ deviates from linearity. Some authors [48, 49, 50, 42] speculate that the behavior observed in the region $H < H_T$ corresponds to the so called the *de Almeida-Thouless* line[51], which is a characteristic feature found in many magnetic glassy phases[52]. However, in pure superparamagnetic systems, it has been demonstrated by numerical calculation of Brown's equation for the magnetization relaxation time[53] that a similar dependence also holds true.

Figure 1.7 reports, for all four samples, the applied magnetic field to the power of 2/3 as a function of the scale parameter $1 - T_B/T_0$, to illustrate the

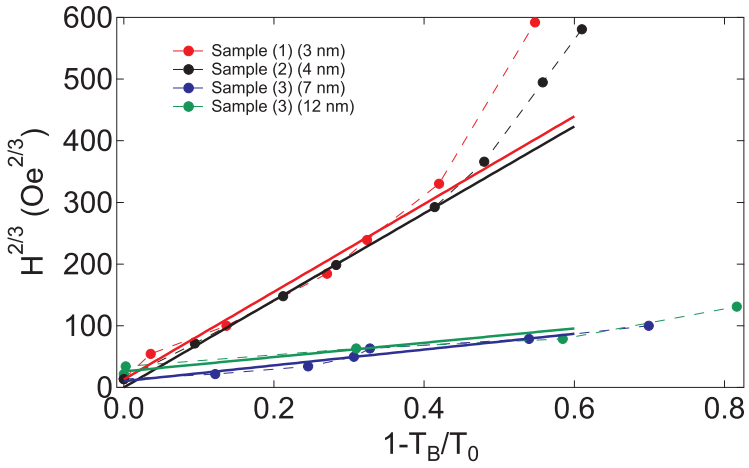

Figure 1.7 – Field dependence of the blocking temperature T_B for all investigated samples. The X-axis reports the scale parameter $1 - T_B/T_0$ where T_B is the estimate for the blocking temperature at a certain field, while T_0 is the blocking temperature at zero applied field. The solid lines are best fits to the power law $H^{2/3} = H_0(1 - T_B/T_0)$ for $H < H_T$ (the critical field where the plotted points deviate from linearity), showing the *de Almeida-Thouless* line.

described behavior: for low strenght of the applied field the dependence of the plotted parameters is linear, in agreement with expression 1.14; over the critical field H_T there is an abrupt change in the trend of the blocking temperature, corresponding to the transition to a regime where the applied field energy $\mu_S H_T$, μ_S being the total superparamagnetic moment of the particle, is comparable to the average single particle anisotropy energy barrier. In this regime the particle moment is more susceptible to be unblocked, thus the blocking temperature decreases more rapidly with increasing field.

For free, non interacting fine particles, e. g. in a diluted ferrofluid, H_T sets around 150 Oe. However, due to the powder form of the investigated samples, the experienced H_T is quite greater than 150 Oe. In the case of sample **1** and sample **2** $H_T =\sim 3000$ Oe, while for the other samples the critical field seems to never be met, suggesting once more that there are sizable inter-particle dipolar interactions acting inside the samples with core diameters $d > 4 - 5$ nm. In presence of interparticle interactions, the qualitative picture of the behavior of a system of magnetic nanoparticles following a decrease in temperature may become more complicated than the mere transition to the blocked state[54]. The possible transitions, at a given measurement time τ_m, are shown in Fig. 1.8[4]: when the interactions are active, the regime is superparamagnetic if the relaxation of a given particle is governed by its own activation barrier, eventually modified by the interactions. Instead, a collective state will emerge if it is not possible to define an activation barrier for each particle, but only a barrier relative to the assembly. Since the blocking temperature T_B decreases with increasing iteractions, a number of states should be observed with decreasing temperature, only below a critical interaction strenght: paramagnetic, superparamagnetic, blocked and collective states. Above this critical point the

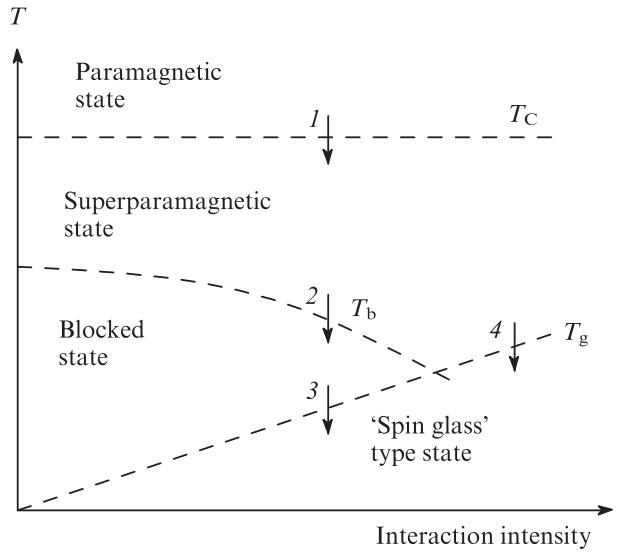

Figure 1.8 – This 'Temperature *vs* Interaction intensity' plot shows all possible phase transitions in a system of randomly arranged magnetic nanoparticles, taking into account interparticle interactions. (1) Transition from the paramagnetic to superparamagnetic state within single particles; (2) transition from the superparamagnetic into blocked state; (3)transition from the blocked state into a spin-glass-like state (superspin-glass); (4) transition from the superparamagnetic state to a spin-glass-like state.

blocked state should be suppressed and a transition from superparamagnetism to a collective state would occur.

Indeed, if the particles are irregularly arranged in space, interparticle interactions should transfer the system into the 'spin-glass-like' type state at some temperature T_g.[54] Which of the two temperatures, either T_g or the average blocking temperature $\langle T_B \rangle$ would be higher for the given type of particles depends on the particle size and on the average distance between them. Since the temperature dependence of the magnetic moment for a system of non-interacting particles and for a 'spin glass' is similar[55], determination of the nature of the transition is a non-trivial task.

The evaluation of a possible superspin-glass state is further discussed in the next paragraph about AC susceptibility data analysis.

1.4 AC susceptibility on ferrite nanoparticles: interparticle interactions and spin-glass like phenomena

Magnetic interparticle couplings have a significant effect on the magnetic properties of a nanoparticle assembly. Most notably, the energy barrier E_B, which depends on the symmetry of the magnetic anisotropy tensor of the single particle, is modified[42]. In such a circumstance, the total free energy of the assembly as a whole becomes relevant, while the single particle energy barriers are no

longer important by themselves. This means that the reversal of one particle moment may change all energy barriers within the assembly.

Interparticle interactions are only negligible in very diluted solutions while concentrated solutions and powder samples are all affected at a certain extent. For instance, assuming a magnetic dipolar interaction between two particles, each with a magnetic moment $\mu = 3000\mu_B$ and at a distance $D = 6$ nm, the mean point dipolar energy will be $E_{d-d}/k_B = (\mu_0/4\pi k_B)\mu^2/D^3 = 26$K. Taking also into account all neighbors, the mean dipolar energy could assume values around 100K in a dense packing. High-order multipole terms can also become relevant in the case of imperfectly spherical particles[56], and can eventually dominate over single particle blocking, leading to a collective freezing [4, 11, 42, 13, 57]. Superspin glass-like behavior has been observed in many nanoparticle systems with intermediate strength of dipolar interactions: here the superspins of the nanoparticles freeze collectively into a spin-glass-like phase below a critical temperature T_g[12, 58, 59].

Spin glasses typically show a divergence of the non-linear part of the susceptibility at the temperature T_g or aging and memory effects at $T < T_g$ [52, 60]. All of these features cannot occur in superparamagnetic, strongly diluted nanoparticle systems, in which the interaction of the particles can be neglected. This holds true even if non-negligible interparticle interactions of dipolar origin are presents. In the latter case the nanoparticle system also reveals a marked change in both the relaxation times of the electronic magnetization and the activation energies [4].

The superspin-glass state has been proposed by some authors [49, 13] to account for the dynamics observed by AC susceptibility in ferro- and ferrimagnetic nanoparticles of diverse sizes; the interpretation of such dynamics, however, is rather difficult, because the observation of a spin-glass-like state by means of a bulk technique such as AC susceptibility or DC magnetometry, could be labeled either as a cooperative effect between the SPM superspins of the ferrite nanoparticles or a consequence of the magnetic frustration between the iron spins at the surface layer of each particle, originating from the uncompensated chemical bonds and lattice symmetry breaking. It seems plausible that in very small particles a disordered magnetic state covering the whole particle could be found at low temperatures while on larger particles the canted-spin region might only reach a certain depth from the surface. As pointed out in Ref. [49], the occurrence of a high field irreversibility, witnessed by an unsaturated hysteresis cycle, usually support the latter case, opening a scenario that sees the core and surface regions as very distinct from one another, the disordered region being limited to the surface layer only.

One would expect that upon the application of a high magnetic field ($>\sim 1kOe$) the anisotropy energy barrier would disappear; on the other hand, a disordered surface layer would create a complex multiminima energy landscape, actually broadening the EBD [61], while the joint effect of dipolar interactions shifts the average barrier toward lower values, introducing substantial low-energy contributions, as previously discussed.

The dependence of the anisotropy energy barrier at high applied fields, as seen by a dynamic experimental technique such as AC susceptibility, has been here investigated. The in-phase and out-of-phase AC susceptibility curves in sample **1**, the smallest of samples, at three external magnetic field intensities, $H = 0$, 3700 and 6800 Oe have been measured. Remarkably, an average barrier Δ could be extracted at all fields, by fitting the plot of the relaxation time τ as a function of temperature with an Arrhenius function $[\tau(T) = 2\pi/\nu(T) = \tau_0 exp(\Delta/T)]$. The values of τ were obtained from the maximum of χ'' using the relation $\omega\tau = 1$, ω being the working ac frequency. The parameters Δ and τ_0 extracted from ac data for sample **1** are $(\Delta, \tau_0) = (630.12$ K, 1.499×10^{-18} s/rad), (183.92 K, 8.445×10^{-13} s/rad), (66.29, 2.766×10^{-7} s/rad), respectively for $H = 0$ Oe, 3.7 kOe and 6.8 kOe.

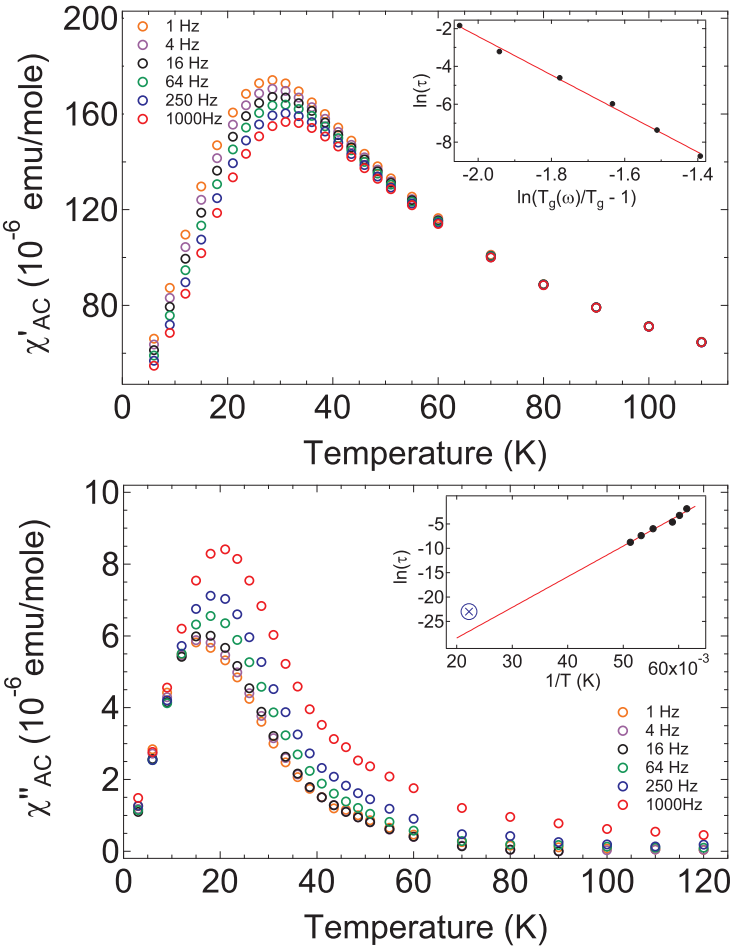

Figure 1.9 – AC Susceptibility measurements on sample **1** at various excitation frequencies. The upper figure reports the real part of the susceptibility, χ'_{AC} and an inset showing the result of the fit to the critical slowin-down law, Eq. 1.15. Data extracted from the imaginary part χ''_{AC} (bottom) was analysed with Eq. 1.5 and 1.6. The Néel plot is shown in the inset. Also in the inset, the blue circled cross marks the position of the data point from Mössbauer experiments on sample **1** (τ 10^-10 s/rad, $T_B = 45$ K; see Section 2.3.5 for further details).

Sample	d_{TEM}	$\bar{E}$ (DC)	τ_0 (AC-Arr)	E_{eff} (AC-Arr)	τ_0 (AC-V.F.)
	nm	K	s/rad	K	s/rad
1	3	318.54	4.95×10^{-19}	652.14	8.35×10^{-13}
2	4	199.75	4.74×10^{-16}	454.53	4.41×10^{-13}
3	7	728.63	1.40×10^{-11}	801.60	3.43×10^{-9}
4	12	1002.61	3.27×10^{-18}	4261.59	1.95×10^{-12}

Sample	d_{TEM}	E_{eff} (AC-V.F.)	T_0	τ_0 (Scaling law)	T_g (DC)	$z\nu$
	nm	K	K	s/rad	K	
1	3	242.33	6.88	1.22×10^{-10}	25.5	10.20
2	4	266.02	3.65	3.64×10^{-7}	17.6	7.43
3	7	442.06	13.31	-	-	-
4	12	1596.22	48.05	4.10×10^{-8}	193.7	2.24

Table 1.3 – This table gathers all the results from the analysis of AC susceptibility data with Eq. 1.5, 1.6 and 1.15. From left to right: average anisotropy energy barrier $\bar{E}$ from DC measurements; τ_0 attempt time and $\bar{E}$ effective barrier from the Arrhenius fit of AC imaginary susceptibility data; τ_0 attempt time and E_{eff} effective barrier and T_0 parameter from the Vogel-Fulcher fit of AC imaginary susceptibility data; τ_0 attempt time, T_g spin-glass critical temperature and critical exponent $z\nu$ from the fit of AC real susceptibility data to the phenomenological scaling law, Eq. 1.15.

Since τ_0 usually takes values in the range 10^{-9}–10^{-12} s for noninteracting superparamagnets in zero applied field, our results imply that Néel's model breaks down and that the activation energy is temperature dependent, a partly expected result on the basis of the imbalance of the two wells of the energy-level diagram when a magnetic field is applied. Unphysical τ_0 values are commonly encountered when magnetic nanoparticles are coupled by dipolar interactions (see Ref. [42] and references therein). The rather large values for Δ also reflect the presence of such couplings. The same test was repeated on χ'' curves of samples **2**, **3** and **4**. Average barriers and τ_0 are gathered in table 1.3. As it can be evinced by the tabulated values, Néel's model breaks down in samples **1**, **2** and **4**, whose AC data analysis resulted in quite unphysical values for τ_0. Sample **3**, though, seems to be fine, and this is also confirmed by the good agreement between the average barrier extracted from DC measurements ($\sim 728K$) and the value yielded by the Arrhenius fit on the AC data ($\sim 801K$). In all other cases, there is a significant difference between the values extracted by the two techniques. For sample **1**: $\sim 318K$(DC) vs $\sim 652K$(AC); sample **2**: $\sim 199K$(DC) vs $\sim 454K$(AC); sample **4**: $\sim 1002K$(DC) vs $\sim 4261K$(AC). An attempt to fit the AC data with the phenomenological Vogel-Fulcher model resulted in lower values for the average energy barriers and higher, more sensible values for τ_0. A quick comparison of the values in the two leftmost columns of Table 1.3 establishes the greater quality of the results from the V-F expression, being E_{eff} (AC-V.F.) comparable to $\bar{E}$ (DC), while the Arrhenius model shows little agreement with the DC data. It is here reminded that $\bar{E}$ (DC) has been

extracted from near-zero-field DC magnetometry data as the average of the best fit activation energy distribution, Eq. 1.13, satisfying equation 1.12.

The values of T_0 in samples **1** and **2** are very similar, while higher values characterize the other two bigger samples. This result suggests that the interparticle interactions could be comparable in the two samples; hence, bearing in mind that sample **2** is geometrically different from sample **1** but the particle diameters are almost the same, the interparticle distance would be around the same order of magnitude. The observation does not seem unrealistic since tight packing in powders would result in interparticle distances, meant as the minimum distance between the surfaces of two neighboring particles, of about 3 – 5 nanometers, which is roughly the nominal interparticle distance in sample **2**. Samples **3** and **4** feature similar interparticle spacings but the average magnetic moment is larger; then, a stronger dipolar coupling is expected, as demonstrated by markedly higher T_0 values.

To test the hypothesis of interparticle interactions leading to a spin-glass-like state in the three sample showing signs of such couplings, we followed a procedure applied to γ-Fe_2O_3 nanoparticles in Ref. [13] (see also Ref. [62]), fitting the χ' data at zero applied static field to the critical slowing-down law:

$$\tau = \tau_0 \left[T_g(\omega)/T_g - 1\right]^{-z\nu}, \tag{1.15}$$

where $z\nu$ is the product of the dynamical critical exponent z and the critical exponent ν associated with the correlation length. No temperature dependence of the attempt time τ_0 has been considered in the investigated temperature range. $T_g(\omega)$ has been extracted by $\chi'(T)$ as the temperature of the curve maximum at each working frequency ω (see Fig. 1.9 (a) and inset). T_g has been fixed to the temperature of the maximum in the ZFC curve at $H = 50$ Oe. For sample **1** I found $\tau_0 = 1.22 \pm 0.62 \times 10^{-10}$ and $z\nu = 10.2 \pm 0.3$; the value for the exponent $z\nu$ is in excellent agreement with values expected for the three-dimensional Ising-like spin glasses ($10 < z\nu < 12$)[63, 64] and with other results on maghemite nanoparticles (Parker *et al.*[13]: $z\nu = 10.3 \pm 0.3$, $d = 9$nm;). Analysis on sample **2** yielded $z\nu = 7.43$, which is still compatible with similar results found in literature (e.g. Leite *et al.*[57]: $z\nu = 8.0 \pm 0.2$, $d = 3$nm).

1.5 Conclusions

Non saturated hysteresis cycles have been found for all the investigated samples, an observation which has been related to a the effect of surface spin anisotropy on the static measurement of the magnetization.

Hints of the presence of a two-component magnetic configuration, ordered on the inside, disordered on the outside, have also been provided by the temperature dependence of the ZFC/FC magnetization. Indeed, the distribution of activation energies is broadened as a consequence of both a surface effect and an interparticle interaction effects. Consequently, energy barrier distributions have been observed even for relatively high magnetic fields ($H \sim 10$ kOe).

Suspects about strong interparticle interactions due to the tight packing of the powder-form samples have found confirmation after AC susceptibility measurements, that yielded results that can be interpreted under the hypothesis of a collective superspin-glass state. This hypothesis explains why the analysis with a standard Arrhenius-like function does not properly describe the temperature dependence of the Néel relaxation time of any of the investigated samples. The hypothesis is also consistent with the observation of the mixed behaviors, superparamagnetism on the one hand and spin-glass-like states on the other.

While particle interactions can be neglected when mid-to-high fields are applied, the distribution of energy barrier cannot, and it must be taken into account when investigating the materials by ^{1}H-NMR. In the next chapter the transition of the particles to a blocked/frozen state, even at high applied field, is discussed.

Chapter 2

Size-dependent spin dynamics in iron oxide nanoparticles by ^{1}H-NMR

2.1 Chapter overview

The main topic of this chapter is the investigation of the temperature-dependent and size-dependent spin dynamics of coated maghemite nanocrystals by the observation of anomalies in the ^{1}H-NMR nuclear-spin lattice relaxation rates. Specifically, the identification of the freezing process of the ensemble of superparamagnetic moments is achieved by searching for an enhancement of the relaxation rates, followed by the progressive broadening of the ^{1}H-NMR spectrum as the temperature decreases below the blocking temperature. However, superparamagnetic blocking is not the only dynamic process encountered within the covered temperature range ($1.5 < T < 300$ K); other relaxation mechanisms emerge at characteristic temperature values, such as the rotational motions of organic groups at high temperatures ($200 < T < 300$ K) and the slowing down of surface spin fluctuations at the lowest temperatures ($T <\sim 10$ K).

Information about the static and dynamic properties of the systems reported in this thesis, and presented in the previous chapter, represent useful cues for the interpretation of NMR proton relaxation rates. NMR spectra, NMR relaxation rates and Mössbauer data, also reported at the end of this chapter, all point to the conclusion that spin freezing occurs in all investigated samples, although at very different temperatures depending on the average size of the nanoparticles: very small particle can be considered as highly disordered superparamagnets with a small blocking temperature, while very large crystals (such as Sample **4**) may have a blocked magnetic moment even near room temperature; interestingly, the middle region (i.e. Sample **3**) is characterized by a relatively more structured relaxation rate profiles, an occurrence which is possibly related to the de-coupling of the 'inner-spin' dynamics and 'surface-spin' dynamics. As discussed in the previous chapter, the investigated samples also exhibit a collective magnetic behavior at low temperatures. However, the

strenght of the magnetic field employed in the NMR measurements quenches any emerging 'supra-particle' order, such as a superspin-glass, because of the intrinsic frailty of the collective state. For this reason, no additional reference to a collective state is present in this chapter.

2.2 Probing the dynamics

The exploration of the spin dynamics of ferrite nanoparticles has a long history, but the last 20 years have probably seen the most fervent scientific activity in this field, partly fueled by technological advances and the availability of powerful computational resources for the detailed modelization and simulation of complex systems.

On the experimental side, methodologies that exploit the static and dynamics measure of the magnetization of the particle ensemble are widely spread. Less common approaches rely on precise measurements of the local dynamics, which can be achieved only by refined resonance spectroscopy experiments. Among these techniques, Mössbauer is possibly the most used, thanks to the existence of fine tailored models and simulations that are able to match theory and experiments (see Ref. [65] for a comprehensive review and references). Other viable methods are the Electron Paramagnetic Resonance (EPR) spectroscopy and the Ferromagnetic Resonance spectroscopy, that provide additional information about the dynamics: starting with the seminal work of de Biasi of 1978 [66], the popularity of these techniques increased and were adopted to study magnetic anisotropy and size effects in magnetic nanoparticles [4, 67, 68, 69] and also more exotic concepts such as spin canting and surface effects [70, 42, 71] and quantum features [72, 73, 74]. Recently, it has also been reported that EPR studies could help to bridge the gap that divides the worlds of molecular magnets and magnetic nanoparticles [24].

Nuclear magnetic resonance (NMR) is frequently employed as a local probe for the study of the static and dynamic properties of bulk magnetic materials [75]. However, despite NMR investigations on bulk ferromagnets can be easily found in the literature [76], only a few NMR works on magnetic nanoparticles have been published. For instance, ^{59}Co NMR on single-domain cobalt nanoparticles was attempted on single-domain cobalt particles[77, 78], and on ferromagnetic nanowires [79] ($1/T_1$) and nanocomposites [80] (signal and spectra), while other groups focused on the ^{57}Fe NMR on fine powdered iron [81], nanocrystalline zinc ferrite [82] (spectra), and barium hexaferrite [83]. The first early studies that employ NMR on bulk iron oxide date back to 1959, when Gossard and Portis reported the first observation of nuclear resonance in a ferromagnetic bulk cobalt sample[84]. ^{57}Fe-NMR firstly appears in 1963 in a work about bulk magnetite [85, 86, 87, 88] (signal and spectra), then later on α-Fe_2O_3 (hematite) [89, 90, 91] and other ferrimagnetic oxides [92, 93]. Maghemite (γ-Fe_2O_3) first appears as the object of a 2006 paper, Ref. [94], on bulk micron-sized powder, while only just recently two ^{57}Fe NMR line shape studies have been reported

for maghemite powders in the 18-85 nm range [95, 96]. Even the very recent literature seems to confirms that ^{57}Fe-NMR is the obvious choice to observe the local spin dynamics of such nanostructured iron oxides (e.g. Ref. [97] and [98]).

However, despite choosing ^{57}Fe nuclei as NMR probes would seem convenient, this approach carries serious drawbacks; first of all, ^{57}Fe has a gyromagnetic ratio $\gamma_{^{57}Fe}/2\pi = 1.378$ MHz/Tesla; as a consequence, the relative NMR sensitivity of ^{57}Fe is found to be 3.37×10^{-5}. We attacked the problem of a local investigation of the spin dynamics from a different and novel perspective: the external organic coating of the oxide nanoparticle core contains a great number of uniformly distributed hydrogen atoms, whose ^{1}H nuclei are an obvious and excellent spin-1/2 NMR probe. ^{1}H NMR relative sensitivity is 1 by definition, i.e. about 3000 times higher than ^{57}Fe. Additionally, ^{1}H gyromagnetic ratio is 42.576 MHz/Tesla, allowing for an NMR investigation at low magnetic fields. The main disadvantage of this approach resides in its intrinsically quasi-local character, since a considerable amount of protons are located in regions distant from the iron-oxide core; distant protons would sense an average hyperfine magnetic field related to the nearby particles' superspins. On the other hand, protons close to the surface of the inorganic core are also very sensitive to the closest particle's surface magnetic ions. This last observation opens an exploitable window to the investigation of surface and interface phenomena in these nanostructured systems.

By virtue of the complexity of such systems, a rich phenomenology should be observed as the temperature decreases and internal motions and/or hyperfine magnetic field fluctuations slow down, revealing themselves through a significant enhancement of the proton spin lattice relaxation rates, i.e. $1/T_1$. Thanks to the different correlation times associated with the various encountered fluctuations, it is usually possible to clearly distinguish between each contribution to the relaxation rate. For instance, rotational motions of a number of organic groups, e.g. Methylene (CH_2) or Methyl (CH_3) groups, are characterized by a rotational correlation time of about $\tau_r = 10^{-7} - 10^{-9}$ s/rad at room temperature; these motions should be observed by NMR in the form of a broad peak in $1/T_1$, near or just below room temperature, when the rotational correlation time satisfies the condition $2\pi/\tau_r \sim \nu_L/$, ν_L being the Larmor precession frequency for protons.

Since Néel's correlation time τ_N for superparamagnetic fluctuations of the magnetic moment of ferrite nanoparticles should fall within the range $10^{-12} < \tau_N < 10^{-9}$ s/rad, depending on the species of the magnetic ion and size/shape of the particle, proton relaxation rates should be enhanced at relatively lower temperatures than those associated with the freezing of Methyl and Methylene groups. On the other hand, it is not uncommon to find correlation times of the order of 10^-8 for either very anisotropic or very large particles; thus, it is reasonable to expect, in these extreme cases, that the enhancement of $1/T_1$ will coincide with that related to rotational motions of organic groups. The anomaly in $1/T_1(T)$ could also be positioned above room temperature, i.e. outside the investigated temperature range.

The blocking temperature of small magnetic particles, having diameter $d < 5$

nm, assumes values in the range $10 < T_B < 60$ K, while slightly larger particles ($5 < d < 10$ nm) have $T_B \sim 100 - 150$ K, so the $1/T_1$ anomaly should be observed in this temperature ranges. Additionally, in some cases a magnetic particle could exhibit two different magnetic orders: a collinear order in an inner core shell and a disordered order in an outer surface shell, due to the decreased coordination number of surface Fe atoms. Consequently, two different correlation times describe the spin freezing dynamics: one, $\tau_{N,core}$, is related to the superparamagnetic blocking of the aligned core spins; the other τ_{surf} describes the freezing of the disordered surface spins to a spin-glass-like state and it is usually shorter than $\tau_{N,core}$ [99]. The results is a double peak in $1/T_1$, one at intermediate temperatures $50 < T < 150$ K (core contribution) and one at low temperatures $T < 50$ K (surface contribution).

Finally, the spin configuration of very small magnetic particles ($d < 5nm$) can be completely disordered, i.e. the disorder induced by surface atoms with non-saturated bonds can extend to the whole particle because the thickness of the magnetically frustrated surface shell would be comparable to the particle diameter. In this scenario only one peak is found at low temperatures, because surface spins and core spins are so strongly correlated that only one correlation time is sufficient to describe the dynamics of Fe spins.

2.3 ^{1}H-NMR and Mössbauer spectroscopy experiments on coated magnetic nanoparticles.

Relaxometric properties of Iron-oxide nanoparticles have been investigated at two main NMR frequencies, 21 MHz and 58 MHz, respectively corresponding to applied static field $H_{ext} = 5$ and 14 kOe. Hereby the temperature dependence of NMR spectra, line-width (FWHM) and spin-lattice relaxation time for all samples will be presented.

A field-sweeping setup on a 15 kOe electromagnet, related procedures and automation programs have been developed by the author of this thesis specifically for the purpose of sampling large NMR lines on solid state samples, both in Pavia and Ames, IA, USA. Spectra measurements have been carried out by sweeping the external field around the resonance condition at a slow sweeping rate, while pinning the RF frequency to a specific value. Each point in a spectrum corresponds to a NMR solid-echo experiment, characterized by very short RF pulses, with a pulse width in the range $1 < \tau_{\pi/2} < 4$ μs. The sampled spectrum is then actually the envelope of many different spectra, each centered at the Larmor frequency of the resonant nuclei, a slice in the frequency domain selected by moving the field. In principle the envelope could be calculated by numerical computation of the convolution of the various Fourier transforms of all echo signals measured during the sweep sequence. In practice it is far more convenient to simply plot the area of the echo signal as a function of the instant

external static magnetic field, measured with a Hall probe. This method was chosen to overcome the limitation of the calculation of spectra as numerical FT of the echo signal, because the proton NMR line is very broad and it is not possible to guarantee the same optimal RF irradiation condition for the whole frequency range spanned by the ^{1}H-NMR spectrum; only a small portion of the spectrum can be adequately irradiated and it is roughly $\delta\nu = 1/2\tau_{pi/2}$ wide, i.e. about 100 – 250 kHz, a value comparable to the proton NMR line-widths at half maximum in the studied materials.

T_1^{-1} values have been estimated by monitoring the return to equilibrium of the longitudinal nuclear magnetization of hydrogen nuclei after applying a standard saturation recovery sequence. Additional details on the measure of T_1^{-1} are given in section 2.3.2.

2.3.1 ^{1}H-NMR Spectra

A selection of ^{1}H-NMR line-shapes at various temperatures is reported for Sample **2** in Fig. 2.1, as an exemplary case. Indeed, every observed NMR spectra on all coated ferrite nanoparticle samples feature a Lorentzian symmetric line shape and a distinct line broadening as the temperature is lowered, related to the progressive freezing of the particle superspins. The full width at half maximum (FWHM) was calculated and plotted in Fig. 2.2 against the measuring temperature. We can safely ascribe the temperature dependence of the NMR FWHM to an inhomogeneous component originating from a distribution of hy-

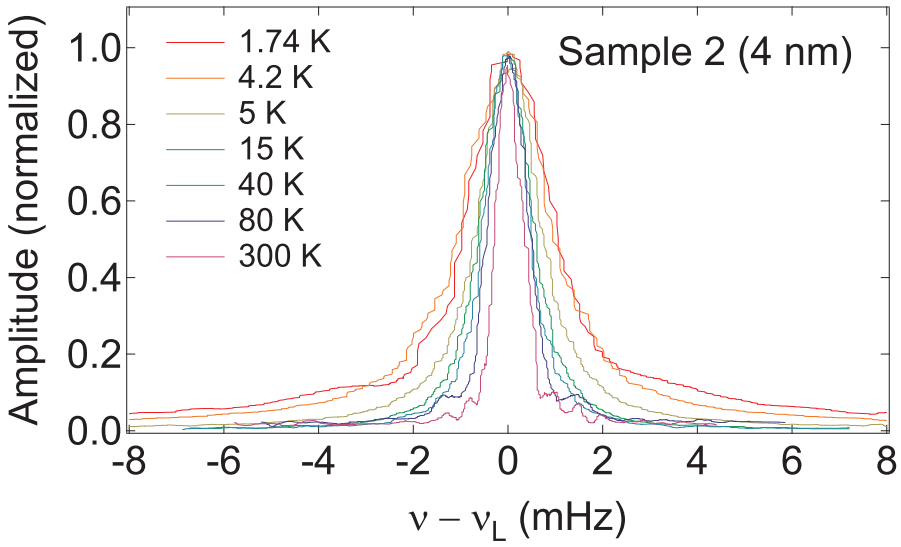

Figure 2.1 – Proton NMR spectra of Sample **2**, recorded by field-sweeping at fixed frequency $\nu_L = 58MHz$. A selection of 8 spectra sampled at different temperatures, covering the range $1.74 < T < 300$, is reported to show the progressive broadening of the NMR line as the temperature is lowered. The side peaks at temperatures 80 K and 300 K are only apparent: they are actually experimental glitches due to the interference of noise a signal phase correction algorithm during acquisition.

perfine dipolar fields at the nuclear proton sites. Such a distribution is due to the interaction of the magnetic moments of protons with the Fe^{2+} and Fe^{3+} magnetic moments.

The very large broadening of the line at low temperatures is proof of the slowing down of the spin dynamics upon cooling, and of the strong hyperfine coupling with the nuclei. It should be noticed that the protons closer to the surface of a magnetic nanoparticle experience a distribution of dipolar fields due to the disordered magnetic configuration of the electronic spins in the nearby surface layer; then, the probes closer to the surface should mainly sense the surface layer dynamics, surely through magnetic dipolar interaction and, possibly, through direct and/or transferred exchange interaction in those cases where an appreciable overlapping exists between the electronic orbitals of the coating molecule and those of the Fe ions.

Additionally, each spectrum is intrinsically broadened because of the great number of inequivalent proton sites in the coating material and also considering the orientational disorder of powders, resulting in a wide distribution of nuclear Larmor frequencies. A temperature independent component due to nuclear dipole-dipole magnetic interaction is also present.

Figure 2.2 collects all the FWHM vs T plot of the four investigated samples at various external magnetic fields.

In Sample **1** the ^{1}H-NMR LW progressively increases with decreasing temperature, passing from 200 – 600 KHz at ~70 K to ~1.5 MHz at ~1.5 K, following the progressive freezing of local spins. Under $T = 4$ K the line-width saturates, marking the achievement of a completely blocked state of the SPM moments. The data set for $H = 14.4$ kOe is offset by roughly +300kHz with respect to the set for $H = 3.7$ kOe, simply because the sample magnetization is higher and creates a broader distribution of local hyperfine fields.

Although the same trend is replicated on the plot relative to Sample **2**, showing the line broadening at three different magnetic fields ($H = 2.7, 5, 14$ kOe), saturation of the line is not yet achieved at the lowest temperature, 1.5K. Moreover, the excursion between the FWHM values at room temperature and 1.5K is less pronounced with respect to Sample **1**.

As the particle size is increased, we witness a decreasing maximum relative broadening of the ^{1}H-NMR line, with respect to the line width at room temperature: Sample **1** $\sim 400\%$, Sample **2** $\sim 270\%$, Sample **3** $\sim 200\%$ and Sample **4** $\sim 130\%$. For samples **3** and **4**, the observed behavior can be ascribed to the saturation of the NMR line at much higher temperatures with respect to the two smaller samples. This is consistent with the measured blocking temperature extracted from the NMR spin lattice relaxation rates versus temperature profiles, as is further on discussed briefly: $T_{B,NMR}$ sits around 150K for Sample **3** and around, or possibly over, $280K$ for Sample **4**; consequently the spectrum width shows little signs of broadening, given that the local hyperfine magnetic fields created by the blocked particles are frozen under $T_{B,NMR}$.

The smaller samples, on the other hand, linger in the motional narrowed regime down to very low temperatures because their magnetic moments are

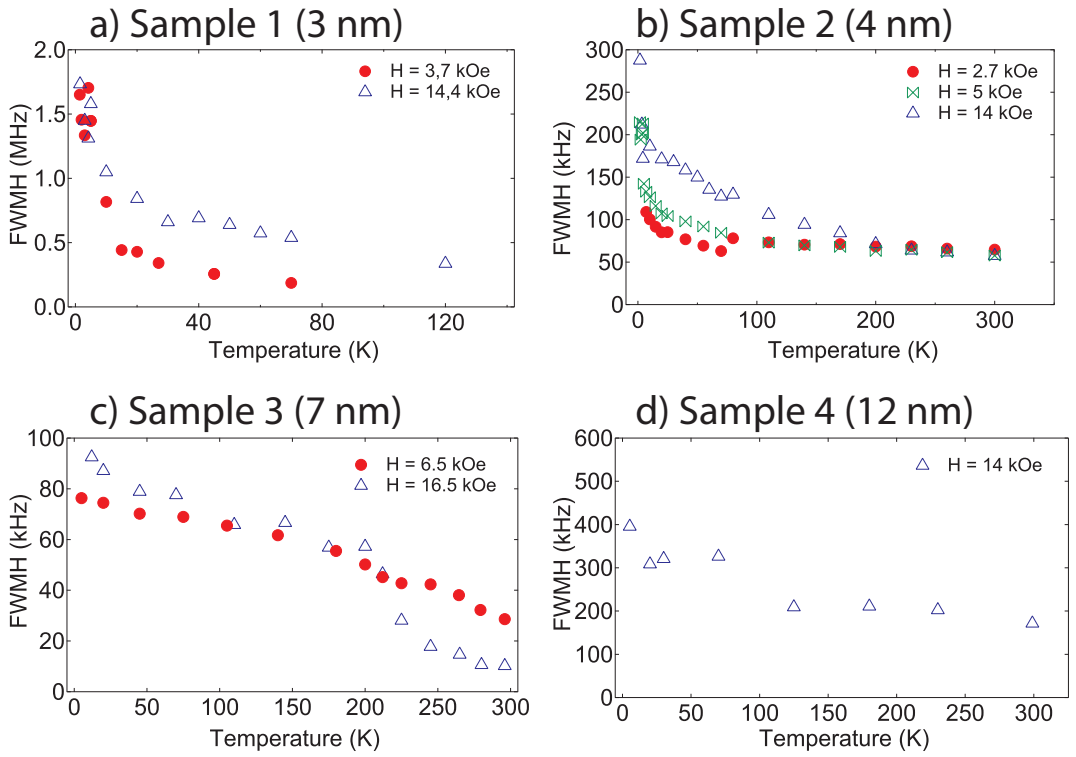

Figure 2.2 – These four panels report the temperature dependence of the Proton-NMR line widths (FWHM) for all four presented samples. Different external magnetic fields were used in each case: H = 3.7 and 14.4 kOe for Sample **1**, H = 2.7, 5 and 14 kOe for Sample **2**, H = 6.5 and 16.5 kOe for Sample **3** and H = 14 kOe for Sample **4**. The overall observed trend is a pronounced broadening of the proton spectrum when decreasing the temperature, a phenomenon related to the freezing of the superparmagnetic moments of the particles. Saturation of the line width is reached at the lowest temperatures for samples **1** and **2** while the line is already saturated at high (room) temperature for samples **3** and **4**.

fluctuating freely under thermal excitation, and the transition to the blocked regime is definitely more abrupt with respect to the 7 nm and 12 nm samples.

One interesting feature that characterizes the trend of the NMR line width with the particle size is that the absolute value of the FWHM is maximum on Sample **1**, i.e. 1.7 Mhz at $T = 4.2$ K, and it drops down to 300 kHz on Sample **2** and to 100 kHz on Sample **3**; then the FWHM rises up again to 400 kHz for the largest sample, $d = 12$ nm. The very high values of FWHM in Sample **1** are most certainly due to the canted nature of the internal spin configuration of the magnetic core: Mössbauer spectroscopy experiments confirms that for this sample the disordered magnetic state that is frequently observed on the surface [100] of the particle is in this case extended to the whole particle volume (see section 2.3.5). Consequently, the distribution of local hyperfine fields at the proton sites near the particle is much wider than in any other investigated samples. A possible explanation for the behavior of FWHM with the particle size is that as the particle diameter increases the fields experienced by the protons is altogether more homogeneous since the collinear order of iron spins inside

the particles is favored by the greater anisotropy; however, on large particles (e.g. $d = 12$ nm) the average magnetic moment $\langle\mu\rangle$ of each particle increases considerably; as a result, the distribution of hyperfine fields broadens.

For the two small samples, i.e. Samples **1** and **2**, the line-width at temperatures in the range $T >\sim 30$K has two main contributions: first, a field independent term related to nuclear dipole-dipole interaction among protons in the coating molecules; another term comes from the proton-superspin dipolar interaction: the particle superspin, polarized by the external field, generates at the proton site a local hyperfine field which is proportional to the local superparamagnetic moment, i.e. $\chi_{loc}H$. As a result, the NMR line-width is given by

$$\delta\nu = \delta\nu_{dip} + A\chi_{loc}H \tag{2.1}$$

where the prefactor A is an average hyperfine coupling constant between the nuclei and the superparamagnetic moments. Such paramagnetic broadening is inhomogeneous due to the distribution of local hyperfine fields at inequivalent proton sites, with different dipolar fields resulting from the anisotropic character of the dipolar interaction. As a matter of fact, the paramagnetic broadening divided by the external field yields an estimation of the local magnetic susceptibility. This explains why the qualitative temperature behavior of the line-width is not exactly the same as the bulk $\chi_{FC}(T)$ measured by DC magnetometry: the increase in the FWHM on lowering the temperature reflects the increase of the local magnetization of the system. Below 30 K, thermal fluctuations of the particle magnetic moment severely slow down, then the FWHM increases dramatically.

The field dependence of the FWHM vs H shown in Fig. 2.3 follows from eq. 2.1 and the extrapolated value at $H = 0$ yields the dipolar contribution to the line-width, which accounts only for about 65 kHz of the line broadening of both Sample **1** and Sample **2**.

2.3.2 Longitudinal spin-lattice nuclear relaxation rates.

We turn now to the presentation of the Nuclear Spin Lattice Relaxation Rates (NSLRs), measurements by ^{1}H-NMR recovery sequences. A collection of recovery curves for Sample **2** is reported in Fig. 2.4, as an example of a typical measurement set. The recovery of the longitudinal nuclear magnetization toward the equilibrium is described by a wide distribution of relaxation times that results in a strongly non-exponential profile for the recovery curve. This behavior characterizes all four samples, indicating that the NMR probes are indeed experiencing a highly inhomogeneous spatial distribution of local hyperfine magnetic fields: protons near the particle surface are more likely to probe both the magnetic dynamics of both surface and core and are thus responsible for the fast contributions to the nuclear magnetization relaxation.

On the other hand, protons distant from the magnetic centers are less susceptible to relax since the strength of the magnetic interactions is lower and

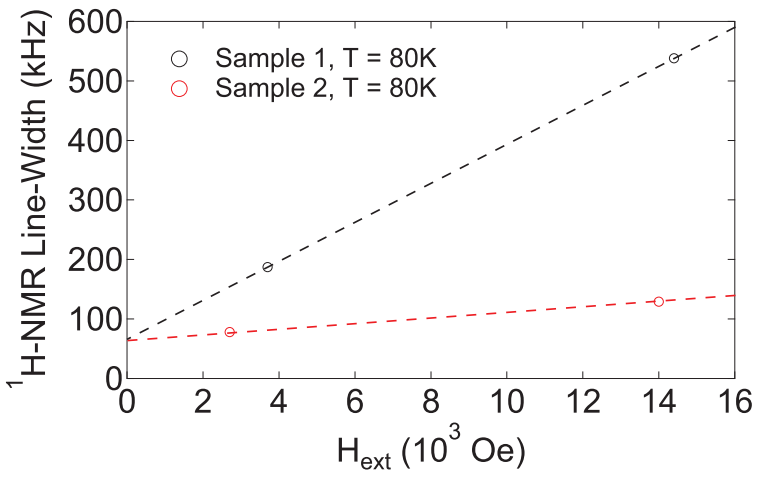

Figure 2.3 – Field dependence of the Proton-NMR line width (FWHM) measured at $T = 80$ K in Sample **1** (3 nm) and Sample **2** (4 nm) at two different frequencies, $\nu_L \sim 16$ MHz (corresponding to ~ 2.8 kOe) and $\nu_L = 60$ MHz (corresponding to ~ 14 kOe). The dashed lines are fit to Eq. 2.1: the extrapolated values of the line width at $H = 0$ yields a rough estimation of the dipolar contribution to the broadening; for both samples this contribution amounts to ~ 65 kHz.

they mainly contribute to the slow components of the relaxation. Beside the effect due to the presence of inequivalent proton sites, one should also take into account the orientational distribution of the nanoparticles in the powders as an additional source for the distribution of relaxation times.

No analytical expression was chosen *a-priori* to fit the recovery curves and estimate the T_1 values, since we lack a theoretical understanding of the distribution of longitudinal nuclear-spin relaxation times in such a disordered system; instead, a 5-degree polynomial interpolation was calculated. The polynomial $P_M(t)$ is the best-fit of the recovery curve in a time range t centered roughly around the instant t^* corresponding to $(1-M(t^*)/M_{inf} = 0.6)$, i.e. the 60% level in Fig. 2.4. The actual time value representing the estimate of T_1 was then read on the interpolated curve, $P_M(t)$ at a position corresponding to $P_M(t) = 0.6$. This procedure allowed to measure an effective relaxation parameter T_1, consistent throughout all measurement sets. As such, the estimated T_1 values have to be considered as average values associated to the fastest relaxing nuclei.

The NSLR as a function of temperature for Samples **1** – **4** are presented, respectively, in figures Fig. 2.5 through 2.8.

Sample **1** features a very clear peak in $T_1^{-1}(T)$ at $T = 42$ K for both $H = 3.7$ kOe and $H = 14.4$ kOe; below these temperatures this sample is considered to be in the blocked regime on the time scale of the NMR measurement. A lower shoulder near $T = 7$ may be distinguished on the curve for $H = 3$ – 5 kOe, although its nature is unclear. Unfortunately the experimental data set only covers temperatures in the range $1.5 < T < 150$ K because at $T > 150$ K the NMR signal becomes comparable to the thermal noise and disappears.

From the AC susceptibility and DC magnetometry data presented in the previous chapter, an anomaly in $1/T_1$ was expected at low temperatures, although

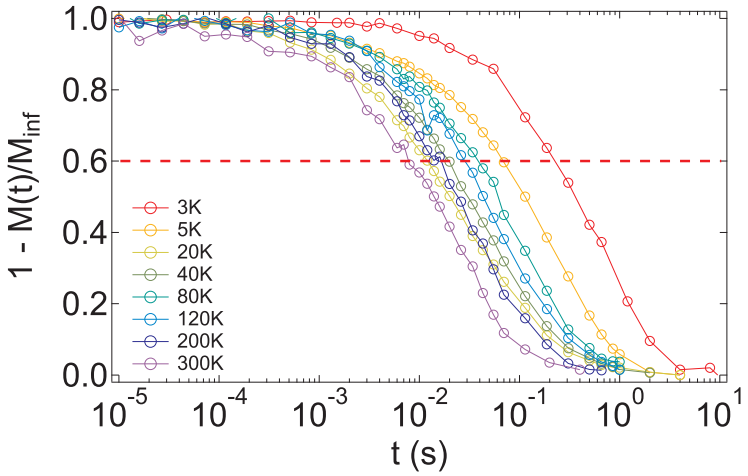

Figure 2.4 – Strongly non-exponential nuclear magnetization recovery curves measured on Sample **2** (4 nm) at $H = 2.7$ kOe, selected as representative of the observed behavior in all samples. Analysis of these curves rely on 'manual' estimation of T_1, i.e. the T_1 value is the time position at which the recovery reaches the value of 0.6. The red dashed line in the graph marks such reading level.

the position of the peak is found at temperatures higher than T_B (DC).

An analogous low-T peak was found for Sample **2** at even lower temperatures, i.e. $T = 24$ K, at $H = 2.7, 5, 14.4$ kOe. To this date the reason behind the difference between Sample **1** and **2** is unclear, even though some speculation is possible: leaving aside any effects due to a possibly different strength of dipolar interparticle interactions, the causes of such a deviation might reside in the internal magnetic configuration of the spin systems (canted spins, collinear order, vortex order, and so on...), that in turn depends on the shape of the nanocrystals [100]; a substantial difference in the shape of the distribution of sizes and/or anisotropy energy barriers may also play a major role.

The strong NMR signal of Sample **2** allowed for the covering of the whole 1.5 – 300 K temperature range. At $T \sim 260$ a second peak was found in the NSLR of Sample **2** and was easily identified as the effect of the slowing down of rotational fluctuations of CH_2 and CH_3 organic moieties present both in PVP and PEG chains.

On Sample **3** the anomaly associated with the superparamagnetic freezing was found at $T = 127$ K for $H = 6.5$ kOe and at $T = 138$ K for $H = 16.5$ kOe. A low-T peak at $T = 11$ K for $H = 6.5$ kOe and at $T = 30$ K at $H = 16.5$ kOe was also observed but it was not further investigated. The current preliminary interpretation, though, relate the low-T peak to the freezing of surface spins. Another peak in $T_1^{-1}(T)$ was found near room temperature and interpreted as the contribution from CH_2 / CH_3 organic groups of the coating molecules.

Finally, Sample **4** features only one broad peak in $T_1^{-1}(T)$ at $T \sim 250$ K for both $H = 3.7$ kOe and $H = 14.4$ kOe. Unfortunately it is highly probable that the peak from the spin freezing is superimposed over the one associated to the rotation of organic groups, as previously discussed. The position of the peak associated to the superparamagnetic freezing of magnetic ferrite nanoparticles

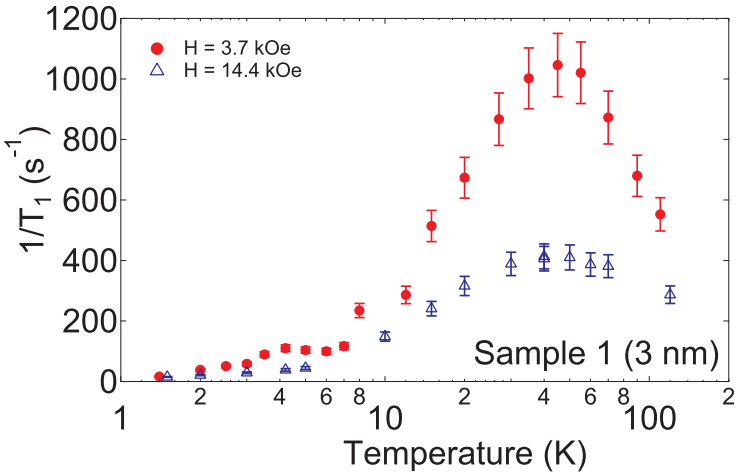

Figure 2.5 – $1/T_1$ vs T data for Sample **1** (3 nm)

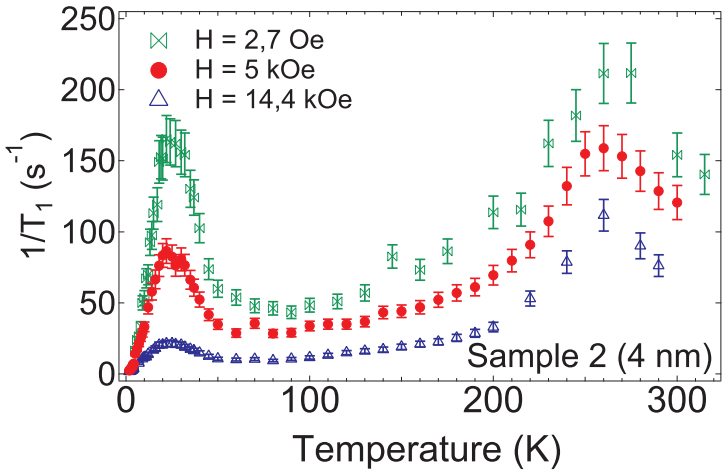

Figure 2.6 – $1/T_1$ vs T data for Sample **2** (4 nm)

was found to be almost independent of the external applied field, at least within the experimental error, although the absolute value of the local maximum scales with the field roughly as $1/H$.

2.3.3 Theory of proton spin-lattice relaxation rates for coated superparamagnetic nanoparticles

NMR relaxation theory postulates that, in general, in order to cause relaxation, there must be a time-dependent modulation of spin interactions which act directly on the nuclear spins[101]. Consequently, an essential requirement for relaxation is that the molecular motion or, alternatively, local field fluctuations must occur on a suitable time scale, that is, interactions which cause fluctuations at or near the nuclear Larmor frequency will be the most effective. For instance, in a superparamagnetic system at the superparamagnetic limit, the collective slowing down of the superspin fluctuations when passing to the

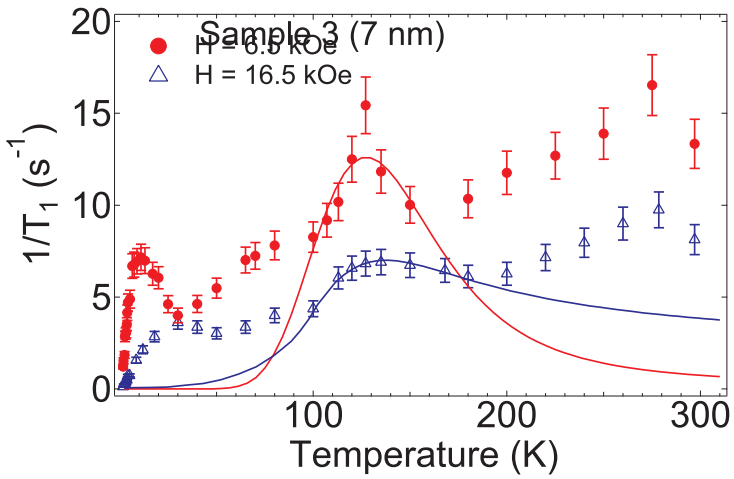

Figure 2.7 – $1/T_1$ vs T data for Sample **3** (7 nm)

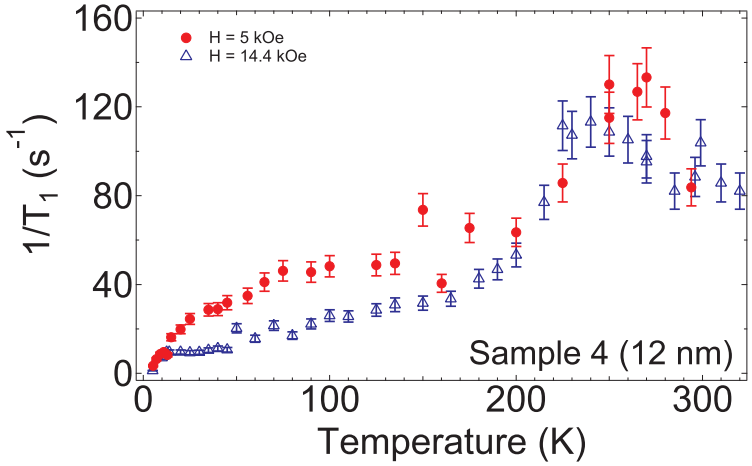

Figure 2.8 – $1/T_1$ vs T data for Sample **4** (12 nm)

blocked regime is sensed by the NMR probe as a slowing down of the fluctuating dipolar particle-nuclear interaction.

The spin-interaction Hamiltonian relevant for magnetic resonance can be expressed in a general form as

$$\mathcal{H}(t) = \sum_i f_i \sum_k F^{(k)}(t) O^{(k)} \tag{2.2}$$

where index i runs over all possible couplings; factors f_i are interaction-specific constants, $O^{(k)}$ are spin operators, and $F^{(k)}(t)$ are the fluctuating structure functions, which will in general be a function $F^{(k)}(t, \mathbf{r})$ of both time t and relative positions $\mathbf{r}$ of neighboring atoms in the lattice (or molecule). In this brief introduction we neglected the spatial dependence of the structure factors and, as a consequence, in the following sections we also dropped the spatial dependence of the autocorrelation function and the momentum dependence of the spectral density function, i.e. $G(t, \mathbf{r}) \approx G(t)$ and $I(\omega, \mathbf{q}) \approx I(\omega)$, respectively. The main reason behind this approximation is the fact that there are

many non-equivalent magnetic ions sites and proton sites on the single particle; moreover, the investigated samples consist of disordered ensembles of magnetic particles, thus the spatial effect is effectively averaged to a negligible amount. Several types of couplings may lead to relaxation; among them, the dipolar coupling in particular provides a very efficient relaxation mechanism. Such coupling is composed of two components in the case of coated ferrite nanoparticles: a first contribution comes from nuclear-nuclear dipolar coupling between spin-1/2 hydrogen nuclei; each ^{1}H is also magnetically coupled to the particle electron superspin and experiences the magnetic field fluctuations due to the superparamagnetic relaxation. Protons close to the surface of the particles may also experience a scalar interaction due to the proximity of Fe^{2+} and Fe^{3+} ions outer orbitals. Consequently, the total T_1 relaxation time consists of several contributions associated to many different types of couplings that usually cannot be measured individually:

$$\frac{1}{T_1} = \frac{1}{T_{1,n-n}} + \frac{1}{T_{1,n-e}} + \frac{1}{T_{1,scalar}} + \dots \tag{2.3}$$

The phenomenon of the fluctuation of spin interactions is described by the autocorrelation function $G_{(k)}(\tau)$ of the structure function $F^{(k)}(t)$. $G_{(k)}(\tau)$ is a measure of the correlation between values of the function $F^{(k)}(t)$ with itself at a time difference τ:

$$G_{(k)}(\tau) = \left\langle F^{(k)}(t) F^{(-k)}(t+\tau) \right\rangle \tag{2.4}$$

As such, $G_{(k)}(\tau)$ measures the persistence of the fluctuations. The Fourier transform of the autocorrelation function is known as the spectral density function $J_{(k)}(\omega)$ and it represents the fluctuations probability in the structure function to have a certain frequency ω.

$$J_{(k)}(\omega) = \int_{-\infty}^{\infty} G_{(k)}(\tau) e^{-i\omega\tau} d\tau \tag{2.5}$$

The initial values of the autocorrelation functions are equal to the mean squared fluctuation of the structure function, i.e. $G_{(k)}(0) = \left\langle |F^{(k)}|^2 \right\rangle$. Irrespective of the interaction and observable types, one can show that the relaxation rates can be expressed in terms of the reduced autocorrelation function $\tilde{G}_{(k)}(\tau)$:

$$\tilde{G}_{(k)}(\tau) = \frac{\left\langle F^{(k)}(t) F^{(-k)}(t+\tau) \right\rangle}{\left\langle |F^{(k)}|^2 \right\rangle} \tag{2.6}$$

The Fourier transform of the reduced autocorrelation function $\tilde{G}(\tau)$ is the reduced spectral density function $I(\omega)$, and is supposed to be the same for all $F^{(k)}$:

$$I(\omega) = \int_{-\infty}^{\infty} \tilde{G}(\tau) e^{-i\omega\tau} d\tau = 2 \int_{0}^{\infty} \tilde{G}(\tau) \cos \omega\tau d\tau \tag{2.7}$$

Frequently, the motional averaging can be expressed in terms of an exponential decay reduced autocorrelation function with a time constant τ_c, called the correlation time.

$$\tilde{G}(\tau) = e^{-\tau/\tau_c} \tag{2.8}$$

The reduced spectral density function then becomes

$$I(\omega) = \frac{2\tau_c}{1+\omega^2\tau_c^2} \tag{2.9}$$

The spectral density $I(\omega)$ is thus a Lorentzian of width $1/\tau_c$ and centered at $\omega = 0$, whose shape depends on the lattice excitation, while its area remains constant. Spectral density functions such as Eq. 2.9 are fundamental to the theoretical description of relaxation. They allow the dynamic characteristics of the system, defined by τ_c, to be expressed in terms of the spectral density function at frequency ω.

In order to build a simple phenomenological model to grasp the essential features of the nanoparticle spin system, we started from Moriya's expression of the spectral density function for nuclear spin-lattice relaxation rates in paramagnetic materials[102, 103]:

$$\frac{1}{T_1}(T) = A(T)\chi(T)TI(\omega) = A(T)\chi(T)T\frac{\tau_c(T)}{(1+\omega^2\tau_c(T)^2)} \tag{2.10}$$

The prefactor $A\chi(T)T$ contains the temperature dependence of the static magnetic susceptibility $\chi(T)$ and is proportional to the mean square value of the local hyperfine field fluctuations $\langle\Delta h^2\rangle$, since $A\chi(T)T \equiv \gamma^2 \langle\Delta h^2\rangle /2$. The quantity $I(\omega_0)$ reaches its maximum value when the characteristic frequency of fluctuations matches the Larmor frequency. When this condition is met ($\omega_0\tau_c = 1$) the relaxation rate becomes:

$$\left(\frac{1}{T_1}\right)_{max} = \frac{\gamma^2}{2}\left\langle\Delta h^2\right\rangle\frac{1}{\omega_0} \tag{2.11}$$

and an estimate of the hyperfine field at the nuclei can be deduced from the measurement of $(1/T_1)_{max}$.

We assumed that the characteristic correlation time of the spin system could be described by the superparamagnetic relaxation time τ_N that, in the case of non interacting nanoparticles, takes the form of the simple Néel expression:

$$\tau_c(T,\Delta) \equiv \tau_N(T,\Delta) = \tau_{0,\mathrm{NMR}}e^{-\frac{\Delta}{k_BT}} \tag{2.12}$$

In Eq. 2.12, $\tau_{0,\mathrm{NMR}}$ is the attempt time experience at the magnetic fields of the NMR experiments. As discussed in section 1.3, the temperature behavior of a superparamagnetic nanoparticle ensemble is directly related to its mean effective magnetic anisotropy energy. Actually, we need to take into account that a whole distribution of energy barriers Δ takes part in the dynamics. In chapter 1 it was demonstrated that, despite the application of a large magnetic

field, the EDB is not completely quenched. For this reason we assumed that the EDB could be approximated, at any field condition, by a lognormal distribution $P(\Delta)$ of barrier parameter Δ, with median value $\bar{\Delta}$ and scale parameter σ_Δ:

$$P(\Delta) = \frac{1}{\Delta\sigma_\Delta\sqrt{2\pi}} \exp\left(-\frac{\left[\ln\Delta - \ln(\bar{\Delta})\right]^2}{2\sigma_\Delta^2}\right) \tag{2.13}$$

With the insertion of Eq. 2.12 into Eq. 2.11, weighting with the distribution $P(\Delta)$, and integrating over Δ, Eq. 2.11 becomes:

$$\frac{1}{T_1}(T) = A\chi(T)T\int_0^\infty P(\Delta)\frac{\tau_c(T,\Delta)}{1+\omega_L^2\tau_c^2(T,\Delta)}d\Delta \tag{2.14}$$

which is the final expression employed to fit all the NMR spin-lattice relaxation rate versus temperature curves. A slightly more consistent version of Eq. 2.14 can be obtained by substituting the Arrhenius-like Néel expression for the correlation time with the phenomenological Vogel-Fulcher equation, already applied to the analysis of AC and DC magnetic data. Of course, this operation implies the addition of a correction of the $T_1^{-1}(T)$ function when $T- > T_0$, to handle the unphysical divergence in the temperature dependence of T_1^{-1}, induced by the $T - T_0$ term in the V-F expression. On the other hand, results from the improved equation were almost indistinguishable from those obtained with equation 2.14, within experimental error, and will thus not be discussed in the next section.

2.3.4 $1/T_1$ data analysis

The analysis of the peaks due to the finite size phenomenon has been attempted, identifying the correlation time τ_c that enters in the theoretical expression of T_1, Eq. 2.14, with Néel's relaxation time τ_N (Eq. 2.12), which is usually valid for non-interacting magnetic particles. However, it is noted that this assumption implies that the local spin-spin correlation function decays in time in the same way as the macroscopic magnetization correlation function, which is a risky approximation.

As seen in Chapter 1, the bulk magnetization relaxation time dependence on the temperature is not generally described by a simple Arrhenius law, thus a more complex model should be developed to take into account other contributions to the relaxation of the particle's electronic magnetization. On the other hand, the choice of 2.12 greatly simplifies the numerical calculation of Eq. 2.14, at the same time preserving a grasp on the fundamental dynamics that we are interested in, which is the SPM blocking. On this respect, an additional argument in favor of the validity of this strong approximation to the samples investigated in this thesis is presented at the end of this section

We must address one more approximation that affects Eq. 2.14: a Lognormal shaped EBD, $P(\Delta)$, was once again chosen to better mimic the real distribution functional form. Indeed, the real distribution $P_{real}(\Delta)$ at the applied

field is never known exactly; as a matter of fact, the *a-posteriori* calculation of $P_{real}(\Delta)$ through fit to experimental data is by definition an ill-posed problem because the analytical form for $P_{real}(\Delta)$ that results in the observed data points is not unique. A number of numerical approaches could be employed to solve the inverse problem, such as the Expectation Maximization algorithm, Monte Carlo simulations, Genetic Algorithm Inversion and many others. The implementation of these methods is beyond the frame of this thesis but might be object of future research.

On a side note, we included the temperature dependence of the prefactor χT in Eq. 2.14 by fitting the experimental $\chi_{FC}T$ curve with a 5 order polynomial expression, then feeding the polynomial coefficient to the fitting routine. By doing so, we assumed that the local magnetic susceptibility χ_{loc} could be approximated by the measured bulk magnetic susceptibility χ_{FC}.

The best fitting parameters for $T_1^{-1}(T)$ curves for all samples are listed in Table 2.1. Figure 2.9 shows all graphs of NSLR vs T, where the best fit curves have been plotted over the experimental data points. The plot ranges were adjusted to highlight the anomaly of interest in $T_1^{-1}(T)$.

The very simple model embodied by Eq. 2.14 is sufficient to excellently reproduce the experimental data, with extracted EBDs that qualitatively follow the expected behavior, in good agreement with the results from DC magnetometry (see section 1.3). All distributions are gathered in Fig. 2.10: the common trend is a decrease of both the temperature of the distribution maximum $T_{P_{max}}$ and parameter σ_Δ, although the distributions parameters for $P_{NMR}(\Delta)$ do not match those for $P_{DC}(\Delta)$ at each respective external field. As an additional result confirming the good quality of the fit model, the values for $\tau_{0,NMR}$ lie in the range $[10^{-12}, 10^{-11}]$, i.e. well within the typical range for non-interacting superparamgnets. If one compares the NMR results with those from AC susceptibility

Sample	**Experimental parameters**		**Fit parameters**				
	H_{ext}	T_{peak}	A	$\bar{\Delta}$	σ_Δ	$\tau_{0,\mathrm{NMR}}$	$T_{P_{max}}$
	kOe	K	Oe g emu^{-1} K^{-1}	K	-	s/rad	K
1 (3nm)	3.7	42	3.24×10^6	103.09	0.786	3.24×10^{-11}	56
	14.4	42	6.54×10^6	62.33	0.963	2.60×10^{-11}	24
2 (4nm)	2.7	24	1.03×10^6	130.24	0.520	7.26×10^{-12}	98
	5.0	24	1.03×10^6	83.69	0.536	2.78×10^{-11}	62
	14.0	24	1.03×10^6	62.23	0.450	3.47×10^{-11}	50
3 (7nm)	6.5	127	8.17×10^5	977.79	0.183	1.47×10^{-12}	944
	16.5	138	1.19×10^6	415.13	0.099	7.35×10^{-11}	411
4 (12nm)	5.0	261	2.10×10^5	1688.67	0.174	1.02×10^{-11}	1640
	14.0	248	2.95×10^5	1358.85	0.085	1.05×10^{-11}	1350

Table 2.1 – Fit parameters for Eq. 2.14, applied to the analysis of nuclear spin-lattice relaxation rates. From left to right: value of the applied external field H_{ext}; peak temperature of the relaxation rates T_{peak}; prefactor A of Eq. 2.14; Average barrier $\bar{\Delta}$ and scale parameter σ_Delta of the tentative lognormal distribution of energy barriers; τ_0 prefactor of the Arrhenius expression for the correlation time τ_c (see Eq. 2.12); temperature value of the maximum of the estimated EBD.

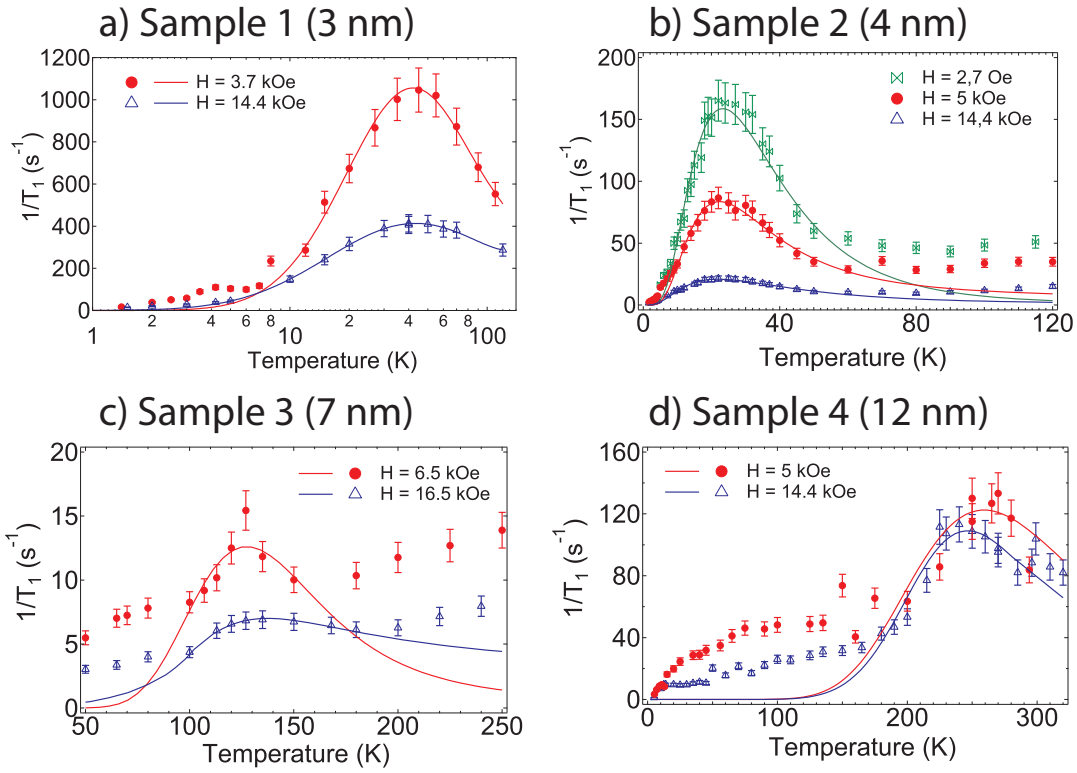

Figure 2.9 – Proton Nuclear Relaxation Rates for samples **1** – **4**, arranged from left to right, top to bottom, in order of increasing size. Only the region where nanoparticles undergo the transition from the superparamagnatic state to the blocked regime is displayed. Solid curves are the best-fits to Eq. 2.14, which is a Lorentzian spectral density function modified to account for a distribution of activation energy barriers. Output values for parameters of Eq. 2.14 are listed in Table 2.1

analysis it appears evident that the scales for the superparamagnetic relaxation correlation time do not match: from AC susceptibility $\tau_0 \sim 10^{-19} - 10^{-}11$ s/rad (Arrhenius fit) and $\tau_0 \sim 10^{-}13 - 10^{-}9$ s/rad (V.F. fit), while from NMR we have $\tau_0 \sim 10^{-12} - 10^{-}11$ s/rad (we will not consider here τ_0 results from the scaling law 1.15). In other words, parameter τ_0 in table 1.3 are at least one order of magnitude lower than $\tau_{0,NMR}$ in most cases. The inequivalence of the two approaches in estimating τ_0 should not be surprising, because in the case of AC susceptibility τ_0 is a quantity characterizing the relaxation of the particle magnetic moment as a thermodynamic process involving a single activation barrier, while $\tau_{0,NMR}$ is intimately tied to a distribution of anisotropy energy barriers.

Moreover the dynamics that τ_0 describes in the case of NMR is technically different from the one probed in the case of AC susceptibility: in the NMR case, the proton spin relaxation dynamics at a *local* level is described by a spectral density function which, in turn, includes the expression for the relaxation of the particle moment end effectively 'filters' it: $\tau_{0,NMR}$ reflects the time scale to which NMR is sensitive, since any anomaly in the NMR relaxation rates should be associated with a field fluctuation (or motion) having a correlation time $\tau_C \sim$

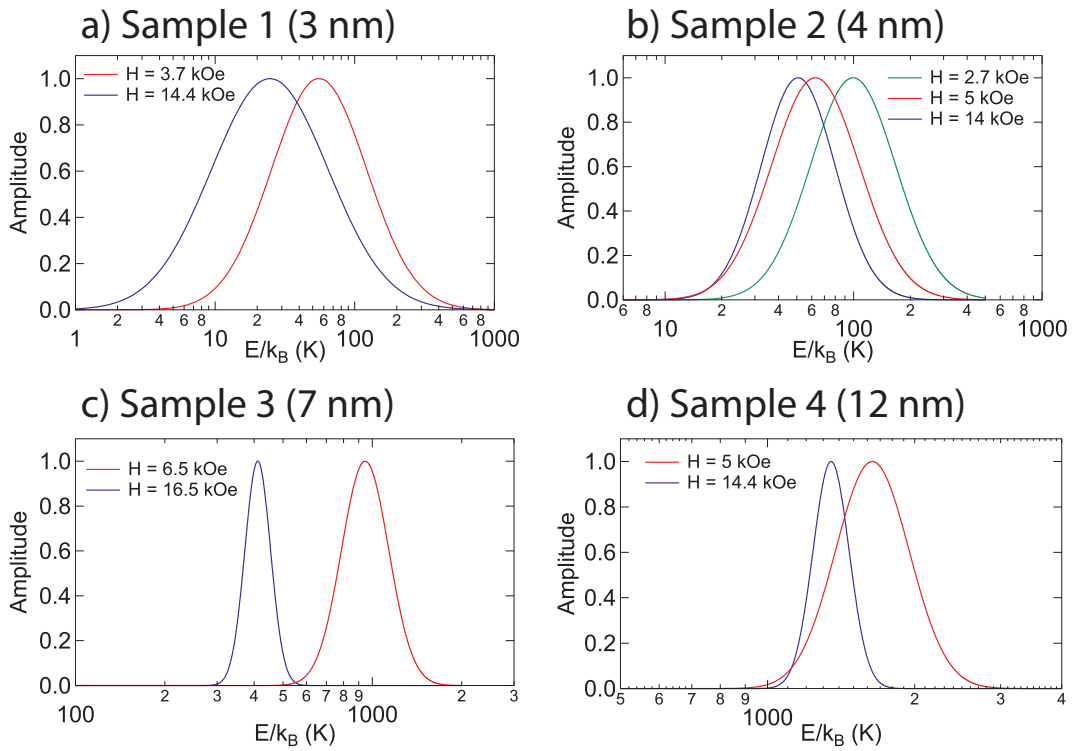

Figure 2.10 – Activation energy barrier distributions estimated by fitting the NMR nuclear spin lattice relaxation rates in Fig. 2.9 to Eq. 2.14. This panel is arranged analogously to Fig. 2.2 and 2.9. Graphs are provided with an X-Log scale, reporting the activation energy in Kelvin units, to cover the support of the broad Log-Normal distributions. Distribution maxima are rescaled to an arbitrary unit value.

$1/\omega_L$. This filtering effect is also the reason behind the disagreement between $P_{NMR}(\Delta)$ and $P_{DC}(\Delta)$ at the same external magnetic field, since information about the energy barrier sensed by the particles under an NMR experiment is fed to the spectral density function via the correlation time $\tau_c \equiv \tau_N$, so it would be correct to label $P_{NMR}(\Delta)$ (eq. 2.13) the *dynamic distribution* of activation energy barriers.

It should also be noted that AC susceptibility measurements were carried out in near zero field conditions, while NMR measurements were performed under the influence of a relatively high magnetic field. Therefore, while a decrease in the effective value of the activation energy barrier after the application of a magnetic field is expected and can be clearly observed by comparing column 5 of Table 1.3 (E_{eff}) and column 5 and 8 of Table 2.1 ($\bar{\Delta}$ and $T_{P_{max}}$), the dependence of τ_0 on the field is not known, and the comparison between AC results and NMR results should be taken with a grain of salt.

One main point of criticism about the presented NMR investigation might be that the presence of considerably strong interparticle interactions can have a non-negligible impact on the observation of a pure superparamagnetic blocking phenomenon in the chosen materials, as other competing dynamics superimpose or, eventually, take over; for instance, a transition to a spin-glass-like state.

However, it is worth noticing that a superspin-glass state is easily destroyed after the application of even a moderate magnetic field;[104] thus, any dynamic contribution that would be generated by the internal field fluctuations associated with the onset of a 'collective' glassy state at low applied static fields can be safely neglected at fields greater than $\sim 10^2$ Oe. We conclude that under the relatively intense fields of a NMR experiment ($H_0 > 10^3$ Oe) the aforementioned ambiguity is removed and no superspin-glass state can be found; hence, it is only possible to probe the superparamagnetic thermal activation of the inner shell of the ferrite core and, eventually, the effects of a faster dynamics of the disordered surface layer. An estimate of the Zeeman energy E_Z at 3.4 and 14.4 kOe yields values of the order of 10^2–10^3 erg while the particle magnetic anisotropy energy E_A as calculated from the bulk magneto-crystalline anisotropy constant $K_{\mathrm{bulk}} = 4.7 \times 10^4$ erg/cm^3 is only of the order of $10 \div 10^2$ erg. However, it is quite common to witness a difference of two orders of magnitude[105, 50, 106] between the bulk anisotropy energy density and the effective anisotropy energy density in a nanoparticle with size $d \leq 5nm$, because additional sources of anisotropy come into play (i.e., shape, surface, magnetostriction contributions, and the dipolar interaction contribution). Thus, it is not unusual to have $E_Z < E_A$ and a double-minima (or multi-minima) energy landscape even at the high fields commonly found in solid-state NMR experiments.

2.3.5 Mössbauer experiments on Sample 1

Mössbauer spectroscopy is a standard tool employed to track the evolution of the dynamic spin system with the temperature. There are by now plenty of works on the subject: Mössbauer spectroscopy has been of great value in studying the basic properties of ferromagnetic nanoparticles [107, 108, 109, 110], understanding interparticle interaction effects on magnetic ordering [111, 112, 113] and explore surface spin-canting phenomena [114, 115, 116].

In the case of Sample **1**, the phenomenology observed by NMR has been confirmed by Mössbauer spectroscopy experiments run by Dr. Mathias Kraken at the μSR, NMR and Mössbauer laboratory of Technische Universität Braunschweig, Germany.

^{57}Fe Mössbauer measurements have been performed at temperatures ranging from 4 to 300 K on an absorber with an area density corresponding to about 0.2 mg ^{57}Fe/cm^2. A conventional transmission spectrometer with sinusoidal velocity sweep was used. As source served about 12 mCi of ^{57}Co in a rhodium matrix kept at room temperature. The absorber containers were made of nylon and fixed within copper clamps. The absorbers were kept in a static He exchange gas atmosphere of about 0.2–0.4 mbar in a flow He cryostat (CRYOVAC). Temperature stability was better than 0.1 K.

Figure 2.11 shows a representative set of absorption spectra at various temperatures. Clearly visible is the gradual broadening of the magnetically split hyperfine pattern at lowest temperatures leading to a collapse to a doublet spectrum above about 50 K. This scenario is typical for relaxation spectra of very

small particles.[65]

At low temperatures the fluctuation rates of particle moments are slow compared to the nuclear Larmor precession of ^{57}Fe, and a magnetically split pattern may be observed. At high temperatures the fluctuations lead to motional narrowing, i.e. the time-averaged hyperfine magnetic field vanishes and only the nuclear quadrupole interaction in the local electric field gradient at the Fe site is observed, leading to a doublet spectrum. The collapse occurs for fluctuation rates between 10^{10} and 10^{11} s^{-1}. Due to a distribution of fluctuation frequencies caused by an inherent distribution of particle size and anisotropy energy this is not a sharp transition, instead it smeared over some temperate range.

Typically one defines the blocking temperature at the time scale of Mössbauer spectroscopy as the temperature where about 50% of the spectral area reveals magnetic hyperfine interactions, whereas the other 50% are superparamagnetic. In our case this takes place at around 45 K, which is consistent with the observation of an enhancement in the NMR NSLR at the very same temperature.

The method of analysis of Mössbauer spectra relies on the multi-level relaxation (MLR) model developed by Jones and Srivastava[117] based on the quantum-mechanical description of a homogeneously magnetized particle with the energy $E = -KV\cos\theta$, θ being the angle between the direction of the homogeneous magnetization and the easy magnetization axis of the particle. This model takes into account thermal excitations into the local energy minima and, thus, is efficiently used to quantitatively analyze the experimental Mössbauer spectra of magnetic nanoparticles.

In Fig. 2.11 we have included fits of theoretical models to the experimental data at temperatures $T = 4, 20, 30, 40$ K, although the estimate of the blocking temperature is practically independent of the method of analysis. Unfortunately, the MLR model does not describe the collapse of the magnetic hyperfine structure into a quadrupolar doublet of lines, which is observed in the experimental Mössbauer spectra of magnetic nanoparticles even more often than the collapse into a single line. This is the reason why the best fit curve in Fig. 2.11 corresponding to $T = 40$ K does not correctly reproduce the fine structure of the central doublet. Future analysis should refine these results by including the effect of quadrupolar interactions by resorting to a recently updated version of the MLR model[118], an operation that should improve the consistency of result in the whole explored temperature range.

In Fig. 1.9 (b) we have included the blocking temperature derived from the Mössbauer data in the inset. As can be seen it is in excellent agreement with the extrapolation of the AC data.

It should be noticed that spectra recorded even at the lowest temperatures still reveal a strong temperature-independent line broadening. This is in contrast to spectra recovered from other small particles of ferrites which show sharp spectra (again, see examples given in Ref. [65]). The broadening therefore cannot be related to magnetic dynamics. One may tentatively interpret this anomaly with inhomogeneous magnetic distributions of hyperfine fields due to the shell structure of the particles having strongly canted spins.

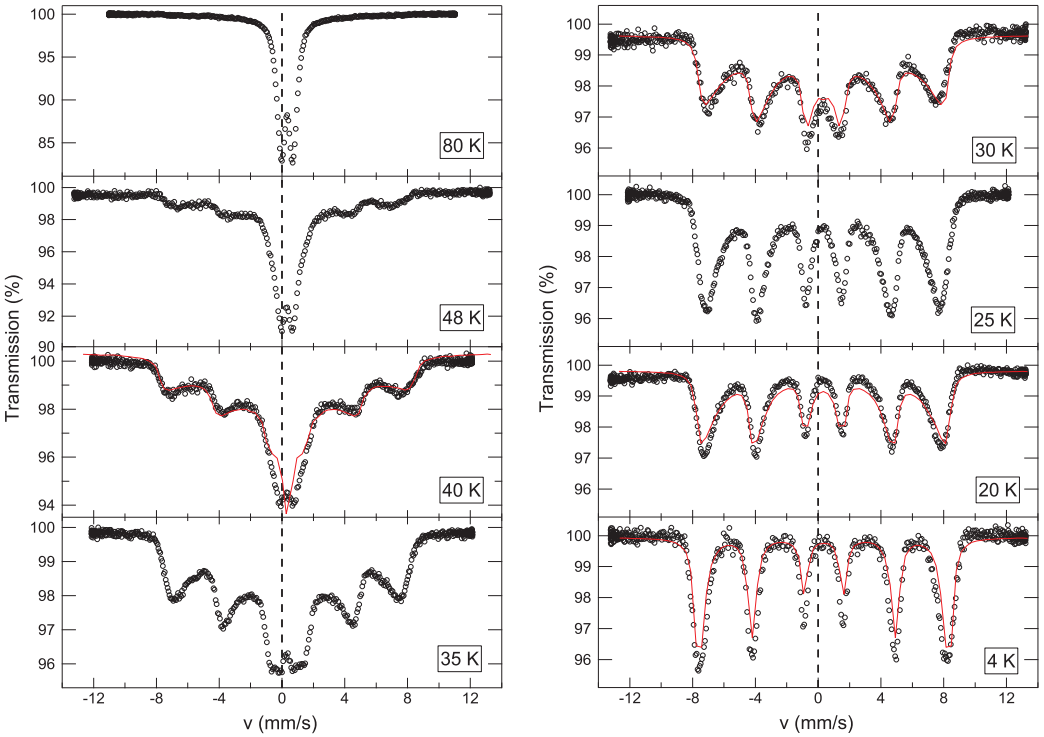

Figure 2.11 – Collection of zero-field Mössbauer spectra recorded for Sample **1** at various temperatures. The red curves overlayed to the spectrum at 40K, 30K, 20K and 4K are simulated best-fits (see text). The gradual vanishing of the six Mössbauer lines as the temperature increases is displayed, while the eventual collapse of the spectrum into a doublet near $T = 50$ K marks the blocking temperature T_B seen by the Mössbuaer experiment.

To test this possibility, Mössbauer measurements in external magnetic field have been performed, as well. Figure 2.12a reports four spectra sampled at $T = 4.35$ K and $H = 0, 20, 40$ and 60 kOe: the fraction of canted surface spins can be seen in the area of the 2nd and 5th line. Due to the polarization of the ordered core in the external field, those lines should vanish. Consequently, the higher the amount of canted surface spins, the larger the remaining area of these two lines. The normal ratios between the lines is 3:2:1 while in external field the ratio is 3:x:1 with $x < 2$. In addition, one observes an increase or decrease of the hyperfine field of the sub-spectra, due to the antiparallel alignment of the sites and the addition of the external field.

Taking a look at the data at 4.35K with 0 Oe and 60 kOe, the area of the 2nd and 5th line does indeed decrease, but not as much as what found for other iron oxide nanoparticles [97], where the lines are barely visible. This means that almost the whole particle consists of a canted spin structure and the well ordered core takes just a very little fraction.

Other measurements were performed between 4K and 12K with $H = 60$ kOe as well, to find out if the canted structure is breaking up (de-freezing) in this region, since this is the region of the low-T shoulder that was found by NMR

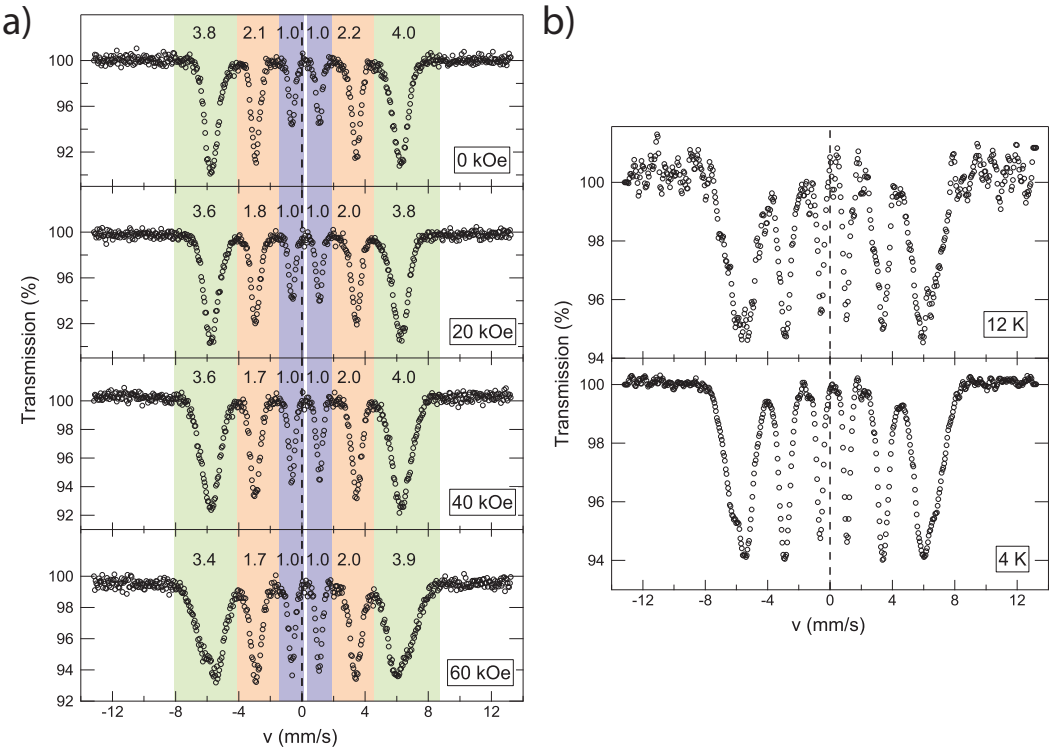

Figure 2.12 – a) In-field Mössbauer spectra recorded at $T = 4.35$ K, spanning the range $0 < H < 60$ kOe. Colored regions highlight the limits for peak integration; the area of each peak is displayed above the Mössbauer spectra. The ratio between 1st, 2nd and 3rd lines is almost field independent, supporting the hypothesis of a completely disordered magnetic state (canted spins). b) In-field Mössbauer spectra recorded at $H = 60$ kOe around 7 K, i.e. $T = 4$ K and $T = 12$ K.

in Sample **1**. The spectra recorded at 4K and 12K at 60 kOe shown in Fig. 2.12b almost look identical, indicating that the canted spin structure is already completely frozen at 12K. Hence, the low-T shoulder observed in the NSLR is actually an experimental glitch.

Although the canted nature of the low temperature magnetic order was demonstrated on Sample **1**, the microscopic factors for the formation of such state are hardly assessed. Some recent results suggest that both crystallinity and surface coating may influence the canting angles of magnetic moments of the Fe atoms in the magnetic sub-lattices of maghemite nanoparticles, being the octahedral positions more susceptible to be canted than tetrahedral ones [119, 120], a result confirmed also by ^{57}Fe-NMR[97].

2.4 Conclusions

The exploration of dynamic magnetic properties of ferrite based superparamagnetic nanoparticles by NMR revealed some interesting features; the rate of broadening of the NMR line width depends on the particle size: saturation of the line is observed almost near room temperature for large particles ($d \sim 12$ nm) and at progressively lower temperatures for smaller particles. This is related to the different temperature point for the nanoparticle magnetic moment blocking.

Confirmation of the blocking phenomenon has been found by studying the temperature dependence of the proton spin-lattice relaxation rates which have been analysed with a seminal heuristic model, accounting for the distribution of activation energy barriers for the reversal of nanoparticles magnetic moments.

The model adapts reasonably well to the experimental data, yielding an estimate of the average activation barrier characterizing the system. Inconsistencies between the so extracted distributions and results from the static magnetic analysis (see Chapter 1.3) represent a clear flaw in the model that should be addressed, although it should also be noted that the observed discordance might be related to the different measuring time-scale of the two techniques.

Other three important remarks should be pointed out: i) the insertion of a distribution of activation energies into the spectral density function ultimately modulates the representation of a *dynamic* process, i.e. information about the energy barrier sensed by the particles is fed through the correlation time $\tau_c \equiv \tau_N$, so it would be correct to label $P_{NMR}(\Delta)$ (eq. 2.13) the *dynamic distribution* of activation energy barriers; ii) equation 2.12 for the temperature dependence of the single correlation time τ_c is an approximated expression that would need further theoretical validation, especially when used in conjunction with other dynamic quantities, such as the spectral density function; iii) the choice of the Log-Normal shape for the distribution $P_{NMR}(\Delta)$ is arbitrary, and other approaches, such as inverse-problem solving algorithms, might prove useful in determining a more appropriate and general analytical expression for $P_{NMR}(\Delta)$.

An attempt at commenting the evolution of the spin dynamics of maghemite nanoparticles with particle size has been made: we propose that the pure superparamagnetic blocking/unblocking regime of the magnetic moment can be found for relatively large particles, $d > 10$ nm. As the particle size decreases, the magnetic volume splits in two distinct regions: one is made of collinear exchange coupled spins still exhibiting a superparamagnetic behavior, and localized in the inner core region of the particle; the second region covers the outer shell volume, starting from the surface and extending to the bulk spins down to a certain depth, which should not depend on the size of the particle. This last region is characterized by a magnetically disordered state, induced by the frustration emerging from unsaturated surface ion bonds; fluctuations associated with spins flip-flop events in this region are also faster than the Néel relaxation rate of the inner region superspin. Under $d \sim 4$ nm the disordered state covers

the whole particle and, again, a single correlation time describes the dynamics; the term 'superparamagnetic spin freezing' may not apply in this last scenario, anymore. This observation is consistent with what has been found in Chapter 2, where a broadening of the distribution of activation energy was found and related to the survival of a freezing phenomena at high applied magnetic fields, either coming from the SP-ordered core spins or the disordered surface spins.

The next chapter will deal with the frequency dependence of relaxation rates of iron oxide based nanoparticles at room temperature.

Chapter 3

Nanoparticle samples in solution: an NMRD investigation

3.1 Chapter overview

The following sections will present a systematic study of the NMR-D relaxivity of coated nanoparticles systems that are promising agents for MRI contrasting. Four magnetic nanoparticle systems are first introduced: magnetic material, nature of the organic coating and particle size are the three main variables considered to span a considerable range of possible combinations. The preliminary characterization with AC susceptibility measurements is then addressed; best fit values from the analysis of Néel relaxation times provide an estimate of the average activation energy barrier and of the attempt time τ_0, which works as an indicator of the superparamagnetic state of the sample. The observations made in the previous chapter about T_B, τ_0 and Δ, which basically determine the spin dynamics of a nanoparticle assembly, have been used to assist in selecting the samples for the NMRD investigation.

In subsequent paragraphs, proton relaxivity curves for the selected samples are presented, commented, and fit to an heuristic formula from Roch's theory of proton relaxation induced by superparamagnetic particles [32, 121], adapted to the present case study. Roch's model allows to follow the evolution of the relaxivity curves with the particle size, taking into account the variations of the effective magnetic anisotropy. Results of the fits are promising, and provide an estimate of the relative importance of the Zeeman and Anisotropy energies, the minimum approach distance of solvent molecules to the magnetic center and Néel relaxation time as experienced by NMR, i.e. the *local* magnetization reversal correlation time (similarly to parameter τ_N recorded in the previous chapter). The excellent performance of the chosen model is further confirmed by a comparison of relaxation times between AC susceptibility and NMR data.

Finally, an attempt at the interpretation of r_2 relaxivity profiles is described: instead of using Roch's expression for r_2 we opted for a simpler analysis, employing a very effective universal scaling law that is valid on a wide range of particle sizes.

3.2 Magnetic nanoparticles in biomedicine

In the medical sciences, magnetic properties of ferro/ferrimagnetic nanoparticles have been extensively exploited for a wide range of applications, like magneto-transport, drug delivery, magnetic field hyperthermia (MFH) and MRI. Particularly they help to improve the image contrast by altering the so called 'relaxivity' of the water protons for the MRI diagnosis of organic tissues. Typical nanoparticle systems for MRI contrasting are composed of magnetite, maghemite or hematite, but heterometallic particles are also presently studied, such as Cobalt-Ferrite, Manganese-Ferrite or Nickel-Ferrite nanoparticles. Among all materials for MRI contrasting, iron oxide nanoparticles are mostly interesting because they feature a high biocompatibility once coated by a biocompatible shell (composed of a sugar or a polymer, for instance), a very high magnetization at clinical field strengths and their synthesis route can be adjusted to obtain very small nanocrystals, with controllable shape and dispersity index. The investigated particles presented in this chapter belong to the USPIO category, i.e. Ultra-Small Superparamagnetic Iron Oxide (Nanoparticles), that include all nanoparticles with $d < 30$ nm. 30 nm is approximately the size limit that permits to evade the immuno-mechanism that would recognize and expel the particles injected into the vascular system. In addition, as said above, all particles are coated with an organic or inorganic material whose function is to maximize the suspension stability, the non-toxicity, the biocompatibility and biodegradability. Also, by carefully choosing and engineering the coating, nanoparticles can be functionalised in a variety of ways so that a single system could become a flexible tool for multi-modal diagnosis [122, 123, 124] and in-situ therapy [125, 126, 127].

3.3 Colloidal suspensions of Iron-oxide-based nanoparticles

Four series of magnetic nanoparticle contrast agent with iron oxide magnetic core size ranging from 4 nm to 20 nm have been investigated. The materials were selected in order to cover a wide range of magnetic anisotropy energies, and a re listed here below together with TEM images witnessing their very good monodispersity.

S-Mag/W Series

Rhamnose-coated magnetite NPS (S-Mag) [128]. Three Fe_3O_4 samples were synthesized by thermal decomposition of iron acetylacetonate and have controlled sizes of 4.1, 6.7 and 18.2 nm. Nanoparticles are functionalized with rhamnose derivative group according to a protocol described in Ref. [129].

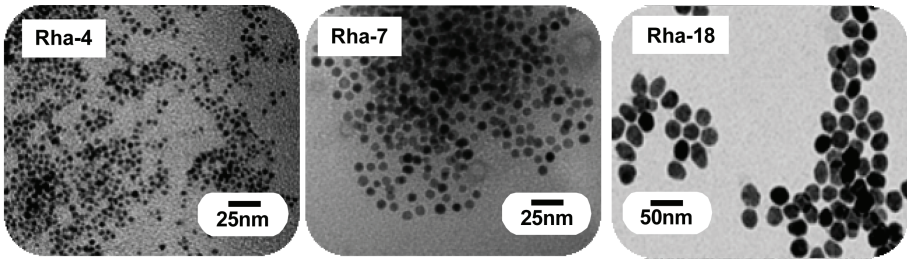

Figure 3.1 – TEM images of, from left to right, S-Mag-1, S-Mag-2 and S-Mag-3.

P-Mag/W & /T Series

Oleate coted magnetite particles (P-Mag) [34]. This monodispersed hydrophobic nanocrystals of Fe_3O_4, synthesized by thermal decomposition of iron carbonyl, have average size of 5.5, 8.0 and 12 nm, respectively and were investigated both in toluene and water solution. The transfer into aqueous media was realized by coating with an amphiphilic polymer shell (poly(maleicanhydride)) whose long aliphatic domains intercalate with oleate molecules on the nanoparticle surface. The whole organic layer including the polymer shell around the inorganic nano- crystals has a thickness of roughly 4 nm.

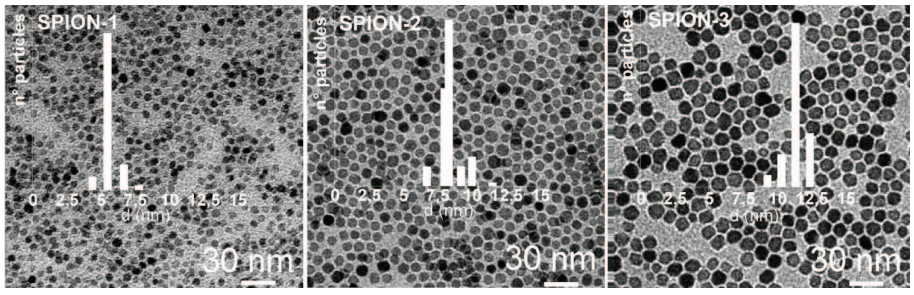

Figure 3.2 – TEM images of, from left to right, P-Mag-1, P-Mag-2 and P-Mag-3.

MnFe/T series

Oleic acid coated Manganese Ferrite nanocrystals (MnFe) [130]. $MnFe_2O_4$ NPs were synthesized by thermal decomposition of metal carbonyl complexes $Mn_2(CO)_{10}$ and $Fe(CO)_5$ in the presence of oleic acid[131]. For $MnFe_2O_4$ nanocrystals the core average sizes are 3.1, 4.9 and 5.9 nm. Average coating thickness is 3nm.

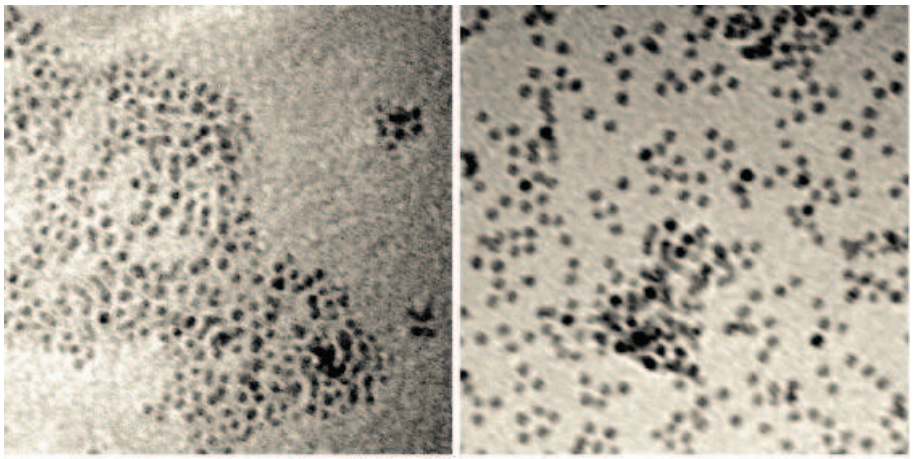

Figure 3.3 – TEM images of MnFe-1 (left) and MnFe-2 (right).

CoFe/T series

Non-stoichiometric Cobalt Ferrite ($Co_xFe_{3-x}O_4$) NPs (CoFe) with two different sizes (8.6 nm and 5 nm) and different Co content ($x = 0.2$ and $x = 0.4$). The samples were prepared by thermal decomposition of Co and Fe acetylacetonate precursors[132]. In the following, the samples will be labeled as: CoFe-1 (d = 8.5 nm, x = 0.4), CoFe-2 (d = 8.6 nm, x = 0.2), CoFe-3 (d = 5 nm, $x = 0.4$) and CoFe-4 ($d = 6$ nm, $x = 0.2$).

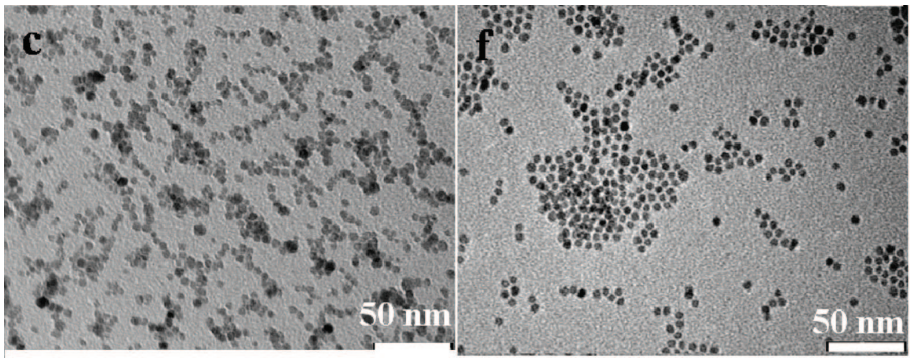

Figure 3.4 – TEM images of CoFe-1 (left), CoFe-3 (right).

Static magnetic characterization of the samples listed above can be found in references [130, 34, 128, 132]; data plots are not reported because not essential, and do not represent original work of the author of this thesis.

In this chapter, only the values of the saturation magnetization M_S are reported, for sake of clarity, in Table 3.2; such values have been extracted from DC magnetometry measurements through a fit to a formula analogous to equation 1.4 in Chapter 1. Table 3.1 also lists the average particle diameters measured by transmission electron microscopy, d_{TEM}, and by dynamic light scattering, d_{DLS}. d_{TEM} provides an estimate of the size of the inorganic magnetic core of the particles in the assembly, while d_{DLS} is a measurement of the hydrodynamic diameter. The hydrodynamic diameter is usually larger than the core particle

Sample	d_{TEM} (nm)	d_{DLS} (nm)	M_S (emu/g)
S-Mag/W-1	4.1 ± 0.6	8.2 (0.16)	77
S-Mag/W-2	6.7 ± 0.8	10.4 (0.14)	75
S-Mag/W-3	18.2 ± 1.1	23.6 (0.10)	68
P-Mag/W-1	5.5 ± 0.6	32.0 (0.49)	38
P-Mag/W-2	8.0 ± 0.8	44.0 (0.57)	52
P-Mag/W-3	12.0 ± 0.7	36.0 (0.62)	43
P-Mag/T-1	5.5 ± 0.6	9.0 (0.26)	38
P-Mag/T-2	8.0 ± 0.8	12.0 (0.30)	52
P-Mag/T-3	12.0 ± 0.7	15.0 (0.52)	43
MnFe/T-1	3.0 ± 0.2	–	44
MnFe/T-2	4.8 ± 0.1	–	44
MnFe/T-3	6.0 ± 0.2	–	42
CoFe/T-1	8.6 ± 1.1	12.0 (0.09)	80
CoFe/T-2	8.6 ± 1.1	14.0 (0.14)	80
CoFe/T-3	6.0 ± 1.4	–	72
CoFe/T-4	5.0 ± 1.2	–	56

Table 3.1 – Main magnetic parameters for sample series S-Mag (Rhamnose-coated magnetite), P-Mag (Oleic Acid-coated or polymer coated magnetite), MnFe (Oleic Acid-coated Manganese Ferrite) and CoFe (Oleic acid-coated Cobalt Ferrite). From left to right in each row: TEM estimated particle diameter, DLS particle diameter and saturation magnetization. The error on d_{DLS} is expressed as a polydispersity index in parenthesis.

diameter because it includes both the thickness of the organic coating and an additional lenght related to the hydration sphere influenced by the presence of the particle itself, depending on the degree of hydrophilicity of the system.

3.4 AC Susceptibility

In the following section the results of the AC Susceptibility analysis on the same samples are briefly reported.

AC Susceptibility measurements were performed on dry powder samples using a Quantum Design MPMS-XL SQUID and a Cryogenic S600 SQUID magnetometer, in the excitation frequency range 0.1 – 1000 Hz, the temperature range 2 – 300 K and zero static field. The values of the Néel relaxation time τ_N at room temperature were extracted and compared to the estimate of τ_N from the NMR-D data analysis, as it is shown in the next section. Similarly to the procedures followed for the samples of Chapter 2, we resorted to a double analysis of the AC data with an Arrhenius-like function and with a Vogel-Fulcher expression, since the powder form of the samples does not allow to exclude interparticle effects beforehand.

Table 3.2 lists all the results of such an analysis on all samples.

Sample	$E_{A,Arr}/k_B$ (K)	$\tau_{0,Arr}$ (s/rad)	$\tau_{N,Arr}$ (s/rad)	$E_{A,VF}/k_B$ (K)	$\tau_{0,VF}$ (s/rad)	T_0 (K)	$\tau_{N,VF}$ (s/rad)
S-Mag/W-1	1525 ± 7	$1.15 \pm 0.14 \times 10^{-13}$	$1.86 \pm 0.26 \times 10^{-11}$	639 ± 29	$5.36 \pm 0.44 \times 10^{-10}$	22.1 ± 2.1	$5.34 \pm 1.00 \times 10^{-9}$
S-Mag/W-2	1118 ± 5	$1.24 \pm 0.12 \times 10^{-12}$	$5.17 \pm 0.58 \times 10^{-11}$	885 ± 42	$1.39 \pm 0.13 \times 10^{-11}$	5.6 ± 2.0	$2.80 \pm 0.67 \times 10^{-10}$
S-Mag/W-3	8421 ± 12	$8.65 \pm 0.49 \times 10^{-21}$	$1.34 \pm 0.13 \times 10^{-8}$	1673 ± 10	$5.73 \pm 0.37 \times 10^{-11}$	113.0 ± 2.8	$4.40 \pm 0.52 \times 10^{-7}$
P-Mag/W-1	–	–	–	–	–	–	–
P-Mag/W-2	–	–	–	–	–	–	–
P-Mag/W-3	3586 ± 13	$4.74 \pm 0.62 \times 10^{-19}$	$7.36 \pm 0.13 \times 10^{-14}$	608 ± 20	$9.72 \pm 0.64 \times 10^{-10}$	57.3 ± 4.0	$1.19 \pm 0.22 \times 10^{-8}$
P-Mag/T-1	612 ± 20	$4.48 \pm 0.30 \times 10^{-15}$	$3.44 \pm 0.45 \times 10^{-14}$	612 ± 19	$4.48 \pm 0.30 \times 10^{-15}$	0.0	$3.44 \pm 0.45 \times 10^{-14}$
P-Mag/T-2	865 ± 33	$9.96 \pm 0.20 \times 10^{-11}$	$1.78 \pm 0.23 \times 10^{-10}$	763 ± 12	$2.90 \pm 0.82 \times 10^{-10}$	2.9 ± 1.0	$3.78 \pm 0.12 \times 10^{-9}$
P-Mag/T-3	636 ± 7	$4.47 \pm 0.84 \times 10^{-11}$	$3.72 \pm 0.79 \times 10^{-9}$	621 ± 18	$5.40 \pm 0.33 \times 10^{-10}$	0.5 ± 0.1	$4.29 \pm 0.52 \times 10^{-9}$
MnFe/T-1	189 ± 2	$7.14 \pm 0.34 \times 10^{-13}$	$1.34 \pm 0.72 \times 10^{-12}$	189 ± 8	$7.14 \pm 0.34 \times 10^{-13}$	0.0	$1.34 \pm 0.10 \times 10^{-12}$
MnFe/T-2	–	–	–	–	–	–	–
MnFe/T-3	1796 ± 8	$9.10 \pm 0.10 \times 10^{-14}$	$3.62 \pm 0.50 \times 10^{-11}$	1036 ± 6	$3.50 \pm 0.37 \times 10^{-11}$	17.3 ± 3.0	$1.36 \pm 0.17 \times 10^{-9}$
CoFe/T-1	–	–	–	–	–	–	–
CoFe/T-2	13569 ± 17	$7.13 \pm 0.46 \times 10^{-25}$	$3.14 \pm 0.38 \times 10^{-5}$	3784 ± 12	$1.31 \pm 0.85 \times 10^{-15}$	127.3 ± 9.0	$4.32 \pm 0.31 \times 10^{-5}$
CoFe/T-3	2611 ± 7	$2.68 \pm 0.23 \times 10^{-15}$	$1.62 \pm 0.18 \times 10^{-11}$	1094 ± 5	$5.21 \pm 0.42 \times 10^{-11}$	32.6 ± 4.0	$3.11 \pm 0.31 \times 10^{-9}$
CoFe/T-4	2661 ± 5	$4.32 \pm 0.20 \times 10^{-14}$	$3.07 \pm 0.19 \times 10^{-10}$	1668 ± 33	$8.26 \pm 0.35 \times 10^{-12}$	21.8 ± 2.0	$3.31 \pm 0.53 \times 10^{-9}$

Table 3.2 – Main magnetic parameters for sample series S-Mag (Rhamnose-coated magnetite), P-Mag (Oleic Acid-coated or polymer coated magnetite), MnFe (Oleic Acid-coated Manganese Ferrite) and CoFe (Oleic acid-coated Cobalt Ferrite), sorted by magnetic core diameter. From left to right in each row: TEM estimated particle diameter and standard deviations in parentheses, saturation magnetization, Arrhenius law estimate of the anisotropy energy barrier, τ_0 prefactor and Néel relaxation time, Vogel Fulcher law's estimate of the anisotropy energy barrier, τ_0 prefactor, T_0 phenomenological parameter and Néel relaxation time.

The effect of the different magnetic ion is mainly noticeable on the E_A parameters: sample with roughly the same dimensions results in different values for the energy barrier. For instance the CoFe samples have much higher barriers than magnetite (see, samples CoFeT-3 and CoFeT-4). Also, T_0 increases with d_{TEM}, since the particles with the higher magnetic moments will interact more strongly with each other. Inside each series the barrier increases with size, as it would be expected, even though unexplained exceptions occurs; for instance sample P-Mag/T-3 should feature a much broader energy barrier, being the largest particle of the series, yet it does not.

Additionally, it does not seem to subsist any definite size-dependence of the τ_0 values. For the samples S-Mag/W-2, P-Mag/T-2 and P-Mag/T-3 the values of the pre-exponential factor τ_0 are in the range 10^{-9} – 10^{-12} s typical for isolated superparamagnetic nanoparticles, while for other samples the values of E_A and τ_0, are higher and smaller, respectively, than those usually observed in non-interacting systems.

The values for parameters E_A and τ_0 obtained with the V-F, on the other hand, are in the typical range for superparamagnetic systems in most cases, but for the two cases of P-Mag/(T&W)-1 and MnFeT-1, the T_0 is zero (see Table 3.2). This is a limit case where the V-F expression reverts back to the Arrhenius case ($T_0 \to 0$). τ_0 seem to increase for the bigger particles: as seen in Chapter 1, this occurence may be related to the onset of a collective state induced by interparticle interactions, such as a supersping-glass state. The emergence of dipolar interactions can be ascribed to the nature of the samples used for AC measurements, which were in powder form or concentrated solutions of nanoparticles.

It has to be noticed that particles in diluted solutions, such as those employed in the NMR dispersion experiments, should be considered as non interacting. The AC susceptibility technique provides sample-averaged results, while NMR is a local probe, consequently less sensitive to the effects of long range dipolar interparticle interactions in solution: the diffusional motions of the particles tend to average the short range interaction to zero and the long range interactions to a negligible amount [133]. None-the-less, a comparison can be attempted between the AC results and the NMR parameters, as we will show in the next section.

3.5 Longitudinal and transverse relaxivity measurements

The ^{1}H NMR relaxometry characterization (i.e. NMR Dispersion profile) of the samples has been performed at room temperature by measuring the longitudinal (and the transverse, not reported) nuclear relaxation time T_1 in the frequency range 10 kHz $\leq \nu \leq$ 60 MHz, corresponding to an external magnetic field H = 2.3 – 15000 Oe. The range was chosen in order to cover the typical

fields for MRI tomographs, used both in clinics (H = 0.2, 0.5 and 1.5T) and research laboratories. Two different FT-pulsed NMR spectrometers have been employed to study the nuclear relaxation: 1) a Fast Field cycling (FFC) NMR relaxometer (STELAR Smart Tracer) working in the frequency range 10 KHz to 10 MHz; 2) a conventional NMR spectrometer (STELAR Spin Master) to cover the frequency range 10 MHz to 60 MHz. Signal detection and generation was accomplished by using standard radio frequency pulse excitation sequences based on CPMG and Hahn echo.

We shall first review each series separately:

a) S-Mag/W Series

The sugar coated magnetite series consists of three samples with very different core diameters. This wide excursion impacts strongly on the relaxivity curves: a plateau at low frequencies shows that the magnetic anisotropy leads the nuclear relaxation rates and a maximum at higher frequencies marks the onset of the Curie relaxation as the main driving Mechanism. This maximum shifts toward lower frequencies when the particle diameter is increased, because the condition $\omega_H \tau_D \sim 1$ is met earlier during the frequency-sweep. For the smaller particles a dispersion is observed at low frequencies, while for higher particle diameters the dispersion disappears because the effective magnetic anisotropy increases, as shown by the values of E_A estimated by AC susceptibility. The maximum in r_1 disappears for the 18.2 nm sample and the behavior can be described by the Ayant's spectral density alone. The disappearance of the maximum can also occur if, fixed the particle dimension, a material with higher Anisotropy energy density is used, as it is the case of CoFe samples (see later on).

r_2 experiments reveal that in samples S-Mag with $d > 5 - 6$ nm the trans-

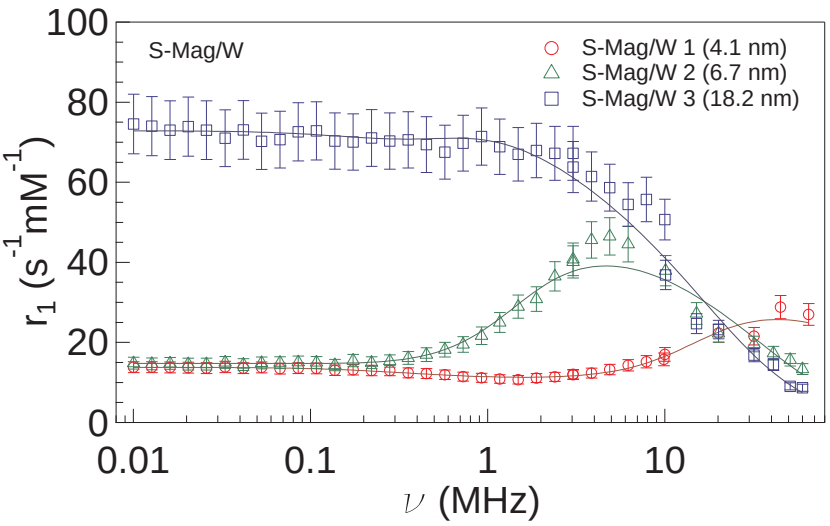

Figure 3.5 – Longitudinal relaxivities for series S-Mag/W. Best Fit curves to Roch's model (see Eq. 3.8) are plotted as solid lines.

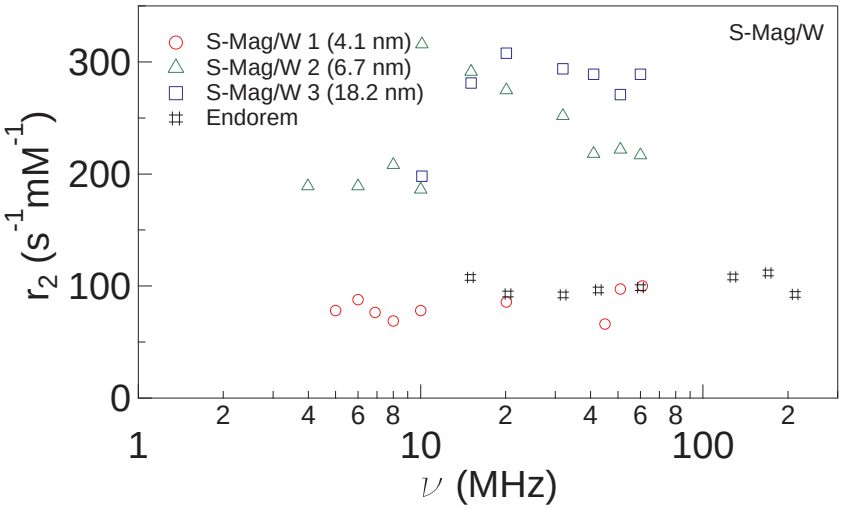

Figure 3.6 – A comparison of r_2 relaxivities for the S-Mag/W samples and Endorem.

verse relaxivity is, remarkably, three times higher than Endorem. Also, further increasing the size of the nanoparticles does not result in any additional enhancement of r_2. This last observation might prove useful when tuning the size of sugar-coated magnetite for the creation of contrast agents. As for all the other investigated samples, r_2 does not depend on the applied static field and/or measurement radiofrequency.

c) P-Mag/W Series

This series is qualitatively similar to the S-Mag/W series, although we did not notice the marked displacement of the maximum of $(r_1)_{max}$ as we did in the S-Mag/W series. Also, the peak is not inglobated in the low-frequency plateau even for large particles, which however here limit to 12 nm diameter instead of 18 nm. This could be also due to a different depth of penetration of water molecules into the polymeric shell with respect to the sugar shell of series S-Mag/W. Comparing the P-Mag/W Series with the S-Mag/T series it is clear that, at equal size, the choice of a different coating does not have a significant impact on the behavior of r_1. On the other hand r_2 is quite affected by the nature of the surfacting material: the r_2 values are lower than or comparable to both Sinerem and Endorem, while increasing the particle size does not lead to a higher r_2 value, on the contrary, the maximum observed values were found on the 8 nm sample.

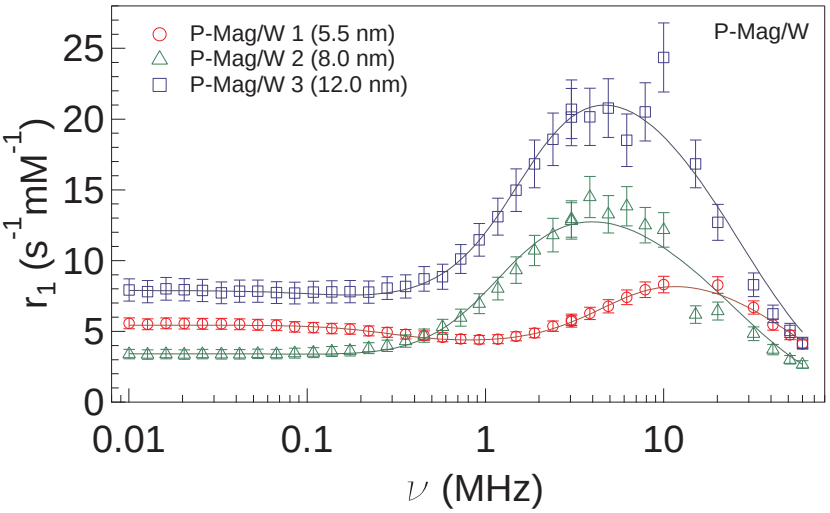

Figure 3.7 – Longitudinalrelaxivities for series P-Mag/W. Best Fit curves to Roch's model (Eq. 3.8) are plotted as solid lines.

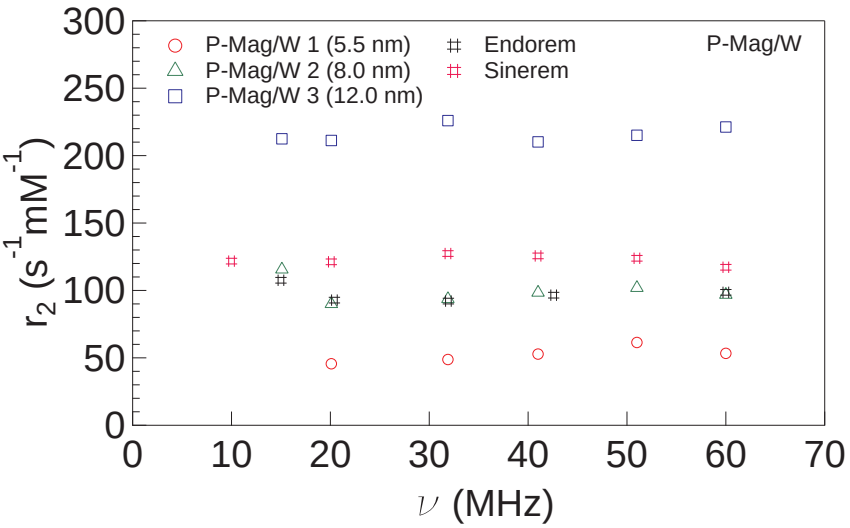

Figure 3.8 – r_2 relaxivities for the P-Mag/W sample series, Endorem and Sinerem.

c) P-Mag/T Series

A transfer of the magnetite particles in an apolar medium such as toluene does not significantly change the profile of NMR-D longitudinal relaxivity curves. The only qualitative visible difference is in the position of the flex point at high frequency, which lies beyond the investigated range for all samples in the P-Mag/T series. We will see that this feature can be better appreciated through a quantitative analysis of the data. r_2 values remain under the Sinerem-Endorem levels, even though the absolute values are quite different from P-Mag/W series; for instance, now the 12 nm sample is outperforming the 8 nm sample.

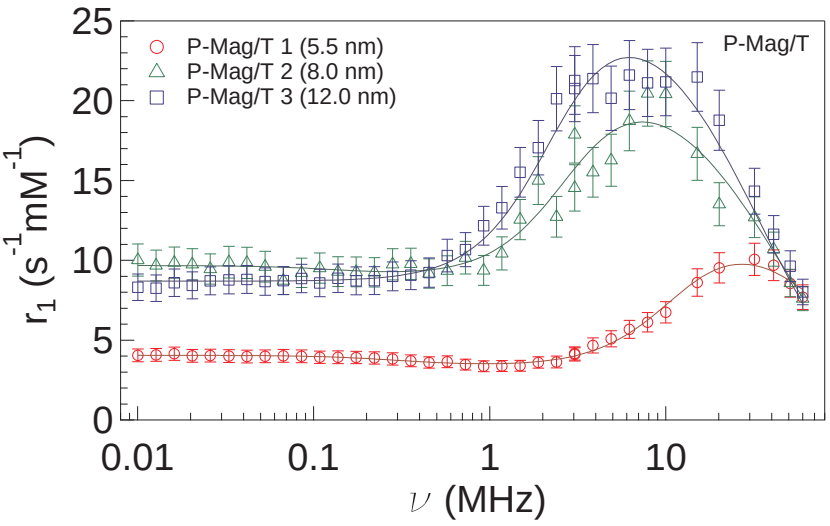

Figure 3.9 – Longitudinal relaxivities for series P-Mag/T. Best Fit curves to Roch's model (Eq. 3.8) are plotted as solid lines.

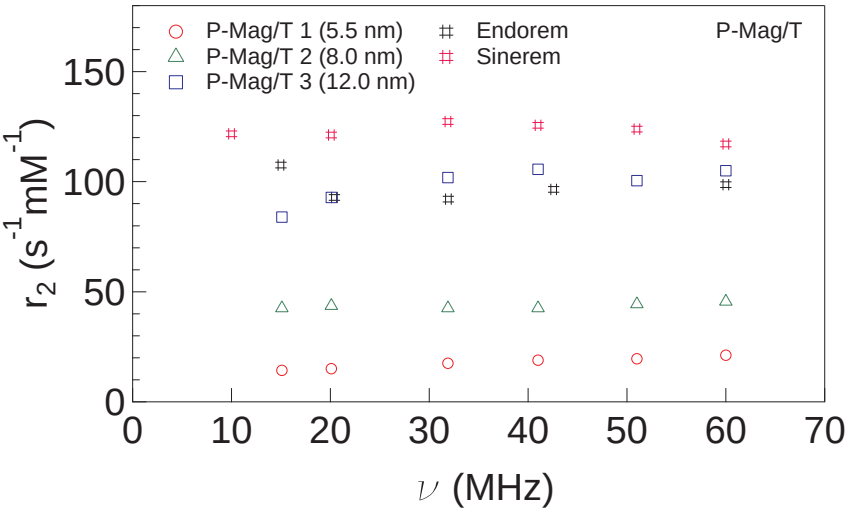

Figure 3.10 – Transverse relaxivities reported in the lower graph show that changing the solvent material seems alter the r_2 values of the larger samples of the P-Mag/T series. The smallest particles ($\sim$ 5.5 nm) on the other hand, are not significantly affected. (Refer to Fig.3.8)

d) MnFe/T series

MnFe has a lower value for the bulk magnetic anisotropy energy density with respect to magnetite. Coupled to a narrower size range this leads to very similar r_1 curves for all samples, although it is still possible to appreciate the variation in the low-frequency dispersion region, which is flatter for the largest sample. Both r_1 and r_2 values are lower with respect to the S-Mag and P-Mag samples, probably because the particle are smaller and also because the samples mass magnetizations are lower (see Tab 3.2).

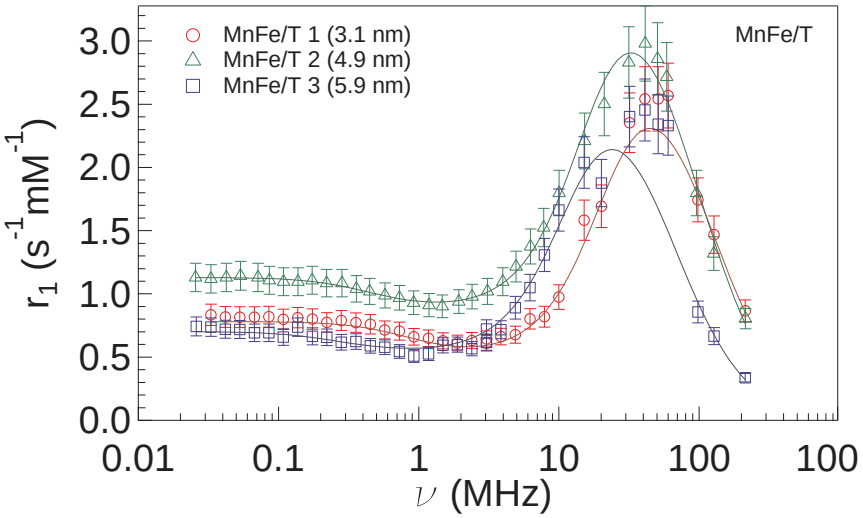

Figure 3.11 – Longitudinal relaxivities for series MnFe/T. Best Fit curves to Roch's model (Eq. 3.8) are plotted as solid lines. A comparison between the r_2 relaxivities for the MnFe/W samples and the r_2 relaxivity of Endorem is provided in the lower graph.

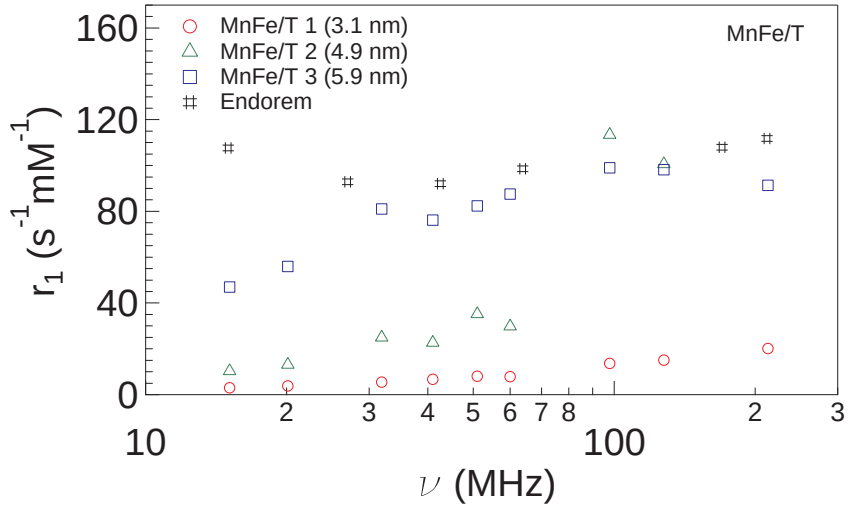

Figure 3.12 – A comparison between the r_2 relaxivities for the MnFe/W samples and the r_2 relaxivity of Endorem.

e) CoFe/T series

Cobalt Ferrite particles have the highest magnetic anisotropy energies among all samples. For this reason the disappearance of the peak occurs in particles much smaller than the ones in the magnetite series. It is also remarkable how a difference in the r_1 dispersion at low frequencies can be appreciated between the samples with x = 0.4 and those with x = 0.2. The r_2 relaxivities measured on samples CoFe-1 and CoFe-2 represent the best result of this investigation, in terms of contrast efficiencies, with a 400% gain over Endorem.

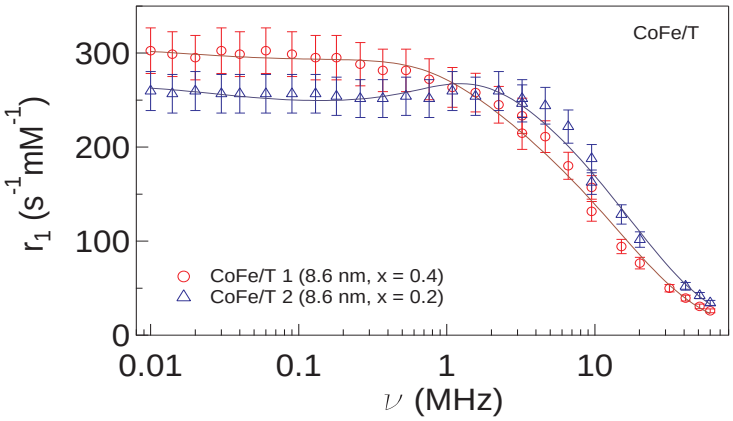

Figure 3.13 – Longitudinal (r_1) relaxivity profiles for the Samples CoFe/T-1 ($x = 0.4$) and CoFe/T-2 ($x = 0.2$), both having $d = 8.6$ nm.

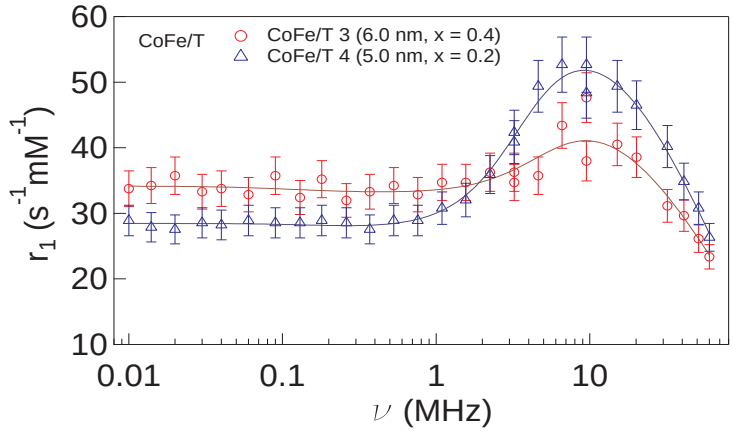

Figure 3.14 – Longitudinal (r_1) relaxivity profiles for the Samples CoFe/T-3 ($x = 0.4$) and CoFe/T-4 ($x = 0.2$), both having $d = 6$ nm and $d =\sim 5$ nm, respectively

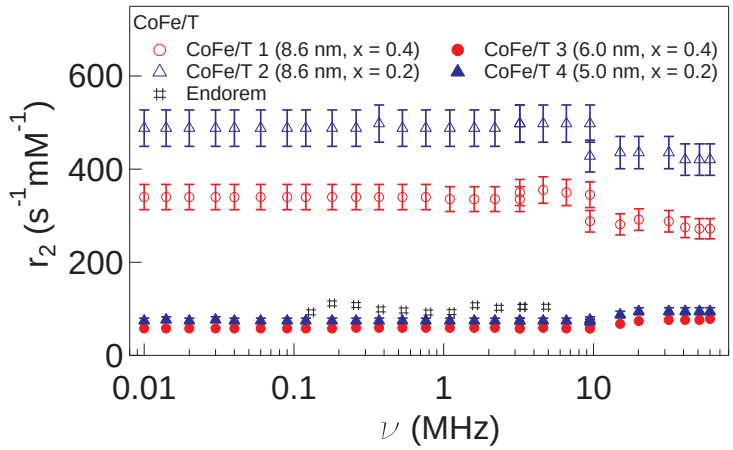

Figure 3.15 – Transverse relaxivities of CoFe/T samples 1 to 4. The very high values ofr_2 yielded by the 8.6 nm indicate a very high contrasting power, outperforming the commercial compound Endorem by almost an order of magnitude.

3.6 Proton relaxivity models and Roch's theory

The quantity universally chosen to characterize the efficiency of a contrast agent is the transverse or longitudinal relaxivity, depending on the type of contrast agent. The relaxivity r_i, where $i = 1$ stands for longitudinal relaxivity and $i = 2$ is for transverse relaxivity, is formally defined by the formula:

$$r_i = \frac{\left(\frac{1}{T_i}\right)_{meas} - \left(\frac{1}{T_i}\right)_{ref}}{C} \tag{3.1}$$

where C is the magnetic center concentration, $(1/T_i)_{meas}$ and $(1/T_i)_{ref}$ are, respectively, the characteristic nuclear magnetization relaxation rate in a solution containing the contrast compound and the relaxation rate for the reference pure solvent.

The reasoning behind such definition lies in the behavior of the sampled NMR signal: if we consider an experiment with repeated sequences, the available transverse magnetization, which is directly proportional to the signal, will depend upon the sequence repetition time T_R and the intrinsic T_1 and T_2 parameters of the irradiated region. It can be shown that the MRI signal at a certain time t takes the following form[134]

$$s(t) \propto M_{\perp}(T) = M_0(1 - e^{-\frac{T_R}{T_1}})e^{-\frac{t}{T_2}} \tag{3.2}$$

where M_0 is the total nuclear magnetization at the beginning of the sequence. As it is clear from Eq. 3.2, the MRI signal can be tuned to achieve different strengths depending on the values of parameters T_1 and T_2. Indeed, the role of a contrast agent is to enhance the contrast of the MRI image by changing the magnetic environment of the water protons in the treated tissues of interest, and thus the T_1 and T_2 relaxation times, providing measurable difference between normal and pathologic conditions in vivo. Those contrast agents that act mainly on the values of T_1 are labeled 'positive contrast agents' since the final effect is usually an enhancement of the signal (brilliant spots where the CA is delivered; conversely, 'negative contrast agents' lower the MRI signal (dark spots) because, due to their high electronic magnetization, they modify the local values of T_2 by creating a very dishomogeneous magnetic environment over the probed region. A high value of r_i at the probing frequencies of diagnostic MRI machines is an index of good contrast since the difference between the relaxation rates in the tissues reached by the agent and the adjacent agent-free regions is high.

The most famous model of paramagnetic relaxation in diluted (i.e. non-interacting) magnetic nanoparticles consider two distinct contributions to the dynamics: the Inner Sphere (IS) and the Outer Sphere (OS) contributions. The IS mechanism assumes that it is possible to identify a spherical volume of solvent molecules that experience the magnetic interaction with the electronic spin of the paramagnetic center, named the 'first coordination sphere'. It is

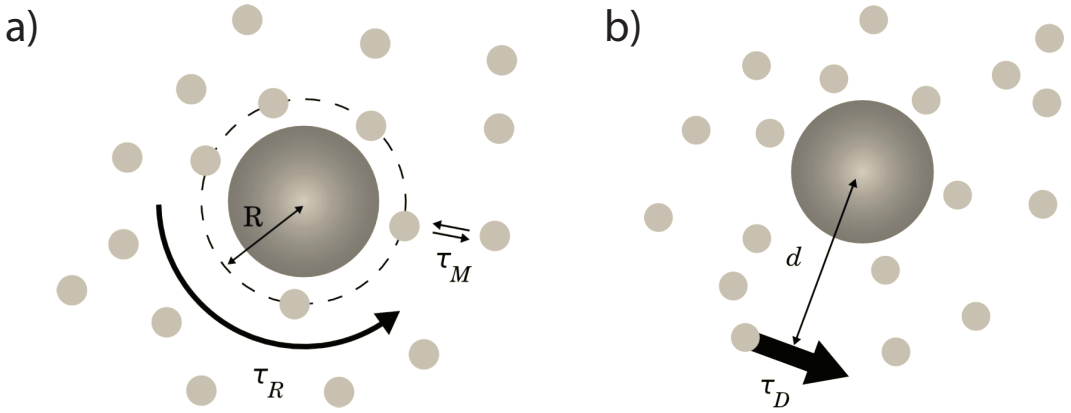

Figure 3.16 – Schematic illustration of a) Inner Sphere Model and b) Outer Sphere Model; the light-colored spheres represent water molecules, while the bigger dark-colored sphere is the paramagnetic center. The first coordination sphere, with radius R, is enclosed by the dashed line. In a) solvent molecules are exchanged in and out of the first coordination sphere, at a rate equal to $1/\tau_M$, where τ_M is the characteristic time for the molecular exchange process (or time of permanence of the solvent molecule in the first coordination sphere). The paramagnetic center is also free to rotate, τ_R being the associated rotational correlation time. In b) the simplified relaxation mechanism takes into account the classic dipolar interaction between proton spins of the solvent molecules and the magnetic center, modulated by the solvent diffusion process, having correlation time τ_D.

also assumed that solvent molecules are continually exchanged in and out of the bounding sphere enclosing the bulk solvent molecules, with no net change in the total number of molecules in the sphere. This contribution is described by a quite complicated functional form by Solomon, Bloembergen and Morgan[135, 136] that takes into account various correlation times that take part in the relaxation mechanism:

$$r_1^{IS} = CC' \frac{1}{T_1 - \tau_M} \tag{3.3}$$

C is the concentration of paramagnetic centers, C' is the number of solvent molecules in the first coordination sphere, τ_M is the time of permanence of the solvent molecule in the spherical volume. T_1 is given, in SI units, by

$$\frac{1}{T_1} = \frac{2}{15}\left(\frac{\mu_0}{4\pi}\right)^2 \gamma_H^2 \gamma_S^2 \hbar^2 S(S+1) \frac{1}{R^6} \left[\frac{3\tau_{c1}}{1+(\omega_H \tau_{c1})^2} + \frac{7\tau_{c2}}{1+(\omega_S \tau_{c2})^2}\right] \tag{3.4}$$

with

$$\begin{aligned}
\frac{1}{\tau_{ci}} &= \frac{1}{\tau_R} + \frac{1}{\tau_M} + \frac{1}{\tau_{Si}} \\
\frac{1}{\tau_{S1}} &= \frac{1}{5\tau_{S0}} \left[\frac{1}{1+(\omega_S\tau_V)^2} + \frac{4}{1+4(\omega_S\tau_V)^2} \right] \\
\frac{1}{\tau_{S2}} &= \frac{1}{10\tau_{S0}} \left[3 + \frac{5}{1+(\omega_S\tau_V)^2} + \frac{2}{1+4(\omega_S\tau_V)^2} \right].
\end{aligned}$$

- γ_S and γ_H: gyromagnetic ratios of electron and proton;
- ω_S and ω_H: Larmor precession frequency for electron and proton;
- R: radius of the first coordination sphere;
- τ_{c1} and τ_{c2}: magnetic correlation time for the interactions between the paramagnetic center and the solvent molecule for longitudinal and transverse relaxation, respectively.
- τ_{S1} and τ_{S2}: longitudinal and transverse electronic relaxation time. τ_{S0} is the τ_{Si} value in zero magnetic field.
- τ_R: rotational correlation time of the reorientation of the electronic spin of the paramagnetic center due to Brownian motion.
- τ_V: characteristic correlation time of electronic relaxation.

The OS mechanism, on the other hand, describes the paramagnetic relaxation due to the long range dipolar interaction between the proton spins of the solvent molecule and the electronic spin of the paramagnetic center. This contribution is given by the expression by Freed [137] :

$$r_1^{OS} = \frac{6400\pi}{81} \left(\frac{\mu_0}{4\pi}\right)^2 \gamma_H^2 \gamma_S^2 \hbar^2 S(S+1) N_A \frac{C}{dD} [7J^F(\omega_S, \tau_D, \tau_{S1}) + 37J^F(\omega_H, \tau_D, \tau_{S1})] \quad (3.5)$$

where

$$J^F(\omega, \tau_D, \tau_{S1}) = \mathrm{Re}\left\{ \frac{1 + \frac{1}{4}(i\omega\tau_D + \frac{\tau_D}{\tau_{S1}})^{\frac{1}{2}}}{1 + (i\omega\tau_D + \frac{\tau_D}{\tau_{S1}})^{\frac{1}{2}} + \frac{4}{9}(i\omega\tau_D + \frac{\tau_D}{\tau_{S1}}) + \frac{1}{9}(i\omega\tau_D + \frac{\tau_D}{\tau_{S1}})^{\frac{3}{2}}} \right\}$$

$\tau_D = d^2/D$ is the diffusion time of the solvent, being d and D the distance of minimum approach of the solvent molecule to the magnetic center and the diffusion coefficient, respectively.

If instead of a paramagnetic center we consider a superparamagnetic particle, i.e. the case of the present thesis, the IS contribution becomes negligible with respect to the OS mechanism; the OS model must be also slightly modified to

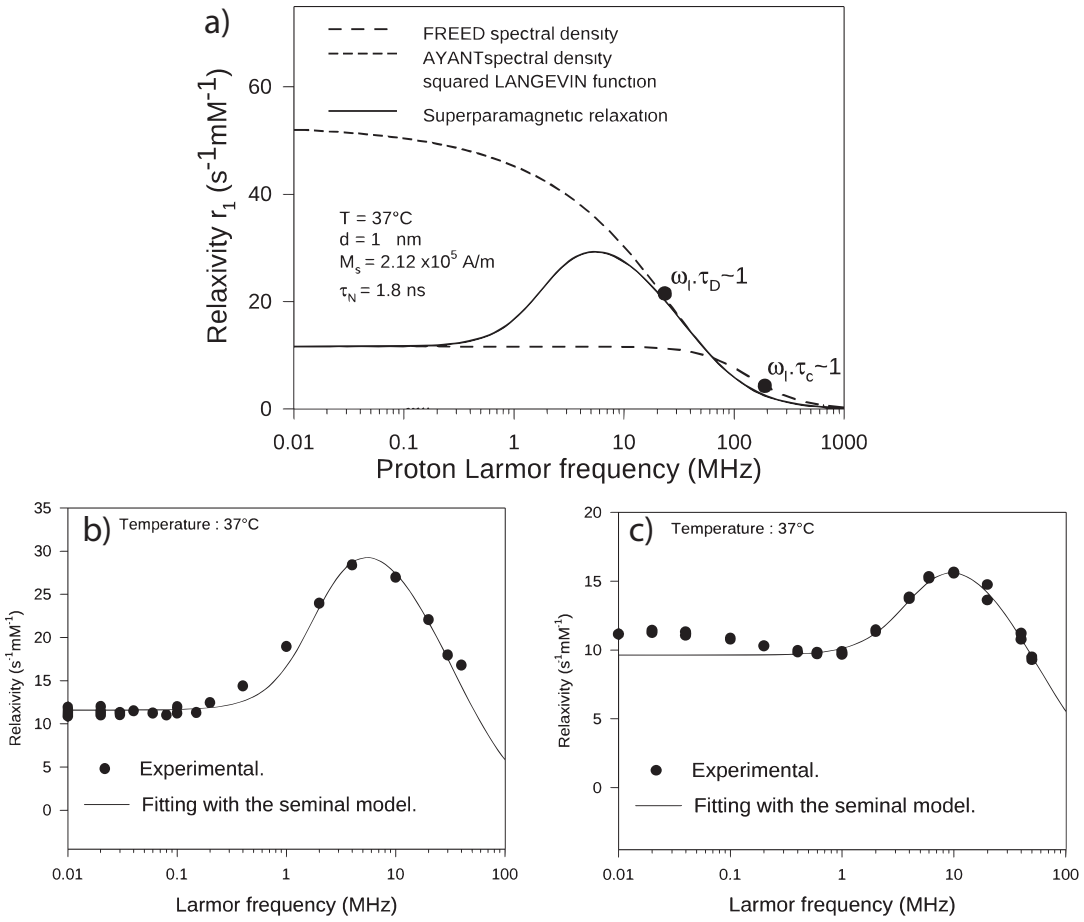

Figure 3.17 – a) Simulated longitudinal relaxivity r_1 curves for a superparamagnetic material from Roch's model. The various contributions to the relaxivity are reported: in the low frequency region the relaxation process is dominated by the Freed spectral density; the cut-off for Freed's contribution falls in the high-frequency region but it is not visible, since Ayant spectral density describe relaxivity in such frequency range. The two graphs at the bottom of the panel show limit cases for superparamagnetic materials with (b) high magnetic anisotropy (i.e. same case of picture *a*) and (c) low magnetic anisotropy (the low-frequency dispersion is clearly noticeable below 1 Mhz).

take into account the effect of Néel relaxation to the modulation of the dipolar electron-nuclear interaction between the superparamagnetic particle and the protons in the solvent molecules.

The results in the case of a superparamagnetic center are schematically reproduced in Fig. 3.17a and 3.17b, that display a typical longitudinal relaxivity for colloidal suspensions of superparamagnetic particles. Two distinct regime can be detected:

a High fields / frequencies regime: the average magnetization of the system lies along the external magnetic field direction when the field strength is high, then Néel's relaxation time, τ_N, is very long ($\tau_N \to \infty$). The main contribution is provided by the diffusion of solvent molecules in the dishomogeneous field in the proximity of the magnetic nanoparticle. The resulting relaxation

is called 'Curie relaxation' because it is directly proportional to the squared average magnetization, which in turn is field dependent via the Langevin function. The Ayant $J^A(\omega_N, \tau_D)$ expression[138] for the spectral density can then be substituted to Freed's formula:

$$\begin{aligned} J^A(\omega, \tau_D) &= \frac{1 + \frac{5}{8}z + \frac{z^2}{8}}{1 + z + \frac{2}{3}z^2 + \frac{4}{81}z^4 + \frac{z^5}{81} + \frac{z^6}{648}} \\ z &= \sqrt{2\omega\tau_D} \end{aligned}$$

J^A is simply the limit of JF when the correlation time characterizing the magnetization fluctuations becomes infinitely long. This regime holds only at those field/frequencies above the condition $\omega_H\tau_D \sim 1$, that is, for fields so high that the correlation times for diffusion processes are comparable to the period of the nuclear Larmor precession.

b Low fields / frequencies regime: the magnetic anisotropy dominates and hampers the magnetization reversal along the easy axis. Longitudinal relaxivity is obtained constraining the OS model to the limitation that magnetization should preced around the field axis, because the magnetic anisotropy blocks it along the easy magnetization axis. Then Freed's expression conveniently describes this range.

The intermediate region is simply described by a linear combination of high fields and low fields contributions, weighted with factors depending on the squared Langevin function.

The model works on crystals larger than 15 nm but fails at lower sizes because the lower values for the anisotropy energy do not allow to assume that at any time the particle magnetization is parallel to the anisotropy axis. Indeed, experimental data measured on small crystals feature a slight 'low-field dispersion' that is not described by the classical OS model, as it is displayed in Fig. 3.17c. The missing step is to consider the role of the magnetic anisotropy in the relaxation process.

An efficient solution was provided by A. Roch et al in Ref. [32]: resorting to quantum formalism, the authors solved the problem in the case of a crystal with one axis of easy magnetization, starting from first principles such as basic interactions among the spins of the superparamagnetic particle and the protons spins of the solvent, accounting for the magnetic energy levels and their populations.

The authors made a number of assumption, such as: 1) each superparamagnetic particle is assigned a single magnetic moment due to the superspin, thus ignoring the internal magnetic dynamics of the particle; 2) The reorientation time is assumed to be much shorter than the particle rotation correlation time τ_R (Brown relaxation), i.e. $\tau_N \ll \tau_R$. Since τ_N depends on the particle size d through an exponential law while τ_R is directly proportional to d, this assumption is valid only for small nanoparticles, which is the starting work hypothesis.

3) τ_N is also independent of the population configuration of the magnetic energy levels of the particle. This condition is fulfilled if the level occupation probability is the same for all levels, i.e. when the anisotropy energy is low.

Under this assumption, the intrinsic electronic Hamiltonian is given by:

$$\mathcal{H} = \mathcal{H}_{ex} + \mathcal{H}_Z + \mathcal{H}_A \tag{3.6}$$

where the addenda in the right hand term are, respectively, the exchange hamiltonian, the Zeeman-coupling energy and the magnetic anisotropy energy. The assumption that the crystal magnetization should be considered as a single magnetic moment (superspin) implies that the exchange interaction is the dominating term since in this way all N iron spins would be aligned along the same direction and the total magnetization would be N times the electronic magnetic moment of the single ion. Then, the exchange term can be safely excluded from the description of the system.

Equation 3.6 is then rewritten as:

$$\mathcal{H} = \mathcal{H}_Z + \mathcal{H}_A = -\gamma_S \hbar \mathbf{H} \cdot \mathbf{S} - E_A(\mathbf{u}_S \cdot \mathbf{u}_A)^2 \tag{3.7}$$

where S is the crystal superspin, γ_S is the electron gyromagnetic ratio, H is the external magnetic field, $\mathbf{u}_S$ is the unitary vector aligned along S and $\mathbf{u}_A$ is a unitary vector pointing in the direction of the anisotropy axis of the crystal.

The analitycal result of Roch's model for the longitudinal and transverse relaxivity in a colloidal suspension of superparamagnetic nanoparticles with uniaxial anisotropy is expressed as follows:

$$\begin{aligned}
\frac{1}{T_1} \quad = \quad & \frac{32\pi}{135000}\hbar^2\gamma_S^2\gamma_I^2\left(\frac{N_A C}{RD}\right)\left\langle \sum_{i,j}\frac{\exp(-\beta E_i)}{Z}\left\{\frac{(S_{-,ij}S_{+,ji}+S_{+,ij}S_{-,ji})}{2}\cdot\right.\right. \\
& \cdot\left[\frac{1}{2}J^F(\omega_I-\omega_{ij},\tau_D,\tau_N)+3J^F(\omega_I-\omega_{ij},\tau_D,\tau_N)\right] \\
& \left.+3|S_{z,ij}|^2\frac{(J^F(\omega_I-\omega_{ij},\tau_D,\tau_N)+J^F(\omega_I+\omega_{ij},\tau_D,\tau_N))}{2}\right\}+ \\
& \left.-3\langle S_z\rangle^2[J^F(\omega_I,\tau_D,\tau_N)-J^A(\sqrt{2\omega_I\tau_D})]\right\rangle
\end{aligned} \tag{3.8}$$

$$\begin{aligned}
\frac{2}{T_1} \quad = \quad & \frac{32\pi}{135000}\hbar^2\gamma_S^2\gamma_I^2\left(\frac{N_A C}{RD}\right)\left\langle \sum_{i,j}\frac{\exp(-\beta E_i)}{Z}\left\{\frac{(S_{-,ij}S_{+,ji}+S_{+,ij}S_{-,ji})}{2}\cdot\right.\right. \\
& \cdot\left[\frac{1}{4}J^F(\omega_I-\omega_{ij},\tau_D,\tau_N)+\frac{3}{2}J^F(\omega_{ij},\tau_D,\tau_N)+\frac{3}{2}J^F(\omega_I+\omega_{ij},\tau_D,\tau_N)\right]+ \\
& \left.+3|S_{z,ij}|^2\left[2J^F(\omega_{ij},\tau_D,\tau_N)+\frac{3}{4}(J^F(\omega_I-\omega_{ij},\tau_D,\tau_N)+J^F(\omega_I+\omega_{ij},\tau_D,\tau_N))\right]\right\}+ \\
& \left.-2\langle S_z\rangle^2\{[J^F(0,\tau_D,\tau_N)+\frac{3}{4}J^F(\omega_I,\tau_D,\tau_N)]-[J^A(0)+\frac{3}{4}J^A(\sqrt{2\omega_I\tau_D})]\}\right\rangle
\end{aligned} \tag{3.9}$$

Evidently equations 3.8 and 3.9 are not suitable for an efficient simulation of relaxivity curves and data analysis because computation times would be prohibitively long on standard instrumentations. Instead, the authors proposed

an alternative heuristic fitting which reproduces the gradual vanishing of the low-field dispersion through a linear combination of the limit rates when $E_A \to \infty$ and $E_A = 0$:

$$\frac{1}{T_1} = \frac{32\pi}{135000}{\mu^*_{SP}}^2\gamma_I^2\left(\frac{N_A C}{RD}\right)\left\{7P\frac{L(x)}{x}J^F\left[\Omega(\omega_S,\omega_0),\tau_D,\tau_N\right] + \right. \tag{3.10}$$
$$\left. + \left[7Q\frac{L(x)}{x} + 3(P+Q)\left(1 - L^2(x) - 2\frac{L(x)}{x}\right)\right]J^F(\omega_I,\tau_D,\tau_N) + 3L^2(x)J^A(\sqrt{2\omega_I\tau_D})\right\}$$

$$\frac{1}{T_2} = \frac{32\pi}{135000}{\mu^*_{SP}}^2\gamma_I^2\left(\frac{N_A C}{RD}\right)\left\{13P\frac{L(x)}{x}J^F\left[\Omega(\omega_S,\omega_0),\tau_D,\tau_N\right] + 6Q\frac{L(x)}{x}J^F(0,\tau_D,\tau_N) + \right.$$
$$\left. + \left[1 - L^2(x) - 2\frac{L(x)}{x}\right]\left[3J^F(\omega_I,\tau_D,\tau_N) + 4J^F(0,\tau_D,\tau_N)\right] + L^2(x)[3J^A(\sqrt{2\omega_I\tau_D}) + 4J^A(0)]\right\} \tag{3.11}$$

where $\mu^*_{SP} = A\mu_{SP}$ is the magnetic moment of each ferrite crystal renormalized by a constant A, which has been introduced to readjust the global SPM moment (*i.e.* the SPM magnetization) with the one sensed by the probing nuclei at a local level; γ_I is the proton gyromagnetic ratio, r is the distance of minimum approach 'proton-magnetic ion', D is the self diffusion coefficient of the medium, N_a is Avogadro's number and C is the molar concentration of nanoparticles; $L(x)$ is Langevin's function, where $x = \mu^*_{SP}B_0/k_BT$.

Parameter τ_D is defined as $\tau_D = r^2/D$, while $\tau_{N,NMR}$ is the Néel relaxation time at room temperature; the label 'NMR' is added to distinguish this parameter from the analogous quantity yielded by the AC data analysis; ω_S and ω_I are the electron and proton transition frequencies, respectively; ω_0 is a free parameter included in the function Ω to recover the correct behaviour of the low-field dispersion inflection point and assuring that it may never appear at a frequency lower than ω_0.

The application of the heuristic formula 3.11 to the fitting of longitudinal relaxivity curves in a certain number of colloidal solutions of diverse magnetic nanoparticles allowed a comparison between the reversal time of magnetization as seen by NMR and the results from AC susceptibility experiments and provided new hints about the physical mechanisms of relaxation. We were thus able to validate Roch's model on a wide selection of samples, and track the effect of the crystal's internal anisotropy energy with the magnetic core-size of the particles. Since P and Q in Eq. 3.11 ultimately weight the contributions from the Zeeman energy and the magnetic anisotropy energy[32], we expect the ratio P/Q to decrease with the particle size. We also successfully extracted the relative weights of Néel and Curie contributions to the ^{1}H nuclear magnetization relaxation and studied their dependence on magnetic core diameter and ion species, as it is shown in the following sections.

3.7 r_1 longitudinal relaxivity data analysis

Each r_1 relaxivity curve was quantitatively analyzed by building a numerical integration routine implementing Roch's model, i.e. Eq. 3.11. We assumed that

the solvent self-diffusion coefficient D was the same for water and toluene, $\sim 2 - 3 \times 10^{-5}$ cm^{2}s^{-1}; this range was chosen to account for the diffusion coefficient variability due to the presence of superparamagnetic agents in the medium. We let parameters A, P, Q, r and $\tau_{N,NMR}$ vary so that an estimation of the distance of minimum approach r and of the characteristic Néel relaxation time $\tau_{N,NMR}$ could be obtained as well.

We plotted the fit to eq. 3.11 of the experimental data collected on S-Mag/W, P-Mag/T, P-Mag/W, MnFe/T and CoFe/T samples in figures 3.5, 3.7, 3.9, 3.11, 3.13 and 3.14, respectively; Table 3.3 lists the output values for the main free parameters of Eq. 3.11 as obtained from the fitting procedure.

3.7.1 The role of size and magnetic anisotropy

We should now discuss the meaning of the results in Table 3.3. The first observation regards the estimated distance of closest approach, r, which is not necessarily equal to the particle's radius. The good agreement between parameter $2r$ and d_{TEM}, that is the particle diameter as measured by TEM, suggests that the solvent molecules do penetrate the enclosing organic shells of the particles. The difference is mostly due to the diffusional motion of the solvent molecules: water (or toluene) molecules may diffuse only within a certain distance from the magnetic core since the organic coating partly blocks the Brownian paths toward the core.

The strongest agreement between the two parameters was observed in the magnetite series, featuring a difference of only 2–4 nm between $2r$ and d_{TEM}, with some exceptions; for instance Sample S-Mag/W-2 has ($d_{TEM} = 6.7$ nm, $2r = 12.8$ nm) and P-Mag/W-2 has ($d_{TEM} = 8.0$ nm, $2r = 17.1$ nm). Although we do not know the thickness of the sugar layer in series S-Mag/W, we can confirm the result of Ref. [128], i.e. the coating layer is easily penetrated by the solvent molecules, in most cases. It also appears that there is a noticeable difference in the solvent penetration depth when comparing the polymer capped magnetite and the sugar capped magnetite samples in water solutions: clearly, the water molecules more easily penetrate the sugar coating than the thick hydrophilic polymer coating plus the underlying hydrophobic shell. Also, when the magnetite samples from the P-Mag series are dispersed in a toluene solution the minimum approach distance decreases: this result is easily ascribed to the thinner organic layer, because the amphiphilic polymer surfactant is missing.

Results on CoFe are perhaps the most difficult to comment. Although the presented best-fit curve approximate the experimental data reasonably well, Roch's model does not easily adapt to very 'squashed' relaxivity curves, such as those in figures 3.13 and 3.14, hence the strong disagreement between $2r$ and d_{TEM}, especially on the larger samples, e.g. sample CoFe-T/1 has ($d_{TEM} = 8.6$ nm, $2r = 16.1$ nm) .

In the next paragraphs we refer to the particle size as the magnetic core size measured by TEM, d_{TEM}.

A quick glance at the P and Q columns of table 3.3 reveals that P and Q

Sample	d_{TEM} nm	$2r$ nm	A	P	Q	$\tau_{N,NMR}$ s/rad	P/Q
S-Mag/W-1	4.1 ± 0.6	4.9 ± 0.3	1.09 ± 0.08	0.22 ± 0.05	0.49 ± 0.09	$9.73 \pm 5.51 \times 10^{-10}$	0.45 ± 0.19
S-Mag/W-2	6.7 ± 0.8	12.8 ± 0.5	0.53 ± 0.03	0.00 ± 0.08	0.82 ± 0.05	$2.82 \pm 1.66 \times 10^{-9}$	0.00
S-Mag/W-3	18.2 ± 1.1	15.2 ± 1.0	0.53 ± 0.01	0.06 ± 0.01	0.94 ± 0.12	$9.58 \pm 2.80 \times 10^{-8}$	0.06 ± 0.02
P-Mag/W-1	5.5 ± 0.6	10.1 ± 0.4	0.65 ± 0.03	0.32 ± 0.15	0.68 ± 0.11	$2.71 \pm 2.94 \times 10^{-9}$	0.46 ± 0.29
P-Mag/W-2	8.0 ± 0.8	17.1 ± 0.3	0.36 ± 0.01	0.00 ± 0.10	0.92 ± 0.22	$2.17 \pm 1.81 \times 10^{-9}$	0.00 ± 0.11
P-Mag/W-3	12.0 ± 0.7	14.5 ± 0.2	0.62 ± 0.01	0.05 ± 0.08	0.77 ± 0.13	$3.36 \pm 1.36 \times 10^{-9}$	0.06 ± 0.11
P-Mag/T-1	5.5 ± 0.6	7.0 ± 0.4	1.03 ± 0.06	0.14 ± 0.09	0.44 ± 0.08	$1.39 \pm 1.12 \times 10^{-9}$	0.32 ± 0.26
P-Mag/T-2	8.0 ± 0.8	11.2 ± 0.4	0.61 ± 0.03	0.05 ± 0.04	0.81 ± 0.10	$3.30 \pm 1.68 \times 10^{-9}$	0.06 ± 0.06
P-Mag/T-3	12.0 ± 0.7	12.3 ± 0.4	0.75 ± 0.03	0.00 ± 0.02	1.00 ± 0.15	$2.02 \pm 2.07 \times 10^{-9}$	0.00
MnFe/T-1	3.0 ± 0.2	6.8 ± 0.1	0.52 ± 0.01	0.49 ± 0.05	0.46 ± 0.09	$3.33 \pm 1.01 \times 10^{-10}$	1.06 ± 0.31
MnFe/T-2	4.8 ± 0.1	7.7 ± 0.1	0.49 ± 0.01	0.26 ± 0.02	0.52 ± 0.09	$7.13 \pm 3.81 \times 10^{-10}$	0.49 ± 0.12
MnFe/T-3	6.0 ± 0.2	9.3 ± 0.1	0.38 ± 0.01	0.20 ± 0.04	0.25 ± 0.04	$1.63 \pm 3.03 \times 10^{-10}$	0.80 ± 0.30
CoFe/T-1	8.6 ± 1.1	16.1 ± 0.4	0.80 ± 0.01	0.07 ± 0.06	0.93 ± 0.26	$2.89 \pm 2.33 \times 10^{-7}$	0.08 ± 0.09
CoFe/T-2	8.6 ± 1.1	14.9 ± 0.3	0.93 ± 0.01	0.04 ± 0.07	0.58 ± 0.07	$5.21 \pm 3.38 \times 10^{-6}$	0.06 ± 0.13
CoFe/T-3	6.0 ± 1.4	7.6 ± 0.4	0.85 ± 0.06	0.04 ± 0.07	0.87 ± 0.18	$6.24 \pm 2.54 \times 10^{-9}$	0.05 ± 0.09
CoFe/T-4	5.0 ± 1.2	8.7 ± 0.3	1.12 ± 0.03	0.05 ± 0.14	1.00 ± 0.17	$2.05 \pm 1.85 \times 10^{-9}$	0.05 ± 0.15

Table 3.3 – Fit values from the analysis of ^{1}H-NMR-D profiles employing Roch's model. From left to right: magnetic core diameter measured by TEM, $2r$ parameter extracted fitting the NMRD data to Eq. 4.3, magnetic moment renormalization factor A, P and Q values, Néel's relaxation time seen by the NMR-D measurement, P/Q ratios.

have opposite trends as a function of d_{TEM}. As explained in Ref. [32], P and Q weight the contributions of Zeeman energy and magnetic anisotropy energy to the relaxivity value, respectively. Since P and Q does not always sum up to 1, rather their sum should be lower than or equal to 1, it is much more useful to look at the P/Q ratio rather than the absolute P and Q values. Then, we would usually expect a decreasing P/Q ratio, as the particle size increases and the contribution from the magnetic anisotropy (thus Q) becomes more and more important. We reported the P/Q ratios for all samples in Fig. 3.18.

As expected, the decreasing trend of P/Q as a function of size is common to all studied samples. A marked increase when lowering the nominal core diameter below the 5nm line is easily noticed. This increase is the most pronounced in the MnFe/T and S-Mag/W series and corresponds to a very marked damping of the low-field dispersion of the smaller samples with respect to the larger ones. The most dramatic effect due to the increasing anisotropy energy was observed in series S-Mag/W for which the NMR-D profile of the 18 nm sample loses the high-field peak. The P/Q ratio for this sample is almost zero while the one for sample S-Mag/W-1 is 0.45. The same behavior is observed in Samples P-Mag/T-1 ($P/Q = 0.32$) and P-Mag/T-3 ($P/Q = 0$), and in Samples P-Mag/W-1 ($P/Q = 0.46$) and P-Mag/W-3 ($P/Q = 0.06$). Indeed, series P-Mag/T and S-Mag/W seems to behave very similarly, as far as we can deduce from the P/Q values, because the minimum approach distance of solvent molecule in the two series is comparable, as previously noticed.

An interesting remark can be made about the comparison of the two P-Mag series: the P/Q values in Fig. 3.18 for samples P-Mag/W are shifted upwards with respect to the P-Mag/T series, leading to conclude that the transfer from the toluene solution to water had the effect of increasing the contribution from

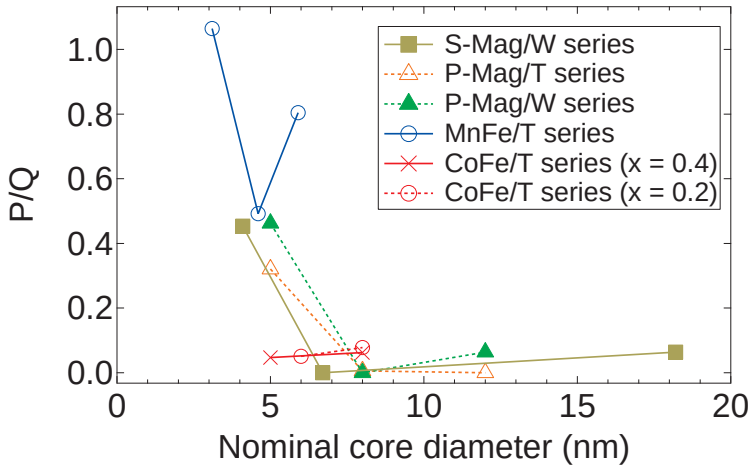

Figure 3.18 – P/Q ratios for all investigated samples: a low P/Q ratio is associated with a pronounced magnetic anisotropy energy. Conversely, smaller particles are characterized by a low magnetic anisotropy and a consequently higher P/Q ratio. The P/Q ratio is lowered by either increasing the particle diameter within a given series or changing the magnetic material, at fixed particle size; compare, for instance, the values of P/Q around $d = 5$ nm.

the Curie relaxation mechanism. Again, one could ascribe this phenomenon to the lower distance of minimum approach of the solvent molecules in the P-Mag/T series with respect to the P-Mag/W samples (see the column for d_{NMR} and d_{TEM} in table 3.3).

Results on the MnFe/W series appear to be less decisive for our study of the dependence of relaxivities on size and magnetic anisotropy, because all samples in this series feature a clear low-frequency dispersion and, consequently, the associated P/Q ratios are high and very scattered.

The case of Cobalt Ferrite is peculiar, because the increase in P/Q for the smaller particles is barely noticeable. As a matter of fact P/Q is limited to the range $[0.04, 0.08]$ for all CoFe samples. The great enhancement in the effective anisotropy due to the Cobalt substitution is responsible for such a small difference between small and large particles; if we look at these results as a function of the Cobalt over Iron content in the magnetic material, no appreciable difference could be observed in the smaller particles when lowering the cobalt content from 15% ($x = 0.4$, in CoFe/T-1 and CoFe/T-3) to 7% ($x = 0.2$, in CoFe/T-2 and CoFe/T-4). A similar behaviour was also reported by Roch *et al.* in Ref. [121]. This result was expected since the CoFe/T NMR-D profiles, displayed in figure 4.13, do not show any significant enhancement of the low field dispersion when halving the cobalt content.

A note about factor A is due: A renormalizes the superparamagnetic moment μ_{SP}, which in turn is calculated from the experimental value of M_S as $\mu_{SP} = M_S * V * \rho$, where V is the nanoparticle spherical volume and ρ is the density of the inorganic material. This operation has the main function of recovering the correct scale for the simulated relaxivity curve and has little effect on the extracted values of P, Q and r. The values of A reported in table 3.3 are mostly lower than the unity, which is ascribed to a number of factors, such as errors in the estimate of M_S, in the concentration C appearing in equation 4.3, and in the fraction of organic material. These issues affect each sample in different ways and produce variations in the value of A inside each series. Besides, some difference between the real SPM moment and the calculated one is expected, since the calculation of μ_{SP} assumes a perfectly monodispersed ensemble of spherical magnetic particles, whereas in fact a dispersion of particle size and shape is always present.

The good quality of the NMR-D results from Roch's model was also confirmed by a comparison between the estimation of the Néel relaxation times at room temperature as extracted by NMR-D profiles and AC susceptibility analysis.

In Fig. 3.19 we plotted the ratios $\tau_{N,NMR}/\tau_{N,Arr}$ and $\tau_{N,NMR}/\tau_{N,VF}$ for a selection of samples. The plot is log-linear and the gray horizontal band indicate the region including all points that differ no more than one order of magnitude from 1, ie. the region $[0.1, 10]$. When parameters such as $\tau_{N,Arr}$ are estimated by different techniques generally a difference of 1 or 2 orders of magnitude is still accepted as good agreement; then the inclusion region was chosen to sort out all points that are in evident discordance with each others. As it can be

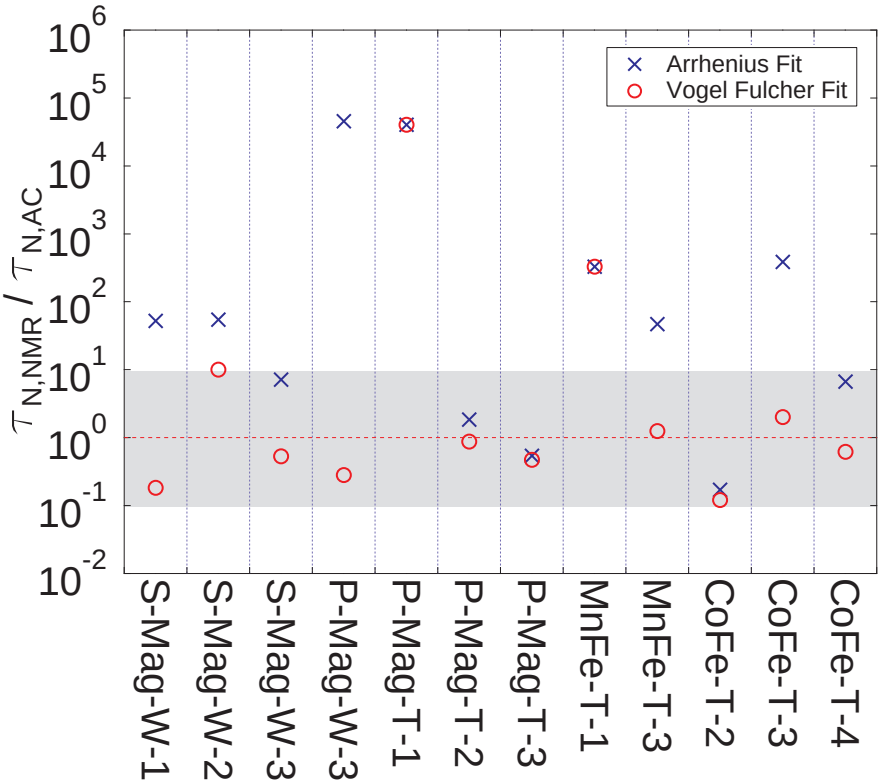

Figure 3.19 – $\tau_{N,NMR}/\tau_{N,Arr}$ and $\tau_{N,NMR}/\tau_{N,VF}$ ratios for all investigated samples. The grey band in the graph covers the ratio range between 0.1 and 10, i.e. within one order of magnitude from the pivot value 1, indicated with a red dashed line. Points falling in this range identify a good agreement between AC susceptibility and NMR spectroscopy in evaluating Néel's relaxation time at room temperature.

noticed from the number of points falling within one order of magnitude from 1, there is a much nicer agreement between the NMR results and the AC results analysed with the VF law than those extracted with the Arrhenius expression; in the former case 10 out of 12 points fall into the gray region, while in the latter only 5 out of 12 points lie in the selection range.

3.8 r_2 transversal relaxivity data analysis

Analysis of r_2 data took a different route and did not rely on equation Roch's heuristic equation 3.11. The analysis of r_2 with Roch's model is quite more difficult than r_1, and pertains to future works. Instead, a very simple model from the literature allows to classify the investigated materials on the basis of a universal scaling law (Vuong *et al.*, [139]).

The authors of [139] argue that "despite the broad variety of superparamagnetic MRI contrast agents differing by their size, geometry (filled micelles or hollow vesicles, dense or loose clusters, etc.), type of coating (organic or inorganic, impermeable or porous, hydrophilic or hydrophobic, etc.), no specific model need to be introduced [$\cdots$]: the simple Outer Sphere model can correctly

Sample	M_v	d	$\Delta\omega\tau_D$	r_2	r_2/M_v^2
	A m^{-1}	nm	–	s^{-1} mM^{-1}	s^{-1} mM^{-1} A^{-2} m^2
S-Mag/W-1	402710	4.1	0.063	85.62	5.28×10^{-10}
S-Mag/W-2	392250	6.7	0.164	234	1.52×10^{-9}
S-Mag/W-3	355640	18.2	1.100	281.09	2.22×10^{-9}
P-Mag/W-1	198740	5.5	0.056	52.8	1.34×10^{-9}
P-Mag/W-2	271960	8	0.162	101.96	1.38×10^{-9}
P-Mag/W-3	224890	12	0.302	18.564	3.67×10^{-10}
MnFe/T-1	230120	3	0.019	7.8	1.47×10^{-10}
MnFe/T-2	230120	4.8	0.049	22.73	4.29×10^{-10}
MnFe/T-3	219660	6	0.074	87.576	1.81×10^{-9}
CoFe/T-1	418400	8.6	0.289	488	2.79×10^{-9}
CoFe/T-2	418400	8.6	0.289	340.28	1.94×10^{-9}
CoFe/T-3	376560	6	0.127	59.268	4.18×10^{-10}
CoFe/T-4	292880	5	0.068	74.062	8.63×10^{-10}

Table 3.4 – Parameters for the analysis of transverse relaxivity data. Columns from left to right: sample name, core size, volume magnetization, $\Delta\omega\tau_D$ values, r_2 relaxivity and r_2/M_v^2 ratios. r_2/M_v^2 ratios versus d are also plotted in Fig. 3.20b.

represent the experimental data once structural and magnetic parameters are known (external diameter, volume fraction and magnetization of the magnetic materials) and the relaxivity is appropriately normalized".

Restraining the following discussion to those samples that are in the motional averaging regime (MAR) and in the framework of the OS model, the expression for r_2 found by Vuong and co-authors is:

$$r_2 = \frac{4\gamma^2\mu_0^2\nu_{mat}M_v^2d^2}{405D} \tag{3.12}$$

where γ is the proton gyromagnetic ratio, μ_0 is the magnetic permeability of vacuum, M_v is the total volume magnetization of the sample, d is the average diameter of the particles, D is the water translational diffusion constant and ν_{mat} is the molar volume, a material-dependent parameter that is given bt the ratio of the molar mass divided by the number of magnetic ions in the chemical formula and by the mass density. In SI units, for maghemite holds $\nu_{mat} = 1.57 \times 10^{-5}$ m$^3\cdot$mol^{-1} and for magnetite $\nu_{mat} = 1.5 \times 10^{-5}$ m$^3\cdot$mol^{-1}.

The condition of validity of the motional averaging regime is $\Delta\omega\tau_D < 1$ where $\Delta\omega$ is the shift in the Larmor frequency at the particle surface. This condition is usually satisfied for the case of small single nanoparticles made of pure magnetic materials, within a thin fully hydrated shell [140, 128]. It is also proven that the nature of the magnetic ion in the iron spinel structure, eg. Fe^{2+}, Co^{2+}, Ni^{2+}, Mn^{2+}, Zn^{2+}, $\cdots$, only leads to a $\pm 5\%$ difference on ν_{mat}.

Substituting all the numerical values in Eq. 3.12:

$$r_2 = 5.9 \times 10^{-12} d^2 M_v^2 \tag{3.13}$$

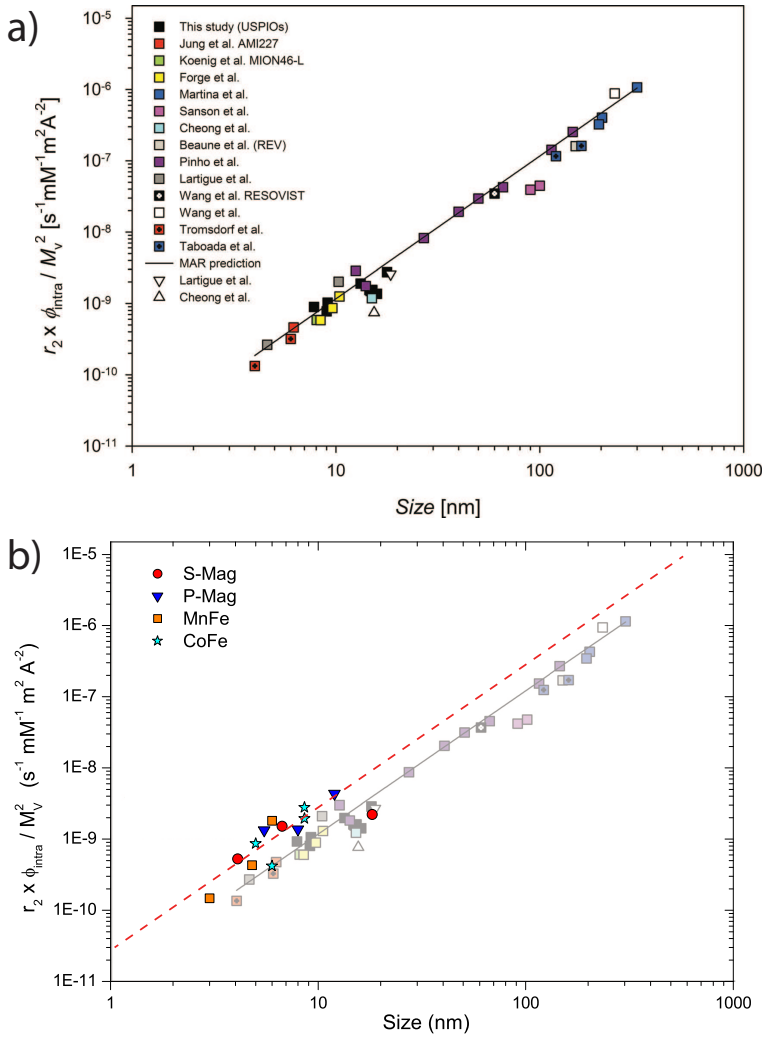

Figure 3.20 – a) Plot of r_2/M_v^2 ratios vs nominal core size d as shown on [139]. The solid black line corresponds to Eq. 3.13. b) (d, r_2/M_v^2) points relative to the samples series presented in this chapter, overlayed to the data of plot (a).

To test the so obtained scaling law, the ratio r_2/M_v^2 was calculated by the authors for various types of ferrite nanoparticles and clusters in the MAR, some novel samples, some taken from the recent literature. A log-log plot of the ratio r_2/M_v^2 as a function of size d is reproduced in Fig. 3.20a, while the points for samples presented in this thesis are collected in Fig. 3.20a, which shows the points overlayed to the results of [139]. In both figures the solid black line is Eq. 3.13. The ratio values for clustered samples were multiplied by the intra-aggregate volume fraction ϕ_{intra}, which allows to properly compare the relaxation data $r_2 \times \phi_{intra}/M_v^2$ as if the particles in the cluster were filling the same volume fraction of suspension as single superparamagnetic nanoparticles at 1 mM iron concentration. Since all the samples presented in this thesis are single particle systems, there was no need for such renormalization of the measured r_2 values.

Parameters for the analysis of r_2 are collected in table 3.4 and r_2/M_v^2 ratios for [139] and for the here investigated series are shown in Fig. 3.20. Our data seems to pack around a straight trend line that runs parallel and close to Eq. 3.13. The overall behavior of r_2/M_v^2 is in line with the conclusions of Vuong: eq. 3.13 could be exploited as "a unified method to predict the transverse relaxivity r_2 of MRI contrast agents at clinical field based on materials (M_v) and geometrical (d, ϕ_{intra}) parameters".

3.9 Conclusions

In conclusion, Chapter 3 provided a systematic validation of the excellent quality of the fitting results employing Roch's theory for the nuclear relaxation in SPM systems. It should be stressed that the importance of this experimental work resides in the possibility of tracking the effect of the crystal's internal anisotropy energy, dampening the low-field dispersion, with the magnetic core-size of the particles.

The relative weights of Néel and Curie contributions to the ^{1}H nuclear magnetization relaxation have been successfully extracted and their dependence on magnetic core diameter and ion species has been evaluated: a marked decrease of the P/Q ratio as the magnetic anisotropy energy per particle increases has been observed in all sample series; this behavior is ascribed to both an increased core diameter and increased magnetic anisotropy energy density.

The core diameters and Néel's relaxation times were also calculated through the fit of NMR-D data and compared with TEM and AC susceptibility results. Due to solvent molecules penetrating only to a certain extent into the organic coating of the particles, $d_{NMR}/2$ actually measures the distance of minimum approach to the center of the particle and thus d_{NMR} was found to be generally greater than d_{TEM}. Néel relaxation times, as measured by NMR, lie in the superparamagnetic range, as it would be expected; a phenomenological Vogel-Fulcher law had to be applied to the AC susceptibility data in order to find a satisfactory agreement between NMR and AC data, since Néel's model breaks down in concentrated solutions and powders due to sizable dipolar interparticle interactions.

Chapter 1, 2 and 3 have provided a broad and detailed overview of the magnetic properties and spin dynamics of ferrite magnetic particle; all the provided information is functional to the selection of a suitable material for biomedical applications. In particular, it is possible to address a particular sample series having the most favorable combination of τ_0, E_B and M_S, so that a strong contrasting effect can be reached without interference from other competing dynamics.

The next concluding chapter presents the preliminary in-vivo study of one MRI contrast agent composed of magnetite nanoparticles coated with a block polymer. The reason behind the choice of this combination of materials is portrayed in Fig. 3.21, which reports the values of the transverse relaxivity

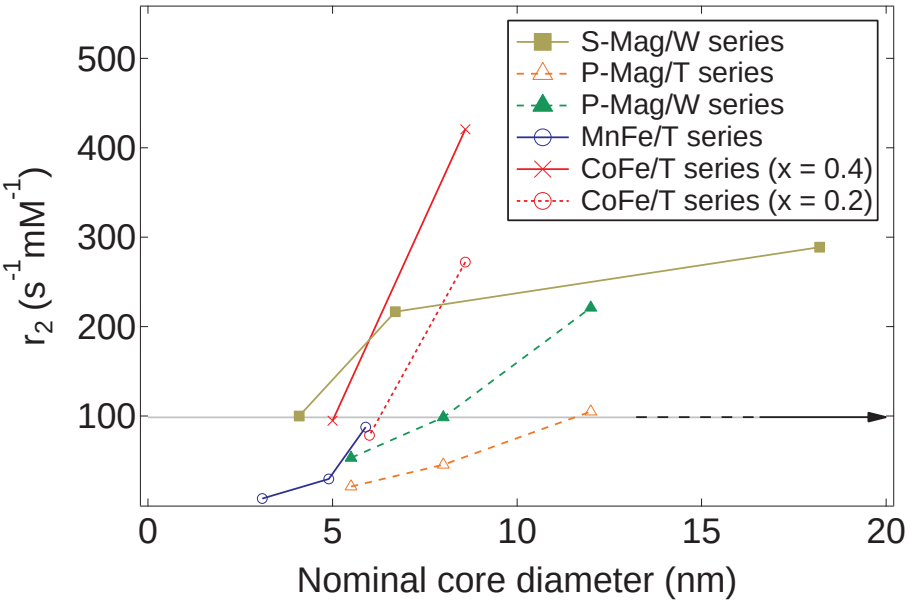

Figure 3.21 – r_2 transverse proton relaxivities at excitation frequency $\nu_{NMR} = 60$ MHz, corresponding to a field $H = 14$ kOe, plotted against the nominal particle diameter. 60 MHz is a very common frequency used for magnetic resonance imaging; here it is chosen as the reference to show how the various materials would perform during a negative contrasted MRI experiment. The higher the r_2 value, the higher the contrast in the final image. The rightward pointing arrow at the $r_2 = 98.6$ $s^{-1}mM^{-1}$ level is the Endorem reference. The d value for Endorem is not shown because this agent is composed of very dispersed particles with diameters ranging from 50 nm to 180 nm.

r_2 as a function of the nominal core diameter for the investigated solutions of nanoparticles, at the excitation frequency $\nu_{NMR} = 60$ Mhz. All samples exhibit an excellent contrasting power with respect to the Endorem reference, indicated by the black arrow in Fig. 3.21. Since a high r_2 value is required for MRI applications the ideal candidates would be either of these three aqueous solution series: S-Mag, P-Mag and CoFe; each of this series contains one sample with $r_2 \sim 300$ $s^{-1}mM^{-1}$. The P-Mag sample with $d \sim 12$ nm, however, looks the most promising because Iron Oxide biocompatibility is much higher than that of Cobalt Ferrites, and the particle size needed to reach such relaxivity value is much lower than the S-Mag series.

Chapter 4

Preliminary in-vivo tests with novel multi-functional magnetic nanoparticles

4.1 Introduction

The last brief chapter of this thesis is dedicated to first preliminary in-vivo experimentation of a functionalized iron-oxide based contrast agent with targeting capabilities. The chosen material belongs to the same class of the previously studied magnetite samples (cfr. P-Mag series in the previous Chapter), exhibiting both excellent contrasting properties and high biocompatibility. First, the experimental protocol is described, then MRI images recorded on treated and untreated mice are discussed. Sufficient targeting specificity has been observed, although an optimal homogenous distribution of the agent over the whole tumoral volume is a long term aim, still out of reach.

4.2 State of the art in brief

With the advances in the field of personalized medicine in today's oncology practices, the applications of biomarker-targeted imaging and drug delivery systems are being explored at a fast rate. As a matter of fact, Iron Oxide based nanoparticles are highly sensitive imaging probes and effective carriers of therapeutic agents: increasing evidence indicates that the selective delivery of nanoparticle agents into a tumor mass can minimize toxicity for normal tissues and maximize cancer cells killing effects of cytotoxic agents. Furthermore, nanoparticles can accumulate to very high concentrations in certain solid tumors because of the enhanced permeability and retention effect (EPR). However, the EPR facilitates tumor targeting only to some level, while an active approach to targeting may further increase the local concentration of drug or change the intracellular biodistribution within the tumor via receptor-mediated internalization.

Therapeutic entities, such as small molecular drugs, peptides, proteins and

nucleic acids, can be incorporated in iron oxide nanoparticles through either loading on the surface layer or trapping within the nanoparticles themselves. When delivered to the target site, the loaded drugs are usually released by diffusion, vehicle rupture or dissolution, or by endocytosis; the therapeutic conjugations of tumor-targeting agents and anti-tumoral drugs on iron oxide nanoparticles enable the simultaneous estimation of tissue drug levels and monitoring of therapeutic response [141, 142].

Only monocrystalline particles or minimal aggregated particles in dispersion would both display superparamagnetism and form a stable suspension when coated with a suitable surfactant. On the other hand particles larger than 400 nm (i.e. the minimal diameter of the capillaries), will be filtered out [143]. It has also been reported that particles which exceed than 200 nm are eliminated immediately regardless of being polymer coated or not[144]. Even the particles under 100 nm would be mostly captured by the liver. Indeed, the phagocytotic activity is size dependent: the smaller the particles, the longer their circulation time in blood vessel. The bio-compatible coating also plays a role; for instance, PEG-coated particles tend to be more transparent to macrophages action [145, 146] and so their circulation time increases substantially.

4.3 Experimental setup

Given the high biological compatibility, low toxicity, together with an excellent MRI contrasting power, both magnetite and maghemite nanoparticles with magnetic core in the size range $10 < d < 20$ nm seem to yield the optimal products, also in the light of the encouraging results of Chapter 3. Here we refer mainly to transverse r_2 relaxivity, the efficiency index for negative SP agents. The r_2 values are independent from the coating material, so the actual nature of the surfacting agent is of little importance for MRI contrast efficiency, but must be taken into account for its possible toxicity level. Among different investigated series of magnetite/maghemite coated samples, with the aim of obtaining a multifunctional particle including MRI contrast efficiency, possibly a fluorescent molecule, a drug (for drug delivery) and a targeting entity, we selected the sample called '15_Block-M-PTX-FA'. The selected sample consists of a water suspension of Hybrid Block-M magnetite nanoparticles with core diameter of about 12 nm and average hydrodynamic diameter $d_{hyd} = 130 \pm 30$ nm. The size value of 12 nm is really a limit value to balance the advantage of a high r_2 relaxivity with the disadvantage given by the fact that for $d_{hyd} > 12$ nm the particles easily precipitate in aqueous solutions. This sample is currently part of the in-vivo trial test series within the scope of the european project 'Nanother' (EU-FP7). The system full name is '15_Block-M-PTX-FA (115/15) / IS19b' (from here on only '15_Block-M-PTX-FA') and was synthesized by Colorobbia in collaboration with the INSTM consortium (University of Pisa is acknowledged for synthesis, and University of Firenze is acknowledged for measurements of magnetic properties).

Two types of samples were considered: a first variant is naked and was used for negative control, while the second type contains the drug Paclitaxel and is grafted with folic acid. Low molecular weight targeting agents such as folic acid have been demonstrated to preferentially target cancer cells, because the folate receptor is frequently overexpressed on the surface of cancer cells [147]. The folate receptor is not only a tumor marker, but also has been shown to efficiently internalize molecules coupled to folate [148, 149]. Furthermore, folic acid itself is stable, and generally poorly immunogenic.

Paclitaxel (PTX) has been embedded into the folate shell, to test both targeting and therapeutic efficiencies. Paclitaxel is a microtubule-targeted agent widely used in cancer therapy. Its primary cellular effect is to cause abnormal stabilization of the dynamic microtubule polymerization, leading to the failure of mitosis. In addition, paclitaxel also alters other cellular functions that involve microtubules, such as intracellular signaling and organelle transport and locomotion[150].

In the following section the preliminary results of the ongoing in-vivo trials with 15_Block-M-PTX-FA are briefly presented. In-vivo experimentation was not directly carried out by the author of this thesis, although assistance in the selection and characterization of solid state samples was provided. This very short chapter is only intended as a demonstration of the capabilities of a functionalized iron-oxide contrast agent belonging to the same class as the nanoparticle samples presented in this work.

4.4 Relaxometric measurements on 15_Block-M-PTX-FA

Relaxivities were recorded using the same setup as the measurements of Chapter 3. The r_1 and r_2 relaxivity profiles are shown in Fig. 4.1 against Endorem: the first striking feature is the very high difference in the r_2 levels between Endorem and Sample 15_Block-M-PTX-FA while the frequency dependence of r_1 is typical of a very high magnetically anisotropic system and shares some resemblance to the CoFe relaxivity curves of the previous chapter. Further grafting with Paclitaxel does not compromise the excellent performance of this sample, as can be noticed from Fig. 4.1.

4.5 Experimental procedures

Preliminary runs of in vivo experiments for the determination of the minimal dose for contrast in MRI images and therapeutic effect as magnetic fluid hyperthermia (MFH) mediators of the selected material were carried out in Verona. The chosen tumoral cell line is *MDA-MB-231* human breast cancer.

Ten female homozygote nude mice were implanted with the tumoral cells via subcutaneous implantation. The animals were scheduled for testing with

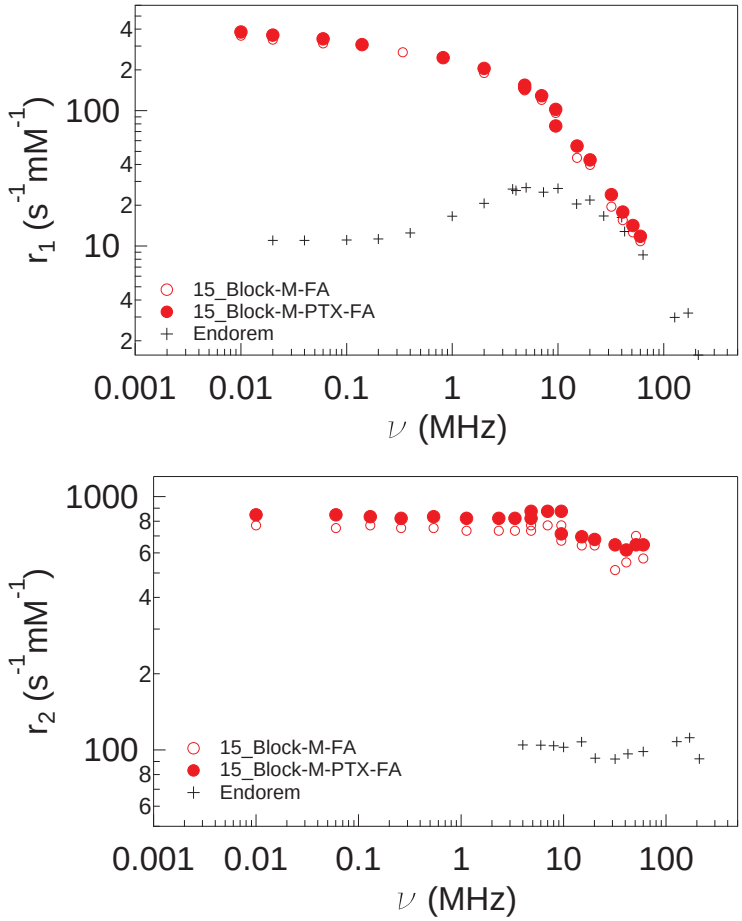

Figure 4.1 – A comparison between $r1$ (top) and r_2 (bottom) relaxivities of 15_Block-M-PTX-FA, 15_Block-M-PTX and Endorem. 15_Block-M-PTX-FA exhibits a much higher r_2 relaxivity than Endorem, while r_1 values at the frequencies of interest (i.e. $\nu >\sim 10$ Mhz) are comparable. These properties confer excellent negative contrasting power to sample 15_Block-M-PTX-FA.

nanoparticles with and without folic acid and with Endorem, to compare the MRI contrasting efficiency and cancer targeting capabilities in vivo. Also, MFH cancer treatment was attempted on five of the animals. The experimental schedule was as follows:

- 2 animals were treated with the intratumoral injection of NPS without folic acid for the hyperthermia treatment.
- 3 animals with intratumoral injection of NPS with folic acid for the hyperthermia treatment.
- 2 animals with slow infusion of NPs with folic acid to see targeting at 1 hour, 24 hours and 48 hours.
- 2 animals with slow infusion of Endorem to see targeting at 1 hour, 24 hours and 48 hours.

- 1 animal with slow infusion of NPs without folic acid to see targeting (negative control) at 1 hour, 24 hours and 48 hours.

For targeting experiments animals were injected with NPS via endovenous system (tail of the mouse). The experimental protocol for in vivo experiments was implemented according to: R. Meier *et. al*, *Breast cancers: MR imaging of folate-receptor expression with the folate-specific nanoparticle P1133* (Ref. [151]).

Average T_2 values were obtained in MRI slices drawing a region of interest in the liver and in the tumor and measuring the T_2 relaxation time. T_2-weighted images were acquired with the following parameters: echo time = 56 ms, repetition time = 5000 ms, slice thickness = 2 mm, field of view = 5.0×2.5 cm^2, resolution: 256×128.

The sagittal MRI images displayed in Fig. 4.2 show that, in comparison to Endorem, 15_Block-M-PTX-FA yields a better targeting (see arrows that indicate where CA is delivered), as it would be expected, since no specific targeting mechanism is implemented for Endorem: dark areas are visible in the

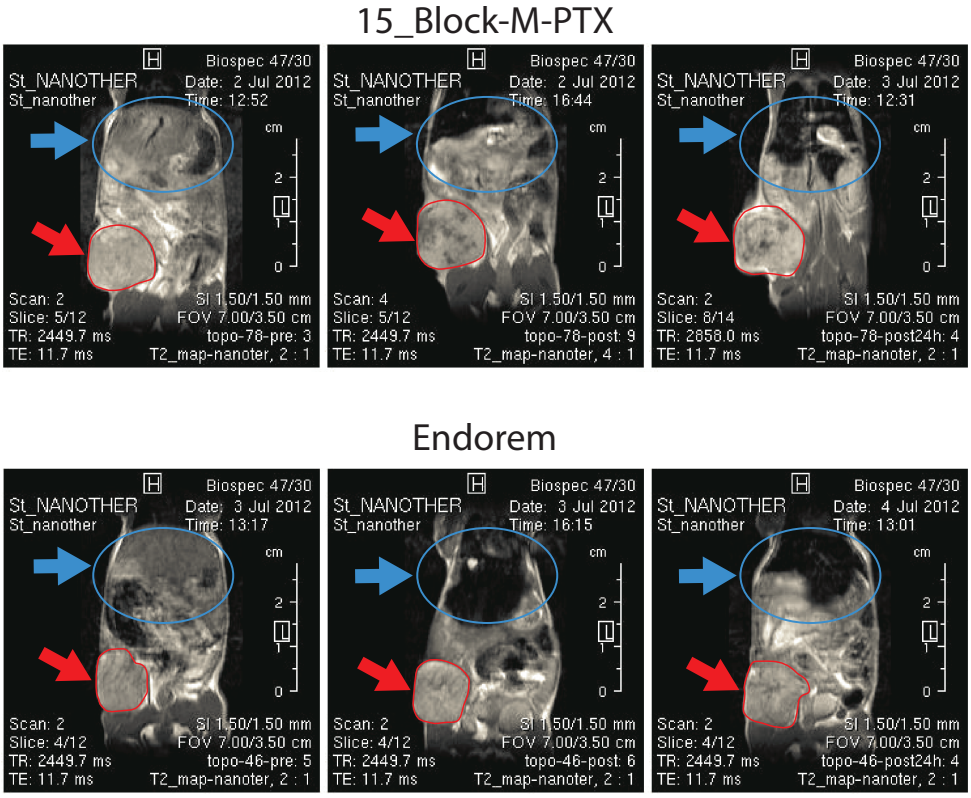

Figure 4.2 – Sagittal MRI sections of animals treated with **15_Block-M-PTX-FA** (top row) and **Endorem** (bottom row) before injection, after 1h and after 3h. The liver is highlighted with a blue outline and a blue arrow, while the tumoral mass is circled in red and indicated by a red arrow. Dark areas are visible in the tumoral mass when 15_Block-M-PTX-FA is used while, in comparison, Endorem shows little contrasting power because it is not able to reach the inner regions of the tumor.

tumoral mass when 15_Block-M-PTX-FA is used while, in comparison, Endorem shows little contrasting power because it is not able to reach the inner regions of the tumor. However, most of the contrasting agent still ends up in the liver.

Figures 4.3, 4.4 and 4.5 offer a comparison of MRI Axial slices between mice treated with nanoparticles with folic acid, nanoparticles without folic acid and Endorem, respectively. Pre-injection images, 1h post-injection and 24h post-injection slices are shown. It can be noticed that, after 24 hours (the typical time checkpoint for MRI injection of SP CA), sample 15_Block-M-PTX-FA reaches the surface of the tumor (see again arrows). Endorem performed similarly, but the targeting efficiency was noticeably lower both at 1h and 24h after the injection. When comparing the functionalized nanoparticles with the non-functionalized system, a rough estimate of the decrease in T_2 in the tumoral region yields a 15-20% decrease for the former and 3-4% for the latter.

In addition, on the animals treated with 15_Block-M-PTX-FA a measurement of diameter of tumor masses was performed, measuring the diameter of tumor masses in MR slices, to monitor the effect of Paclitaxel on tumor growth. After 11 days from the injection of 15_Block-M-PTX-FA(115/15) the rate of tumor growth was of 81.16% (calculated on three animals MR images) compared with the value of the animal treated with Endorem in which the percentage of tumor growth, after eleven days, is of 132.9%. Histological slices of tumor masses monitored at different time points were collected. The images showed the presence of necrotic areas in the periphery of the tumor mass, due to the effect of paclitaxel conveyed by the nanoparticles. Thus the reduced rate of tumor growth is the direct consequence of the presence of PTX.

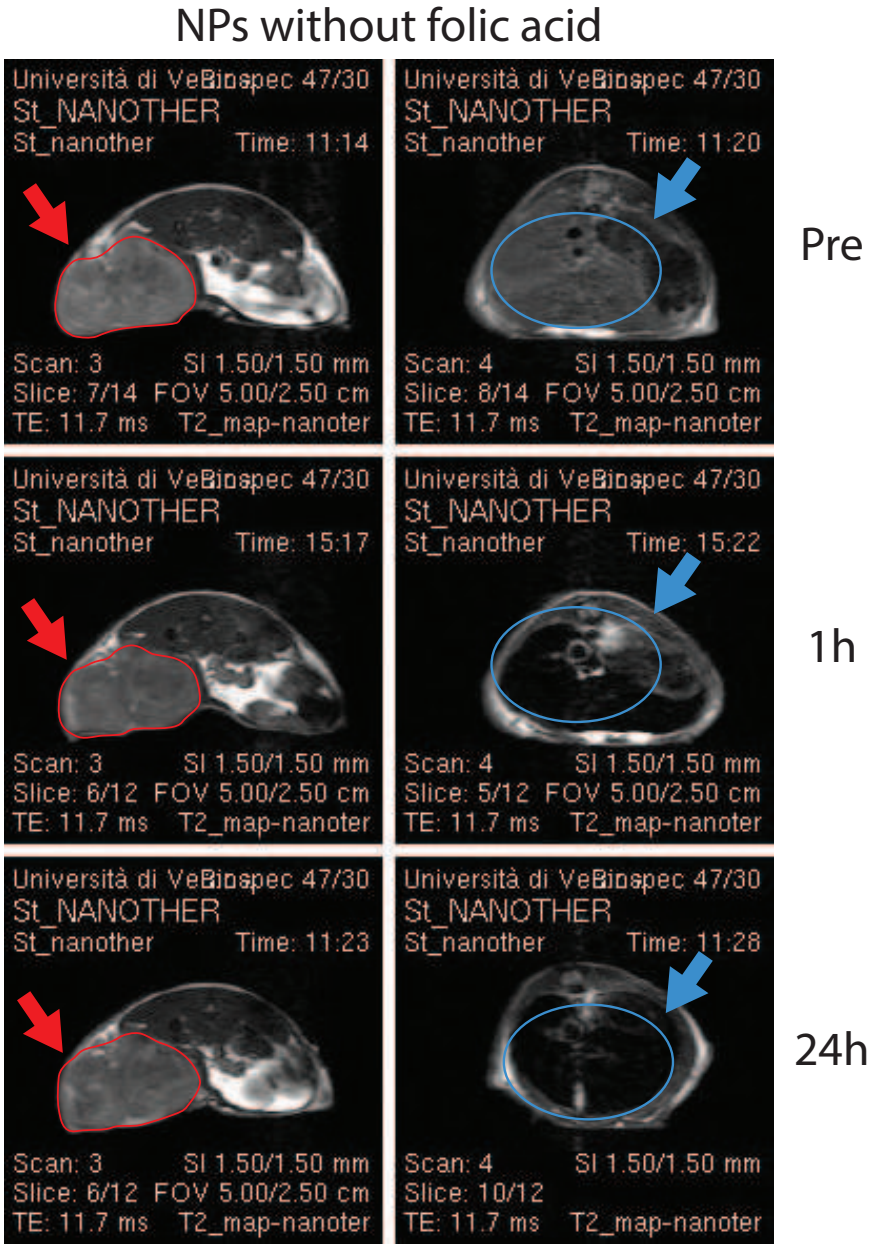

Figure 4.3 – Axial MRI slices of the tumoral mass and the liver of animals treated with **15_Block-M-PTX**, i.e. a sample *not grafted with folic acid*. Contrast condition is shown before injection (top row), after 1h (middle row) and after 24h (bottom row). The tumoral mass is circled in red and indicated by a red arrow in the left-hand column images. The liver is highlighted with a blue line and arrow in the right-hand column images. The performance of the contrast agent is here very poor, and can be compared with the results of Endorem, in fig. 4.5: the inner regions of the tumor are not reached by either **15_Block-M-PTX** and Endorem.

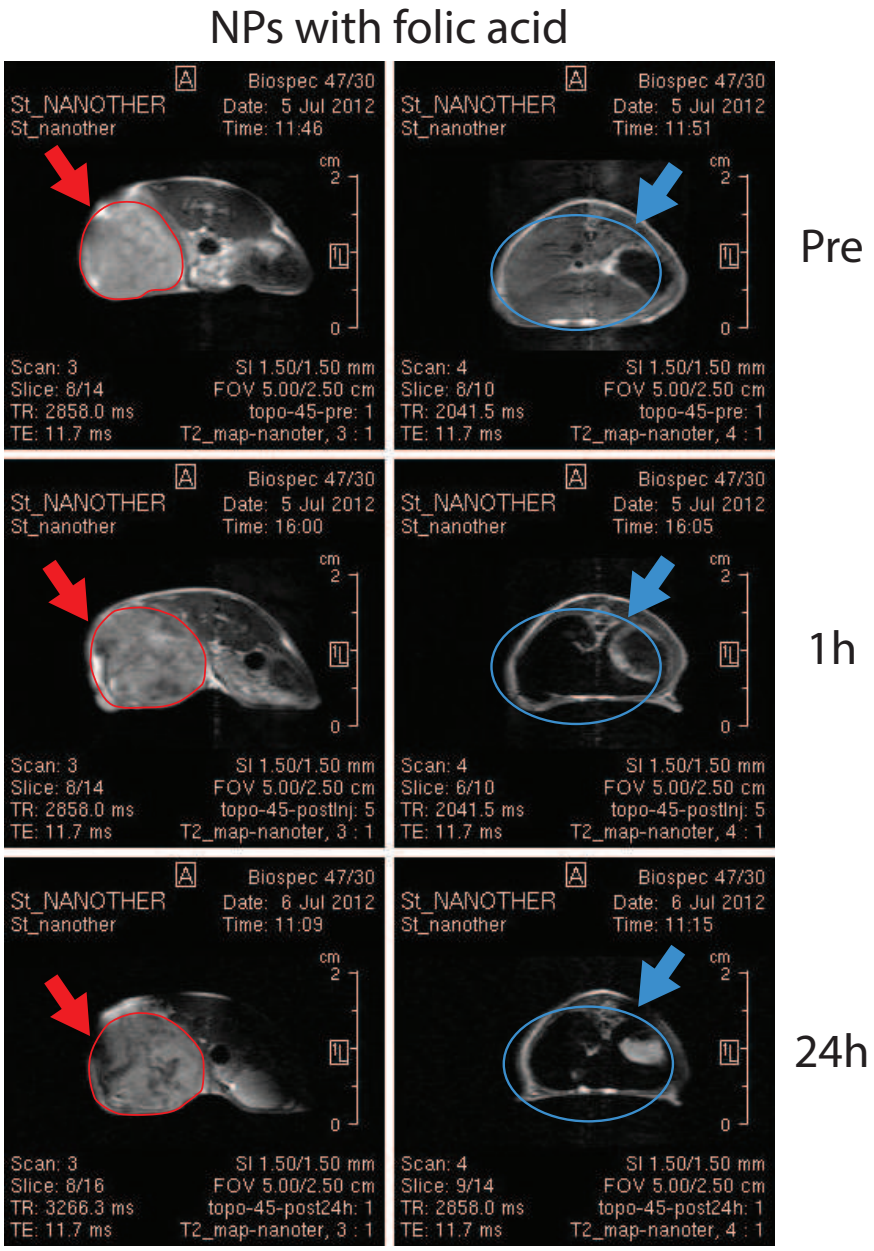

Figure 4.4 – Axial MRI slices of the tumoral mass and the liver of animals treated with **15_Block-M-PTX-FA**, i.e. *with folic acid*. Contrast condition is shown before injection (top row), after 1h (middle row) and after 24h (bottom row). The tumoral mass is circled in red and indicated by a red arrow in the left-hand column images. The liver is highlighted with a blue line and arrow in the right-hand column images. If compared to either Fig. 4.3 or Fig. 4.5, it is evident that the addition of a targeting method greatly enhances the diffusion of the functionalized contrast agent into the inner tumoral regions. This effect is best observed comparing the images taken at the 24h checkpoint in Fig. 4.3, 4.4 and 4.5.

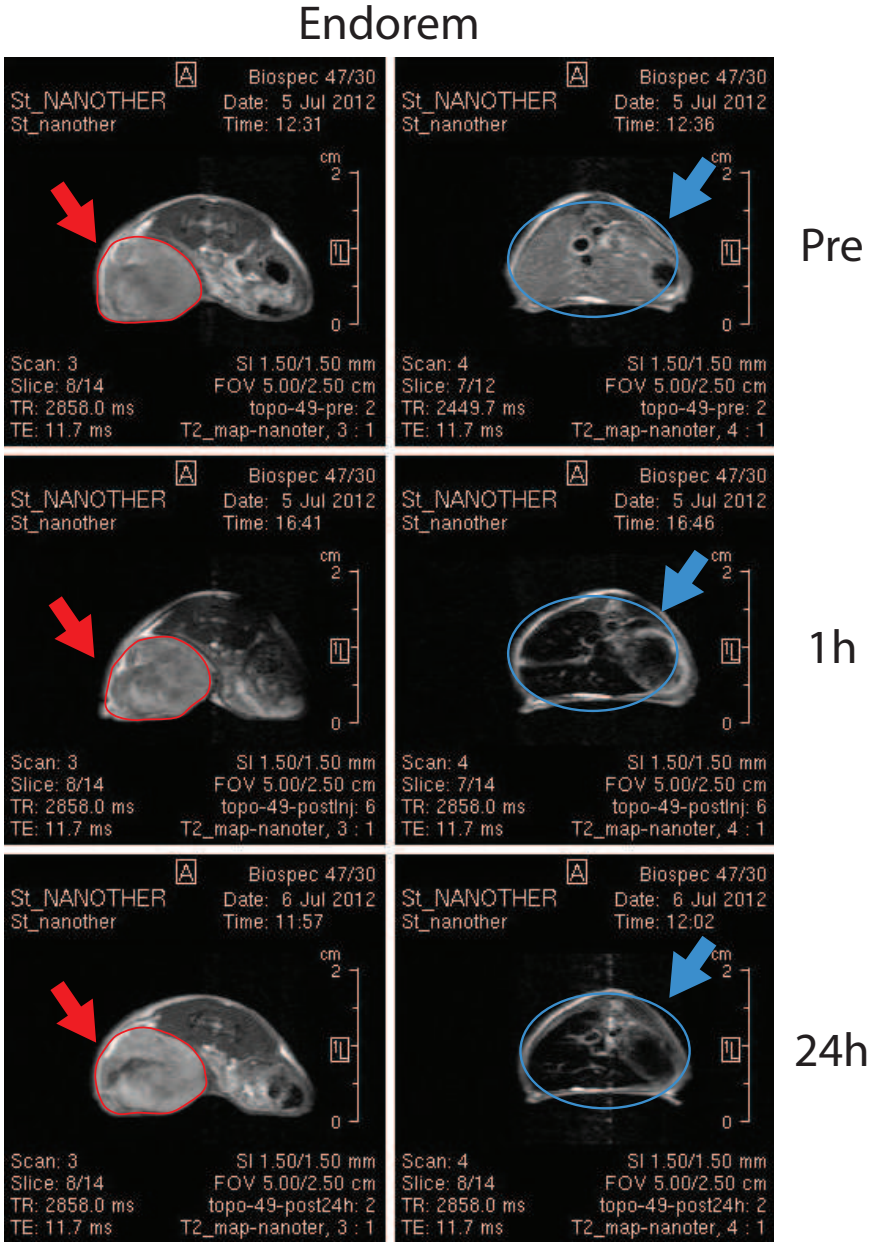

Figure 4.5 – Axial MRI slices of the tumoral mass and the liver of animals treated with **Endorem**. Contrast condition is shown before injection (top row), after 1h (middle row) and after 24h (bottom row). The tumoral mass is circled in red and indicated by a red arrow in the left-hand column images. The liver is highlighted with a blue line and arrow in the right-hand column images. As stated in Fig. 4.3, the inability of Endorem in targeting the inner part of the tumor is the reason behind the poor performance of Endorem.

General Conclusions

This thesis explored the magnetic properties and spin dynamics of nanoscopic iron oxide particles mainly through NMR techniques. Magnetic nanoparticles have been studied for a long time with a broad variety of techniques; this work finds its place alongside the investigations carried out with dynamic spectroscopy methods such as EPR, FMR, ^{57}Fe-NMR and Mössbauer, providing novel ^{1}H-NMR measurements, a new take on the standard approaches to the study of the spin dynamics of these systems.

For the fundamental physics part of the work, four samples made of an iron oxide core encapsulated in a sugar or polymer shell were selected to cover four different core sizes: 3nm, 4nm, 7nm and 12 nm. The static magnetic characterization proved that all samples are superparamagnetic above their blocking temperature T_B (ranging from $\sim$ 20 to $\sim$ 280 K), which increases with the size of the particle. Energy barrier distributions were extracted from zero-field-cooled M versus T curves, and the dependence of the blocking temperature on the magnetic field was compared to the results found in the literature: the main result is that all samples are definitively distant from the 'free particle' regime and sizeable interparticle interactions could be observed both by static magnetometry and by dynamic AC susceptibility. Analysis of AC susceptibility further confirms that a glass-like magnetic state is indeed a feature of all investigated samples. The present analysis supports two hypothesis, either a super-spin-glass or a canted disorder at the surface / whole volume of the particle, this last one being especially probable in the smaller samples.

The ^{1}H-NMR investigation revealed a strong inhomogeneous broadening of the ^{1}H spectra at low temperatures (1.5 MHz for the sample with smallest diameter), a phenomenon that is associated to the progressive slowing down of the spin fluctuations on cooling and to the strong hyperfine coupling with nuclei. The largest spectra were recorded on the smaller samples (3 – 4 nm), where the magnetic lattice consists of canted spins that create a very inhomogeneous magnetic environment at the proton sites.

The nuclear spin-lattice longitudinal relaxation rates were measured versus temperature in the range $1.5 < T < 300$ K at different applied fields ($H = 2.7$ – 16.6 kOe), and interpreted with a simple phenomenological model, yielding an estimate of the energy barrier probed during the NMR experiment. The main result is the finding in all samples of an anomaly in $1/T_1$ whose position in temperature increases with increasing core size. The position of the anomaly is almost independent on the applied magnetic field H and its the amplitude scales as $1/H$. The proposed model accounts for the anomaly by considering a single correlation time and assuming its temperature dependence to be equal to that of the Néel relaxation time of the particle, and introduces a log-normal

distribution of anisotropy energy barriers.

No significant effects from interparticle interactions have been observed at the NMR fields of measurement, because the high magnetic field completely quenches any dipolar interaction-driven magnetic order; thus, any dynamic contribution that would be generated by the internal hyperfine field fluctuations associated with the onset of such state at low applied fields can be safely neglected at NMR fields. On the other hand, the effects of a decoupled dynamics core/surface could possibly be observed in samples with core diameter in the range $5 < d < 9$ nm, such is the case of the 7 nm sample, featuring both a low temperature peak and an intermediate temperature peak in $1/T_1$. $d \simeq 12$ nm seems to be approximately the limit for an NMR investigation versus temperature in the range $T < 300K$ since above 12 nm the blocking temperature seen by the NMR measurement is found at temperatures higher than 300K.

Mössbauer spectroscopy quantitatively confirmed the dynamics seen by ^1H-NMR on Sample **1**, which can be described as the freezing of iron magnetic moments toward the collectively blocked state (below ~ 40 K). In-field Mössbauer experiments also evidenced that the order of Fe spins in each 3nm iron oxide particle below T_B is not collinear but canted, a result which is also in good agreement with the speculations from AC susceptibility measurements.

Both the results of Chapter 1 and 2 proved that the anisotropy energy barrier distributions survive even when a high magnetic field is applied, especially in the case of small samples ($d <\sim 5$ nm), a phenomenon that further support the hypothesis of a strongly disordered magnetic configuration of each magnetic particle.

Future works on the topics of this thesis shall include a more refined ^{1}H-NMR investigation on ad-hoc prepared samples, a comparison between ^{1}H-NMR data and ^{57}Fe-NMR data on the same materials and also a joint analysis of Mössbauer spectra and NMR data on samples with size $d > 3$ nm. An NMR theory specifically tailored for coated magnetic nanoparticle systems, possibly based on first-principle Hamiltonians, is still missing and would be of great value for the successful continuation of the research line.

The contributions to the applicative part of the Ph.D. project have been detailed in Chapter 3 and 4. Chapter 3 presented the experimental NMR data and analysis of a number of systems based on ferrite nanoparticles with different core sizes, magnetic species, organic coatings and solvents. All the chosen materials classify as ideal candidates to be used as superparamagnetic contrast agents for MRI diagnosis.

Preliminary AC susceptibility measurements revealed that all systems are composed of interacting magnetic particles, thus the Vogel-Fulcher expression for the Néel relaxation time τ_N proved to be the best choice, and the one that better reconciles with the NMR results. Indeed, dispersion NMR measurements were carried out on the sample series to record the longitudinal and transverse relaxivities, r_1 and r_2; the systematic fitting of r_1 profiles with Roch's model yielded excellent results, providing an estimation of τ_N in line with the AC susceptibility experiments. The samples were also characterized within the

framework of a universal law that describes the r_2 values on a broad range of core sizes on the basis of simple assumptions.

The comparison between different iron oxides established that Cobalt ferrites would be the best candidate for a novel MRI negative contrast agent, although the optimal option in terms of biocompatibility is magnetite, also because of the very high r_2 values when coated with either a sugar or a polymer. The need to compromise between high contrast efficacy and high cellular uptake limited the selection of a suitable candidate to those particle with size $5 < d < 20$ nm; then, the last chapter was dedicated to the presentation of preliminary in-vivo experiments on mice injected with a 12 nm magnetite sample coated with a block polymer and grafted with folic acid for efficient tumor targeting and Paclitaxel, an anti-tumoral drug, for drug delivery. MRI images proved that contrast enhancement is excellent, while targeting efficiency is sufficient but adjustments and further improvements are needed. Project updates of this research line should take into account the possibility of sacrificing some contrast power by using smaller particles, in favor of a more efficient targeting system.

Appendices

^{1}H-NMR study of the spin dynamics of fine superparamagnetic nanoparticles

Status

Published on Physical Review B.
ID: **Phys. Rev. B 85, 174426 (2012)**.

Authors

L. Bordonali, Y. Furukawa, M. Kraken, F. J. Litterst, C. Sangregorio, M. F. Casula, and A. Lascialfari.

Abstract

We report the broadband ^{1}H-NMR study of the temperature spin dynamics of nearly monodisperse dextran-coated γ-Fe_2O_3 magnetic nanoparticles. We observed a maximum in $T_1^{-1}(T)$ that decreases in amplitude and shifts toward higher temperatures with increasing field. We suggest that this is related to the progressive superparamagnetic spin blocking of the ferrite core. The data can be explained by assuming a single electronic spin-spin correlation time and introducing a field-dependent distribution of anisotropy energy barriers.

Introduction

Over the last 30 years a substantial number of studies concerning the magnetic properties of superparamagnetic (SPM) nanostructures have been published, an effort motivated by the interest in the fundamental physics of low-dimensional magnetic systems and a widespread impact on medical and technological applications [22]. However, the issue of broad polydispersity has hampered the advances in this fields for a long time and only recently it has been possible to synthesize SPM nanoparticles with a sufficiently narrow volume distribution,[152] thus enabling more detailed studies of the physical mechanisms regulating the single particle as well as the collective magnetic behavior. The magnetism of SPM ferrite nanoparticles is usually modeled by Néel's model which describes, in single domain particles, a spin-blocking process controlled by the magnetic anisotropy energy barrier, although more complicated and refined models have

been developed to overcome its limitations. A crucial issue not taken into account by Néel's model is the different spin dynamics of the uncompensated surface spins with respect to the core ones .[113, 153] Moreover, magnetic interparticle interactions of dipolar character, always present to some extent in a powder sample, give rise to complex behavior when coupled with surface effects.

Techniques such as Mössbauer spectroscopy and electron magnetic resonance spectroscopy have been successfully employed to gain insights into the spin dynamics of ferrite nanoparticles[154, 113, 155, 65]. On the other hand, no attempt has been made so far to explore the local spin dynamics on a broad temperature range by NMR techniques, the actual papers in the literature being limited to NMR spectra of nuclei belonging to magnetic ions showing low-temperature spin freezing.[156] NMR has already been successfully employed for the study of the magnetic properties of molecular iron clusters, such as Fe_6,[25] Fe_8,[26, 27] Fe_10[28] and Fe_{30}[29] where an enhancement in $1/T_1$ at temperatures of 10–30 K revealed dynamics driven by the coupling of the paramagnetic ions with acoustic phonons [30]. The same intent is shared by the investigation of very small iron-based nanoparticles, taking the NMR research on iron complexes a step further on the scale of the spin-systems dimensions.

In this paper we present an attempt to address the problem of the spin dynamics of fine magnetic nanoparticles (MNPs) by measuring the ^{1}H-NMR spectra, longitudinal and transverse relaxation rates on dry powders of dextran coated γ-Fe_2O_3 (maghemite) nanoparticles. Our investigation was made possible by the magnetic coupling of the hydrogen nuclei of the polymer shell surrounding the particles with the iron spins of the ferrite core via dipolar and eventually contact hyperfine interaction with protons of oxydriles at the surface of the ferrite core. Thus, even though the probing nuclei do not sense single local spins of the ferrite core, the mechanisms behind the dynamical behavior of the nanoparticle magnetization can be accessed. It should be also pointed out that the presence of the organic shell conveniently allows to rule out the presence of sizable additional interactions such as Ruderman-Kittel-Kasuya-Yoshida (RKKY) superexchange or interfacial exchange couplings that would lead to a more complex scenario.

Findings from the NMR investigation are supported by a comparison with the results of ^{57}Fe Mössbauer spectroscopy experiments, also reported in this paper.

Synthesis of γ-Fe_2O_3 particles

The synthesis of the iron oxide nanocrystals was performed by coprecipitation under alkaline conditions of Fe(II) and Fe(III) (Ref. [33]) in the presence of dextran. An amount of 5.5 g of dextran (Leuconostoc mesenteroides, average molecular weight 9.000–11.000 gmol^{-1}) was dissolved in 2 ml of distilled water. Then 1 ml of a $2M$ solution of iron (II) chloride tetrahydrate ($FeCl_2 \cdot 4H_2O$, $\geq$99%) in deionized and degassed water and 4 ml of a $1M$ iron(III) chloride hexahydrate ($FeCl_3 \cdot 6H_2O$, 97%) solution were deoxygenated by purging with

nitrogen for 30 min at room temperature and were then added to the dextran solution under stirring. Then 50 ml of a freshly prepared $1M$ NH_3 (28–30%) solution was then added dropwise over 30 minutes into the mixture at room temperature under magnetic stirring. A color change from brown to black was observed in the reaction mixture during the addition of ammonia solution. The dextran amount with respect to the overall reaction volume is 10 wt%, and the resultant mixture was stirred for a further hour to promote particle growth. The final pH was recorded to be around 9.5. The particles were then purified from unbound polymer by three cycles of washing and magnetic collection and finally dried at 60 °C for 2 days. Figure 4.6 displays the TEM images of the dextran-coated γ-Fe_2O_3 sample and the measured size dispersion. The core diameter and hydrodynamic diameter distributions of the prepared material were investigated by means of TEM and dynamic light scattering measurements. We found an average ferrite core diameter of 3.0 ± 0.5 nm and an average hydrodynamic diameter of 122 ± 11 nm (polydispersity index 0.4).

AC and DC magnetic susceptibility

Magnetic data were obtained by ac and dc magnetic susceptibility measurements, performed on a MPMS-XL7 Quantum Design superconducting quantum interference device (SQUID) magnetometer in the temperature range 2–300 K and applied fields H = 50 Oe, 3.7 kOe, 6.8 kOe and 14.4 kOe. For ac measurements the amplitude of the ac field was $H_{\mathrm{ac}} = 3$ Oe and investigated frequencies were $\nu_{\mathrm{ac}} = 1, 4, 16, 63, 250$ and 1000 Hz in zero and applied dc fields. Hysteresis loops were recorded in the $H = [-50\,\mathrm{kOe}, +50\,\mathrm{kOe}]$ field range at $T = 5$, 300 K.

Figure 4.7 shows zero-field-cooled (ZFC) and field-cooled (FC) magnetization curves measured at 50 Oe, 3.7 kOe and 14.4 kOe between 2 and 300 K. The departure of the ZFC/FC magnetization curves and the peak in the ZFC curve are characteristics of SPM nanoparticles, the peak marking the so-called blocking temperature T_B. It is remarkable that a blocking temperature can be found even for very high applied fields (14.4 kOe) as confirmed by the surviving cusp in the ZFC magnetization curve. The position of the maximum decreases with increasing field, as it would be expected.[50] The corresponding magnetization loop at 5 K is shown in the inset of Fig. 4.7: the magnetization does not reach a saturation value either at room temperature or at 5 K and it stands well below the value 80 emu/g, the saturation magnetization in bulk maghemite. It is commonly accepted that, in a core–shell framework, an high field irreversibility is the signature for the presence of disorder due to canted surface spins.[49, 16, 14, 99] To investigate the behavior of the anisotropy energy barrier at high applied fields and to gain better insight into the field dependency of the barrier distribution, we measured the ac susceptibility curves in applied magnetic dc fields $0 \leq H_{\mathrm{dc}} \leq 10$ kOe. Remarkably, an average barrier Δ can be extracted by ac measurements at all fields, by fitting the plot of the relaxation time τ as a function of temperature with an Arrhenius func-

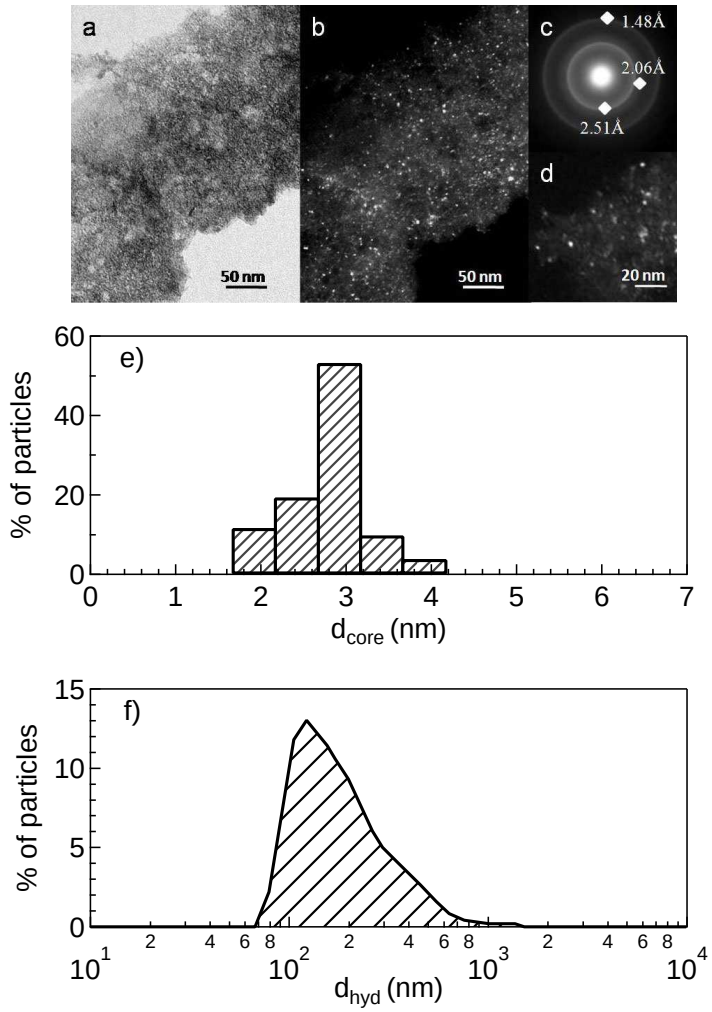

Figure 4.6 – Transmission electron microscopy images of the dextran–iron oxide sample under (a) bright field and (b) dark field mode and (c) the corresponding selected area diffraction; (d) close-up dark field view of the sample. The two graphs at the bottom display (e) the magnetic core diameter and (f) the hydrodynamic diameter distributions.

tion $[\tau(T) = 2\pi/\nu(T) = \tau_0 exp(\Delta/T)]$. The values of τ were obtained from the maximum of χ'' using the relation $\omega\tau = 1$, ω being the working frequency. The parameters Δ and τ_0 extracted from ac data are (Δ, τ_0) = (630.12 K, 1.499×10^{-18} s/rad), (183.92 K, 8.445×10^{-13} s/rad), (66.29, 2.766×10^{-7} s/rad), respectively for $H = 0$ Oe, 3.7 kOe and 6.8 kOe. Since τ_0 usually assumes values in the range 10^{-9}–10^{-12} s for noninteracting superparamagnets in zero applied field, our results imply that Néel's model breaks down and that the activation energy is temperature dependent, a partly expected result on the basis of the imbalance of the two wells of the energy-level diagram when a magnetic field is applied. Unphysical τ_0 values are commonly encountered when magnetic nanoparticles are coupled by dipolar interactions (see Ref. [42] and references therein). The rather large values for Δ also reflect the presence of such couplings.

In this respect, the formation of a spin-glass-like state was previously pro-

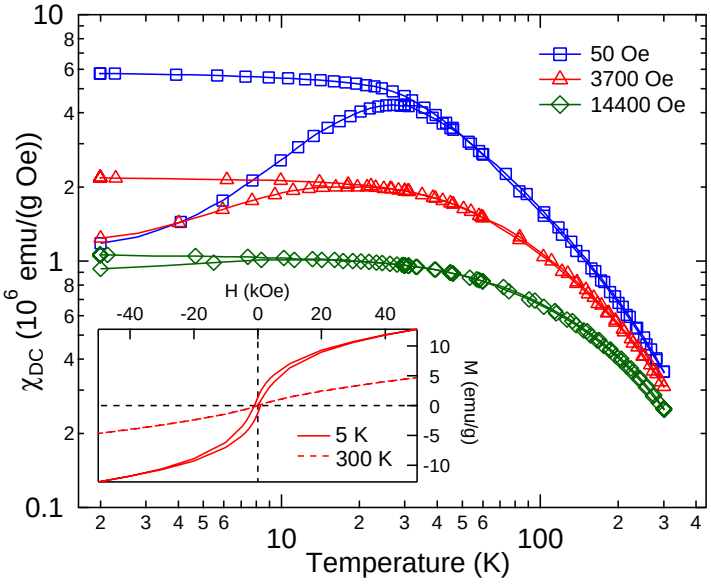

Figure 4.7 – (Color online) The dc Susceptibility FC/ZFC curves vs T at three different fields. An irreversibility temperature is definable for all three data sets. Inset: Hysteresis cycle at $T = 5$ K and $T = 300$ K.

posed to account for the dynamics observed by the ac technique in ferromagnetic and ferrimagnetic nanoparticle systems of varying sizes; in some cases the freezing to a superspin-glass state has been related to strong interparticle interactions. The interpretation of such dynamics, however, is rather difficult, since the onset of a spin-glass-like state could be labeled either as a cooperative effect between the SPM superspin of each ferrite nanoparticle or a consequence of the magnetic frustration between the iron spins at the surface layer of each particle, following from the uncompensated chemical bonds and lattice symmetry breaking. In very small particles, such as those studied in this paper, it seems plausible that a disordered magnetic state covering the whole particle could be found at low temperatures. On the other hand, as pointed out in Ref. [49], the high field irreversibility, witnessed by an unsaturated hysteresis cycle, rules out this hypothesis in favor of a different scenario that sees the core and surface regions as very distinct from one another, the disordered region being limited to the surface layer only.

To test the hypothesis of interparticle interactions leading to a spin-glass-like state we followed a procedure already applied to γ-Fe_2O_3 nanoparticles[13], fitting the ac data at zero applied static field to the critical slowing-down law:

$$\tau = \tau_0 \left[T_g(\omega)/T_g - 1\right]^{-z\nu}, \tag{4.1}$$

where $z\nu$ is the product of the dynamical critical exponent z and the critical exponent ν associated with the correlation length. No temperature dependence of the attempt time τ_0 has been considered in the investigated temperature range. $T_g(\omega)$ has been extracted by $\chi'(T)$ as the temperature of the curve maximum at each working frequency ω (see Fig. 4.8 (a) and inset). T_g has

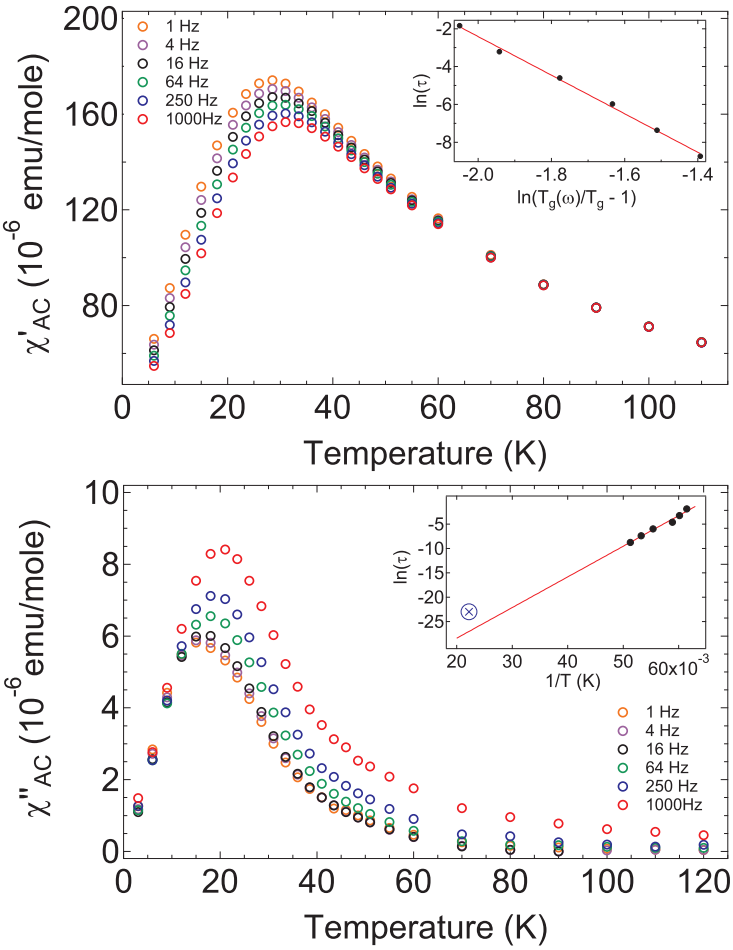

Figure 4.8 – (Color online) Temperature dependence of the (a) in-phase and (b) out-of-phase components, $\chi'(T)$ and $\chi''(T)$, of the ac magnetic susceptibility at different excitation frequencies. The arrows indicate increasing frequencies. Inset of (a): log-log plot of τ vs $T_g(\omega)/T_g - 1$ for the dextran-capped γ-Fe_2O_3 nanoparticles and fit to the dynamic slowing-down power law. Inset of (b): Arrhenius plot extracted from ac χ'' susceptibility at zero field and fit. The data point from Mössbauer experiments is included and indicated with a circled cross symbol (refer to Sec. 4.5 in this paper).

been fixed to the temperature of the maximum in the ZFC curve at $H = 50$ Oe, $T_g = T_B = 25.5\ K$. We found $\tau_0 = 1.22 \pm 0.62 \times 10^{-10}$ and $z\nu = 10.2 \pm 0.3$; the value for the exponent $z\nu$ is in excellent agreement with values expected for the three-dimensional Ising-like spin glasses ($10 < z\nu < 12$) and with other results on maghemite nanoparticles (Parker *et al.*[13]: $z\nu = 10.3 \pm 0.3$, $d = 9$nm; Leite *et al.*[57]: $z\nu = 8.0 \pm 0.2$, $d = 3$nm). Still, the ambiguity between a "collective" superspin-glass state and a "single-particle" spin-glass-like state remains since, although using a critical slowing-down model is qualitatively correct, this method fits either case.

Regarding the NMR investigation presented here, it is worth noticing that a superspin-glass state is easily destroyed after the application of a moderate magnetic field;[104] thus, any dynamic contribution that would be generated by the internal field fluctuations associated with the onset of a 'collective' glassy state

at low applied static fields can be safely neglected at fields greater than $\sim 10^2$ Oe. We conclude that under the relatively intense fields of a NMR experiment ($H_0 > 10^3$ Oe) the aforementioned ambiguity is removed and no superspin-glass state can be found; hence, it is only possible to probe the superparamagnetic thermal activation of the inner shell of the γ-Fe_2O_3 core and, eventually, the effects of a faster dynamics of the disordered surface layer.

In a perfectly monodisperse sample with negligible interparticle interactions one expects that the anisotropy energy barrier would disappear if a high magnetic field was applied; however, the presence of a disordered surface layer creates a complex multiminima energy landscape which should broaden the distribution [61] while the joint effect of the applied field and dipolar interactions shifts the average anisotropy barrier toward lower values, introducing substantial low-energy contributions [44]. An estimate of the Zeeman energy E_Z at 3.4 and 14.4 kOe yields values of the order of 10^2–10^3 erg while the particle magnetic anisotropy energy E_A as calculated from the bulk magnetocrystalline anisotropy constant $K_{\text{bulk}} = 4.7 \times 10^4$ erg/cm^3 is only of the order of $10 \div 10^2$ erg. However, it is quite common to witness a difference of two orders of magnitude[105, 50, 106] between the bulk anisotropy energy density and the effective anisotropy energy density in a nanoparticle with size $d \leq 5nm$, because additional sources of anisotropy come into play (i.e., shape, surface, magnetostriction contributions, and the dipolar interaction contribution). Thus, it is not unusual to have $E_Z < E_A$ and a double-minima (or multiminima) energy landscape even at the high fields commonly found in solid-state NMR experiments.

As we proceed with the discussion of ^{1}H-NMR measurements we show that the hypothesis of a reduced energy barrier is consistent with the results of the analysis on the nuclear spin-lattice relaxation (NSLR) rate temperature dependence.

^{57}Fe Mössbauer spectroscopy on γ-Fe_2O_3 MNPs

^{57}Fe Mössbauer spectroscopic measurements have been performed at temperatures ranging from 4 to 300 K on an absorber with an area density corresponding to about 0.2 mg ^{57}Fe/cm^2. A conventional transmission spectrometer with sinusoidal velocity sweep was used. As source served about 12 mCi of ^{57}Co in a rhodium matrix kept at room temperature. The absorber containers were made of nylon and fixed within copper clamps. Temperature control and measurement were performed with a Lakeshore DRC-91C using a calibrated Si diode attached to the copper clamp. The absorbers were kept in a static He exchange gas atmosphere of about 0.2–0.4 mbar in a flow He cryostat (CRYOVAC). Temperature stability was better than 0.1 K.

Figure 4.9 shows a representative set of absorption spectra at various temperatures. Clearly visible is the gradual broadening of the magnetically split hyperfine pattern at lowest temperatures leading to a collapse to a doublet spectrum above about 50 K. This scenario is typical for relaxation spectra of

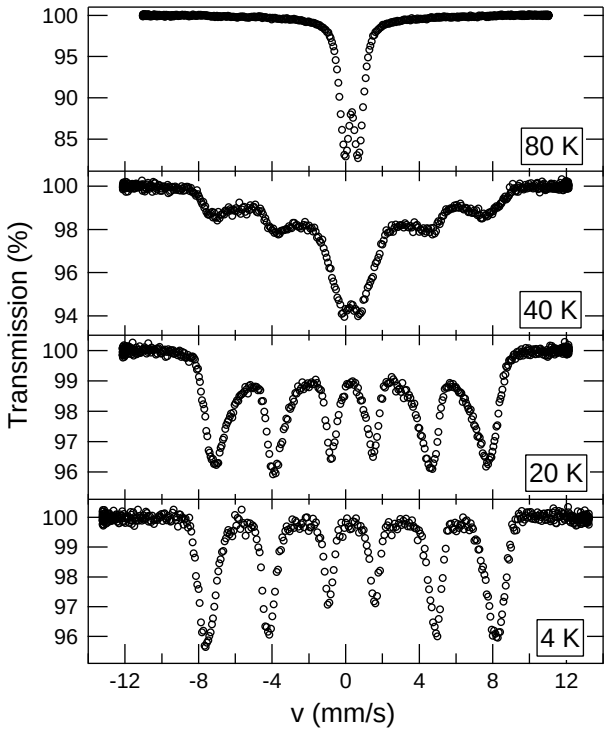

Figure 4.9 – Collection of zero-field Mössbauer spectra recorded for the γ-Fe_2O_3 sample at various temperatures.

very small particles. (For a recent review, see Ref. [[65]].) At low temperatures the fluctuation rates of particle moments are slow compared to nuclear Larmor precession of ^{57}Fe, and a magnetically split pattern may be observed. At high temperatures the fluctuations lead to motional narrowing, i.e. the time-averaged hyperfine magnetic field vanishes and only the nuclear quadrupole interaction in the local electric field gradient at the Fe site (a doublet spectrum) is observed. The collapse occurs for fluctuation rates between 10^{10} and 10^{11} s^{-1}. Due to a distribution in fluctuation frequencies caused by a distribution in particle size and anisotropy energy this is not a sharp transition but smeared over some temperate range. Typically one defines the blocking temperature at the time scale of Mössbauer spectroscopy as the temperature where about 50% of the spectral area reveals magnetic hyperfine interaction, whereas the other 50% are (super)paramagnetic. In our case this takes place around 45 K.

In Fig. 4.9 we have deliberately not included fits of theoretical models to the experimental data. The estimate of the blocking temperature is practically independent of the method of analysis. (We report on a detailed analysis comparing various methods for noninteracting and interacting particles, multilevel relaxation, superferromagnetic model, etc., in a forthcoming publication.) In Fig. 4.8 (b) we have included the blocking temperature derived from the Mössbauer data in the inset. As can be seen it is in excellent agreement with the extrapolation of the ac data.

It should be noticed that spectra recorded even at the lowest temperatures

still reveal a strong temperature-independent line broadening. This is in contrast to spectra found from other small particles of ferrites which show sharp spectra (see examples given in Ref. [[65]]). The broadening therefore cannot be related to magnetic dynamics. We interpret it with inhomogeneous magnetic distributions of hyperfine fields due to the shell structure of the particles having strongly canted spins.

^{1}H-NMR experiments on γ-Fe_2O_3 MNPs and discussion

^{1}H-NMR NSLR rates T_1^{-1} and spectra were measured using a standard pulsed NMR spectrometer in the temperature range $[1.5K, 120K]$ at $H = 3.7$ kOe, 14.4 kOe. The ^{1}H NMR signal at $T > 120$ K was very low and thus it was not possible to collect data in a reasonable acquisition time. The recovery curves of the nuclear magnetization have been collected by integrating the spin-echo signal following a sequence of saturating radio frequency pulses (90°-180° / 90°-90° sequences). All ^{1}H-NMR spectra have been measured point by point by integrating the echo signal while sweeping the external field around the central field position $H_L = \omega_L/\gamma_P$, where γ_P is the proton gyromagnetic ratio and ω_L is the fixed proton Larmor frequency.

The ^{1}H-NMR line shapes for $T = 1.3, 10$, and 120 K at $H = 3.7$ kOe are reported in the inset of Fig. 4.10; for the sake of simplicity we did not report the spectra at 14.4 kOe. All spectra have a Lorentzian symmetric line shape from which the full width at half maximum (FWHM) was calculated and plotted in Fig. 4.10 against the measuring temperature. The temperature dependence of the NMR linewidth is ascribed to an inhomogeneous component, i.e., a distribution of hyperfine dipolar fields at the nuclear proton sites due to interaction of protons with the Fe magnetic moments. It should be also noted that (i) the protons closer to the surface, responsible for the probing of the surface layer dynamics, are experiencing a distribution of dipolar fields due to the disordered magnetic configuration of the electronic spins in the layer; (ii) the spectra are intrinsically broadened because of inequivalent proton sites (i.e. different Larmor frequencies) in the dextran coating. A distribution from orientational disorder of powders must also be taken into account. At both fields the linewidth progressively increases with decreasing temperature, from 0.2–0.6 MHz at ~70 K to ~1.5 MHz at ~1.5 K, following the progressive freezing of local spins. Under $T = 4$ K the NMR linewidth saturates, marking the achievement of a completely blocked state of the SPM moments.

The recovery of the longitudinal nuclear magnetization was found to be non-exponential at both applied static fields $H = 3.7$ kOe, 14.4 kOe. The deviation from the monoexponential behavior can be related to a distribution of relaxation rates due to the presence of inequivalent proton sites and an orientational distribution in the powders. Therefore, in order to measure a consistent relaxation parameter, an effective T_1 reflecting the fastest relaxing nuclei, defined as the time at which the nuclear magnetization has recovered 40% of the equilibrium value, was taken into account.

Figure 4.11 reports the values of T_1^{-1} as a function of temperature for two different applied static fields. Our main result is the observation of a maximum in $T_1^{-1}(T)$ at $T \sim 45$ K for both applied static fields. An additional shoulder is also visible around 4 K on the curve collected at $H = 3.7$ kOe.

In order to give an interpretation of the spin dynamics behind the behavior in $T_1^{-1}(T)$ we assumed a simple Bloembergen-Purcell-Pound-like (BPP-like) spectral density function,[157] which can be obtained from the original Moriya theory of nuclear relaxation in paramagnets,[103, 102] of the form $J(\omega, T) = A(T)\chi(T)T\tau_c(T)/(1 + \omega^2\tau_c(T)^2)$, where $\tau_c(T)$ is the temperature-dependent electronic spin-spin correlation time. The prefactor $A\chi(T)T$ represents the mean square value of the local hyperfine field fluctuations and contains the temperature dependence of the static magnetic susceptibility $\chi(T)$. Assuming that the correlation time $\tau_c(T)$ is the one governing the relaxation of the magnetization of the internal SPM core, we have taken into account that for SPM nanoparticles a "simplified" Arrhenius law is obeyed: $\tau_c(T) = \tau_0 \mathrm{Exp}(\Delta/T)$. Although the choice of a standard thermally activated dynamics model is controversial when interparticle interactions are not negligible, the heuristic model employed to explain the NMR data is greatly simplified assuming to a first approximation an Arrhenius-like law instead of a more appropriate expression, e.g. a Vogel-Fulcher law, which would still be considered a phenomenological solution but becomes senseless when T approaches the critical temperature T_C.

Despite the good monodispersity of our sample, as previously discussed, the application of an external magnetic field and the existence of a disordered surface layer give rise to a distribution of energy barriers. For this reason in the expression of T_1^{-1} we assumed a lognormal distribution $P(E)$ of energy barriers E, with median value $\bar{E}$ and scale parameter σ_E. In doing so, we guarantee that the energy barrier distribution can be related to a volume distribution modified by the surface effect, also allowing for lower energy contributions. The heuristic formula employed to fit the NSLR data is

$$\frac{1}{T_1}(T) = A\chi(T)T \int_0^\infty P(E) \frac{\tau_c(T,E)}{1 + \omega_L^2 \tau_c^2(T,E)} dE, \tag{4.2}$$

where

$$P(E) = \frac{1}{E\sigma_E\sqrt{2\pi}} \exp\left(-\frac{\left[\ln E - \ln(\bar{E})\right]^2}{2\sigma_E^2} \right),$$
$$\tau_c(T,E) = \tau_0 \exp(-E/T).$$

The integration in Eq. (4.2) was performed numerically during the fitting procedure. The NSLR data were fitted to Eq. 4.2 and the resulting curves are reported in Fig. 4.11. The fit yields energy barriers distributions peaked at $E_{peak}/k_B = 58.2K$ for H=3.7 kOe and $E_{peak}/k_B = 23.8K$ for H=14.4 kOe and parameters $\sigma_E = 0.786$ and $\sigma_E = 0.963$, respectively, while the values of τ_0 extracted from the $1/T_1$ data are $\tau_0 = 8,35 \times 10^{-11}$ s/rad and 2.60×10^{-11} s/rad, respectively, in good agreement with the expected values for a typical

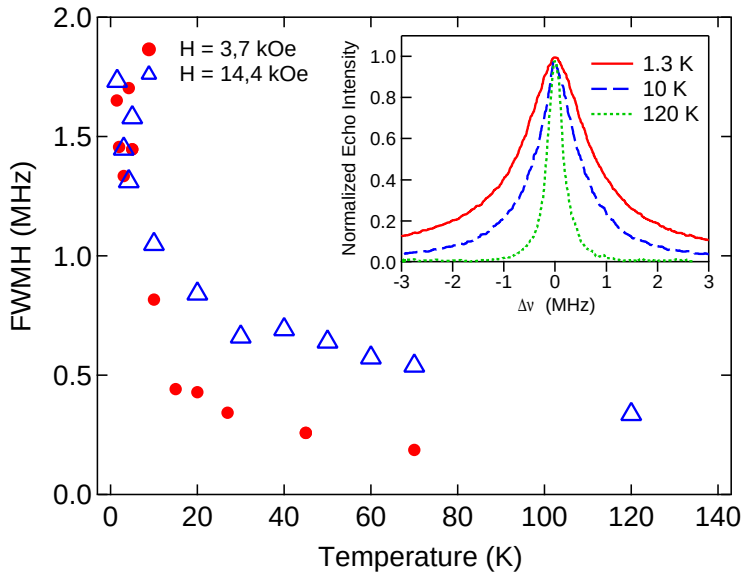

Figure 4.10 – (Color online) Temperature dependence of the proton NMR spectrum linewidths collected at temperatures above 1.5K with evidence for a superparamagnetic spin blocking. The inset shows a selection of measured spectra.

superparamagnet. Magnetic parameters extracted by DC Magnetometry and NMR measurements are collected in Table 4.1.

We suggest that the difference between the attempt time τ_0 measured by χ_{AC} and ^{1}H-NMR is possibly due to the presence of interparticle dipolar interactions having different effects on local (detected by NMR) and bulk (revealed by χ_{AC}) spin dynamics [158, 159, 102, 160]. The NMR probes are mostly sensing the magnetic environment at a very local level, thus being more sensitive to the single particle superspin and to the surface layer dynamics while any cooperative effects driven by the interparticle dipolar coupling have been quenched by the high static NMR field, as discussed in section 4.5.

The inset of Fig. 4.11 reports the energy barrier distributions related to the fit curves in the main plot; it is clearly visible how the mean value of the distribution moves toward lower energies, as it is generally expected when increasing the external static field. Under the current interpretation of the phenomenon, it should not come as a surprise that the position of the anomaly in T_1^{-1} turns out to be nearly the same for both applied fields: considering the expression of the spectral density function of Eq. 4.2, the higher the measurement frequency (higher fields), the higher in temperature the position of the peak should be; however, the shift toward lower energies in the distribution of energy barriers pushes the peak for $H = 14.4$ kOe ($\omega_L \simeq 61$ MHz) down in temperature, in apparent alignment with the peak for $H = 3.7$ kOe ($\omega_L \simeq 16$ MHz).

Finally, the presented heuristic model does not explain the presence of a shoulder at low temperature. This shoulder can be tentatively attributed to an enhancement due to the aforementioned increased contribution to the barriers distribution at nearly-zero energy values originating from dipolar couplings

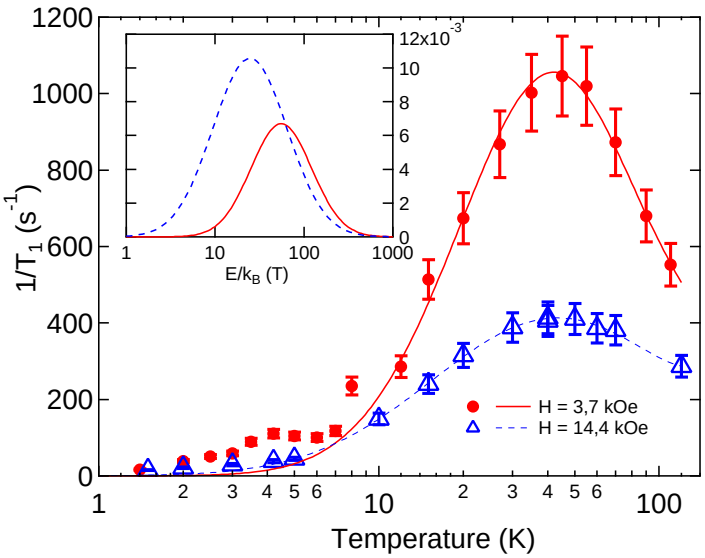

Figure 4.11 – Average Proton spin-lattice-relaxation rate (T_1^{-1}) plotted vs temperature for two external magnetic fields. Inset: semi-log plot of the distributions of energy barriers related to the two investigated static fields, as extracted from eq. 4.2.

DC	$H_{c,5K}$	$T_{B,50Oe}$	$T_{B,3.7kOe}$	$T_{B,14.4kOe}$
Parameters	-1020 Oe	25,5 K	18.9 K	12.5 K
NMR	$\tau_{0,3.7kOe}$	$\tau_{0,1.44T}$	$E_{3.7kOe}$	$E_{14.4kOe}$
Parameters	8.35×10^{-11} s	2.60×10^{-11} s	58.24 K	23.88 K

Table 4.1 – Collection of DC and NMR key parameters obtained from the fitting of the experimental data (see text).

between particles [44] and the application of a magnetic field. As already mentioned in section 4.5, the temperature independent broadening observed in Mössbauer spectra collected at $T \sim 4$ K supports the hypothesis of a highly disordered magnetic phase at the surface. Thus, alternatively, the anomaly at $T \sim 4$ K in $T_1^{-1}(T)$ could be explained as an effect of the fluctuations of the surface spins being faster than the core spin fluctuations, yielding a freezing of surface spins at lower temperatures [155].

The effects of both the core and surface dynamics on NMR quantities greatly depend on the coupling of Fe spins and H nuclei in the outer organic shell via transferred hyperfine interaction; however, a theoretical estimate of the values of hyperfine coupling constant would require a density functional approach to the problem and for the case of even the smallest nanoparticles ($d \simeq 1$nm) the feat would be quite challenging if not unfeasible. Therefore, further experimental and theoretical effort is needed at low temperatures in order to confirm the presence of the mentioned effects.

Conclusions

In summary we have presented the first broad band ^{1}H-NMR study of the spin dynamics of nearly monodisperse γ-Fe_2O_3 nanoparticles encapsulated in an organic shell. We report an enhancement in the proton NSLR rates $1/T_1$ at low temperatures and postulate that the observed dynamics is related to a SPM moment blocking regulated by a field-dependent distribution of anisotropy energy barriers, modified by interparticle dipolar interactions and surface effects. Data from Mössbauer spectroscopy experiments support the dynamics observed by NMR and also give hints on possible low-temperature surface phenomena. Different results between the AC susceptibility measurements and the NMR experiments have been been found and interpreted in the light of the different dynamics observed by the two non-equivalent techniques: the AC data, analysed with a critical slowing down law commonly applied to the study of spin-glass states in condensed matter, yielded results compatible with both a single-particle spin-glass-like state in the surface layer of the maghemite core or a collective superparamagnetic spin-glass state originating from the magnetic dipolar couplings in the nanoparticle ensemble. The latter hypothesis has been excluded from the interpretation of the NMR data on the basis of the fragility of the spin-glass-like collective state to a magnetic field in interacting magnetic particles systems.

The most promising perspective opened by our results concerns the possibility of detecting dynamical effects on magnetic nanoparticles by means of standard solid state NMR spectroscopy and relaxometry, which have only been applied to colloidal suspensions of magnetic nanoparticles [161, 68, 162], though in completely different frameworks. We also reasonably put forward the idea that the NMR technique is a valuable complement to Mössbauer spectroscopy on magnetic nanoparticles when properly coated with a material featuring a sensitive NMR probe.

Future experimental work should also consider the convenience of resorting to NMR for fundamental studies on mesoscopic quantum effect in very small ($d < 2$ nm) magnetic particles [73, 74], at the boundary between classical and quantum behavior. The application of NMR to small nanoparticle may therefore give relevant contributions to the effort of filling the gap between the world of magnetic clusters ($S_{tot} < \sim 30$) and the classical world of the larger nanoparticles ($S_{tot} > \sim 100$).

Journal

PRB Published

Dependence of nuclear relaxation rates on composition and size in nearly monodispersed ferrite nanoparticles.

Status

Submitted to Journal of Physics: Condensed Matter.

Authors

L. Bordonali, T. Kalaivani, K. P. V. Sabareesh, C. Innocenti, E. Fantechi, C. Sangregorio, M. F. Casula, L. Lartigue, J. Larionova, Y. Guari, M. Corti, P. Arosio, A. Lascialfari.

Abstract

We present a systematic experimental verification of the superparamagnetic relaxation by means of dynamic magnetic measurements and ^{1}H-NMR relaxometry, on ferrite-based nanosystems with different composition, various core sizes and dispersed in different solvents. The application of a heuristic model for the relaxivity allowed a comparison between the reversal time of magnetization as seen by NMR and the results from the AC susceptibility experiments, and an estimation of fundamental microscopic properties. A good accordance between the NMR and AC results was found when fitting the AC data to a Vogel Fulcher law. Key parameters obtained from the model have been used to evaluate the impact of the contribution of the magnetic anisotropy energy to the relaxivity curves and estimate the minimum approach distance of the bulk solvent, thus remarking once more the power of NMR as a probe to determine the local spin dynamics.

Introduction

Whenever a new magnetic nanoparticle-based MRI contrast agent is designed, a number of parameters have to be kept under control, such as core size and shape, chemical composition, degree of aggregation, surface states, biocompatibility and contrast efficiency. There is by now a vast literature dedicated to the characterization of such nanosystems, covering these issues separately or collectively depending on the target application of the materials: currently, magnetic nanoparticles appear extensively in biological and medical sciences (see Ref. [163] and references therein) where they are employed both as agents for MRI contrasting[164] and multimodal diagnostics[165], and as advanced therapeutic agents for magnetic hyperthermia[166] or localized drug delivery nanovectors[167].

The slow dynamic behavior observed in these systems is interpreted on the base of the concept of single magnetic domain magnetic particles[42, 6] which assigns to each magnetic nanoparticle a single large collective magnetic moment. The traditional tool to test the effectiveness of a superparamagnetic (SPM) contrast agent, prior to *ex-vivo* and *in-vivo* experimentation, is the evaluation of its longitudinal (r_1) and transverse (r_2) relaxivity as a function of the externally applied static field, *i.e.* the increase of the nuclear relaxation rate per unit of magnetic center with respect to the bulk solvent. Relaxivity is defined as $r_i = [(1/T_i)_{meas} - (1/T_i)_{dia}]/C$ $(i = 1, 2)$, where $(1/T_i)_{meas}$ is the nuclear relaxation rate measured on a sample solution with concentration C in mmolL^{-1} of the magnetic center and $(1/T_i)_{dia}$ is the nuclear relaxation rate of the diamagnetic host solution. High r_1, r_2 and saturation magnetization, M_S, are generally required for a MRI contrast agent (CA) to reach high efficiency.[164] A considerable number of studies on SPM nanoparticles-based CA are available[168, 169], whose relaxivities fit the NMR dispersion (NMR-D) profiles to the well-known model developed by Roch *et al.*.[32] However, to the best of our knowledge, no work has attempted to systematically track the effect of the magnetic anisotropy on the relaxometric properties of magnetic nanoparticles by evaluating the evolution of the key parameters of Roch's theory with the particles' sizes and composition. In this paper we take into account the NMR-D and AC results obtained by a systematic study on samples which mainly differ for the core size, core composition and the surface coating material. This study offers the opportunity to evaluate the flexibility of the above model of SPM relaxation as a consistent fitting method for NMR-D data (part of them new) on a set of SPM nanoparticle-based compounds with widely varying structural parameters. Most importantly the model enables an investigation of the role of the different magnetic anisotropy in the NMR properties of an SPM CA. Since at first order the total magnetic anisotropy energy increases with the nanoparticle volume, a study of the NMR dispersion profiles as a function of the nanoparticle size permits, in principle, to cover a wide range of magnetic anisotropy energies. In addition, coupling the effect of the volume with the broad selection of anisotropy constants (almost two orders of magnitude) by varing the magnetic ion, the effective anisotropy energy may span over an ever wider range.

Sample	d_{TEM} nm	M_S emu/g	$E_{A,Arr}/k_B$ K	$\tau_{0,Arr}$ s/rad	$\tau_{N,Arr}$ s/rad	$E_{A,VF}/k_B$ K	$\tau_{0,VF}$ s/rad	T_0 K	$\tau_{N,VF}$ s/rad
S-Mag/W-1	4.1(0.6)	77	337.0	1.13×10^{-12}	3.47×10^{-12}	216.0	9.28×10^{-11}	3.0	1.92×10^{-10}
S-Mag/W-2	6.7(0.8)	75	1118.5	1.24×10^{-12}	5.17×10^{-11}	885.0	1.39×10^{-11}	5.59	2.80×10^{-10}
S-Mag/W-3	18.2(1.1)	68	8420.7	8.65×10^{-21}	1.34×10^{-8}	2479.9	1.07×10^{-12}	94.0	1.81×10^{-7}
P-Mag/(W&T)-1	5.5(0.6)	38	611.8	4.48×10^{-15}	3.44×10^{-14}	611.8	4.48×10^{-15}	0	3.44×10^{-14}
P-Mag/(W&T)-2	8.0(0.8)	52	865.7	9.96×10^{-11}	1.78×10^{-9}	763.3	2.88×10^{-10}	2.98	3.77×10^{-9}
P-Mag/(W&T)-3	12.0(0.7)	43	636.0	4.47×10^{-10}	3.72×10^{-9}	620.9	5.40×10^{-10}	0	4.29×10^{-9}
MnFe/T-1	3.0(0.2)	44	189.3	7.14×10^{-13}	1.34×10^{-12}	189.3	7.14×10^{-13}	0	1.34×10^{-12}
MnFe/T-2	4.8(0.1)	44	-	-	-	-	-	-	-
MnFe/T-3	6.0(0.2)	42	1795.9	9.10×10^{-14}	3.62×10^{-11}	1035.5	3.50×10^{-11}	17.3	1.36×10^{-9}
CoFe/T-1	8.6(1.1)	80	-	-	-	-	-	-	-
CoFe/T-2	8.6(1.1)	80	13569.4	7.13×10^{-25}	3.14×10^{-5}	3784.5	1.31×10^{-14}	127	4.32×10^{-5}
CoFe/T-3	6.0(1.4)	72	2611.1	2.68×10^{-15}	1.62×10^{-11}	1093.8	5.21×10^{-11}	32.6	3.11×10^{-9}
CoFe/T-4	5.0(1.2)	56	2661.0	4.32×10^{-14}	3.07×10^{-10}	1667.9	8.26×10^{-12}	21.8	3.31×10^{-9}

Table 4.2 – Main magnetic parameters for sample series S-Mag (Rhamnose-coated magnetite), P-Mag (Oleic Acid-coated or polymer coated magnetite), MnFe (Oleic Acid-coated Manganese Ferrite) and CoFe (Oleic acid-coated Cobalt Ferrite). From left to right in each row: TEM estimated particle diameter and standard deviations in parentheses, saturation magnetization, Arrhenius law estimate of the anisotropy energy barrier, τ_0 prefactor and Néel relaxation time, Vogel Fulcher law's estimate of the anisotropy energy barrier, τ_0 prefactor, T_0 phenomenological parameter and Néel relaxation time.

Relaxivity model of SPM relaxation

The relaxivity model can be briefly outlined as follows: a first contribution to the nuclear relaxation arises from the diffusion of solvent protons into the inhomogeneous magnetic field created by the large magnetic moments of the superparamagnetic nanoparticles (Curie relaxation, dominating at high frequencies); a second contribution stems from the fluctuations of the SPM magnetic moment on each particle (Néel relaxation, dominating at low frequencies) and is characterized by a relaxation time, τ_N, related to the rate of the magnetization flip from one direction along the axis of easy magnetization to the opposite one. The reorientation time is assumed to be much shorter than the particle rotation correlation time τ_R (Brown relaxation), i.e. $\tau_N \ll \tau_R$. When the applied static field B_0 is low, the spectral density describing the ^{1}H nuclear spin relaxation is given by the Freed function,[137] J^F, which accounts for both Curie and Néel relaxations. At high field, Curie relaxation dominates and the spectral density function is given by the Ayant function,[138] J^A. The relaxation rates r_1 and r_2 are calculated by averaging over θ, the angle between the external field axis and the anisotropy axis, an approximation valid only for small enough particles; for instance, the threshold for magnetite particles is around 20 nm[32]. The exact model starts from a spin Hamiltonian approach and, by using the density matrix, expresses the nuclear relaxation rates $1/T_1$ and $1/T_2$ as a function of frequency. Roch's exact model was the first to explicitly account for the effect of magnetic anisotropy which produces an attenuation of the low field dispersion of the NMR-D profiles in particles with diameter $d >$ ~10 nm. However, when the number of spins is relatively high (greater than $\sim$ 1000) *i.e.* the nanoparticles have an average diameter greater than 2 – 3 nm, this model requires prohibitive calculation times. As a good substitutive and simplified model, an heuristic expression was proposed in which the fitting variables are reduced to a manageable non-overparametrizing amount while keeping the underlying physical meaning. Roch et al. [32] linearly combined the relaxivity equations for the case of null anisotropy energy $E_A = 0$ with the equations for infinite anisotropy $E_A = \infty$, weighted with factors P and Q respectively and constraining to $P+Q \leq 1$. The last inequality accounts for the fraction of magnetization lost due to fast precession frequencies, *i.e.* the part of magnetization not contributing to the relaxation. The heuristic expression employed in this work to perform the fitting procedure is:

$$\begin{aligned} r_1 \;=\; & A(32\pi/135000)\mu_{SP}^2\gamma_I^2(N_aC/rD) \\ & \times\Big\{7P\tfrac{L(x)}{x}J^F\left[\Omega(\omega_s,\omega_0),\tau_D,\tau_{N,NMR}\right] \\ & +\Big[7Q\tfrac{L(x)}{x}+3(P+Q)(1-L^2(x)-2\tfrac{L(x)}{x})\Big] \\ & \times J^F(\omega_I,\tau_D,\tau_{N,NMR})+3L^2(x)J^A(\sqrt{2\omega_I\tau_D})\Big\} \end{aligned} \tag{4.3}$$

where μ_{SP} is the magnetic moment of each ferrite crystal, γ_I is the proton gyromagnetic ratio, r is the distance of minimum approach 'proton-magnetic ion', D is the self diffusion coefficient of the medium, N_a is Avogadro's number

and C is the molar concentration of nanoparticles; A is a constant introduced to readjust the global SPM moment (*i.e.* the SPM magnetization) with the one sensed by the probing nuclei at a local level; $L(x)$ is Langevin's function, where $x = \mu_{SP}B_0/k_BT$; the parameter τ_D is defined as $\tau_D = r^2/D$, while $\tau_{N,NMR}$ is the Néel relaxation time at room temperature; the label 'NMR' is added to distinguish this parameter from the analogous quantity yielded by the AC data analysis; ω_S and ω_I are the electron and proton transition frequencies, respectively; ω_0 is a free parameter included in the function Ω to recover the correct behavior of the low-field dispersion inflection point and assuring that it may never appear at a frequency lower than ω_0.

Materials

Four set series of CAs with magnetic core size ranging from 4 nm to 20 nm have been investigated:

- Rhamnose-coated magnetite NPS (S-Mag) [128]. Three Fe_3O_4 samples were synthesized by thermal decomposition of iron acetylacetonate and have controlled sizes of 4.1, 6.7 and 18.2 nm. Nanoparticles are functionalized with rhamnose derivative group according to a protocol described in Ref. [129].

- Oleate coted magnetite particles (P-Mag) [34]. This monodispersed hydrophobic nanocrystals of Fe_3O_4, synthesized by thermal decomposition of iron carbonyl, have average size of 5.5, 8.0 and 12 nm, respectively and were investigated both in toluene and water solution. The transfer into acqueous media was realized by coating with an amphiphilic polymer shell (poly(maleicanhydride)) whose long aliphatic domains intercalate with oleate molecules on the nanoparticle surface.

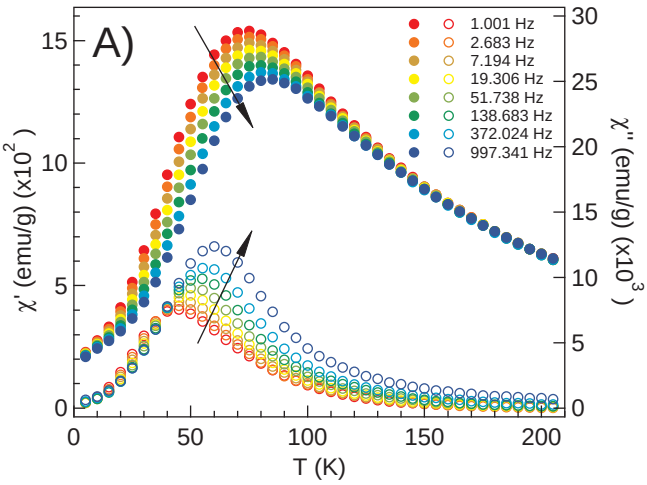

Figure 4.12 – FIG. 1. AC susceptibility in-phase χ' (solid circles) and out-of-phase χ'' (open circles) curves, with excitation frequencies in the 1-1000 Hz range for sample S-Mag/W-2. Arrows indicate increasing frequencies.

- Oleic acid coated Manganese Ferrite nanocrystals (MnFe) [130]. $MnFe_2O_4$ NPs were synthesized by thermal decomposition of metal carbonyl complexes $Mn_2(CO)_{10}$ and $Fe(CO)_5$ in the presence of oleic acid[131]. For $MnFe_2O_4$ nanocrystals the core average sizes are 3.1, 4.9 and 5.9 nm.

- Non-stoichiometric Cobalt Ferrite ($Co_xFe_{3-x}O_4$) NPs (CoFe) with two different sizes (8.6 nm and 5 nm) and different Co content ($x = 0.2$ and $x = 0.4$). The samples were prepared by thermal decomposition of Co and Fe acetylacetonate precursors[132]. In the following, the samples will be labeled as: CoFe-1 ($d = 8.5$ nm, $x = 0.4$), CoFe-2 ($d = 8.6$ nm, $x = 0.2$), CoFe-3 ($d = 5$ nm, $x = 0.4$) and CoFe-4 ($d = 6$ nm, $x = 0.2$).

For all samples, toluene-based colloidal solutions (hereafter labeled as T ferrofluids) were first obtained. Magnetite-based samples were then also transferred in water (W ferrofluids) after sugar or polymer coating procedure according to the considered series.

The DC magnetometry measurements, zero field cooled (ZFC) and field cooled (FC) and hysteresis measurements, previously measured [34, 130, 128, 132] confirmed that all samples are superparamagnetic at room temperature, having blocking temperature well below 300K. Transmission electron microscopy (TEM) analysis have revealed that all the samples are quasi-spherical-shaped and their size is lognormally distributed with normalized standard deviation much smaller than 0.3 for the most of the samples. Table 4.2 reports the average size and saturation magnetization values at 300K for each sample.

AC Susceptibility

AC Susceptibility measurements were performed on dry powder samples using Quantum Design MPMS-XL SQUID and Cryogenic S600 SQUID magnetometer, in the excitation frequency range 0.1 – 1000 Hz, the temperature range 2 – 300 K and zero static field.

The values of the Néel relaxation time τ_N at room temperature are also calculated from the AC results and compared to the estimate of τ_N from the NMR-D data analysis. Figure 4.12 reports the temperature dependence of the in-phase χ' and out-of-phase χ'' components of the magnetic susceptibility for sample S-Mag/W-2, as a typical example. The two components exhibit peaks that shift toward high temperature with increasing frequency. From AC susceptiblity data the parameters for the magnetization relaxation, i.e. the mean magnetic anisotropy barrrier E_A and the characteristic τ_0 attempt time, were inferred by fitting the frequency dependence of the maximum of the χ'' component to the Arrhenius law:

$$\tau = \tau_0 e^{\frac{E_a}{k_B T}} \tag{4.4}$$

where E_a is the average energy barrier for the reversal of the magnetization, τ_0 is the attempt time and k_B is the Boltzmann constant. According to the

Néel model, this law governs the temperature dependence of the magnetization relaxation for non-interacting superparamagnetic systems [170]. For the samples S-Mag/W-2, P-Mag/T-2 and P-Mag/T-3 the values of the pre-exponential factor τ_0 are in the range 10^{-9} – 10^{-12} s typical for isolated superparamagnetic nanoparticles, while for other samples the values of E_A and τ_0, are higher and smaller, respectively, than those usually observed in non-interacting systems. In order to investigate the possible presence of dipolar interparticle interactions, the temperature dependence of the relaxation time was also fitted to the Vogel-Fulcher law (VF), which accounts for such interactions by introducing the phenomenological parameter T_0 in the previous Arrhenius expression:

$$\tau = \tau_0 e^{\frac{E_A}{k_B(T-T_0)}} \tag{4.5}$$

The values so obtained for parameters E_A and τ_0 are in the typical range for superparamagnetic systems in most cases, except for P-Mag/(T&W)-1 and MnFeT-1, where, as evinced by the T_0 values of Table 4.3, it was not possible to fit the AC data to the VF expression without reverting back to the Arrhenius case ($T_0 \to 0$). The emergence of dipolar interactions can be ascribed to the nature of the samples used for AC measurements, which were in powder form or concentrated solutions of nanoparticles.

Conversely, particles in the more diluted solutions, as those employed in the NMR dispersion experiments, should be considered as non interacting. It should also be stressed that the AC susceptibility technique provides sample-averaged results, while NMR is a local probe and so less sensitive to the effects of long range dipolar interparticle interactions in solution: the diffusional motions of the particles generally average the short range interaction to zero and the long range interactions to a negligible amount [133]. None-the-less, a comparison can be attempted between the AC results and the NMR parameters, as we will show in the next section.

^{1}H-NMR Dispersion Measurements

^{1}H-NMR data were collected using two different pulsed FT-NMR spectrometers: (i) a Stelar SMARTracer for 10 kHz $< \nu <$ 10 MHz, and (ii) a Stelar Spinmaster for 10 MHz $< \nu <$ 65 MHz. Standard radio frequency pulse excitation sequences based on saturation recovery, CPMG and Hahn-Echo were used. We recorded the frequency dependence of the longitudinal and transverse NMR-relaxivity (NMR-D profiles) by measuring the longitudinal and the transverse nuclear relaxation times T_1 and T_2 in the frequency range 0.01 – 60 MHz, corresponding to an external magnetic field H = 23 Oe – 15 kOe, at room temperature.

In Fig. 4.13 we report the fitting curves of the experimental data collected on S-Mag/W, P-Mag/T, P-Mag/W and MnFe/T samples. During the fitting procedure of the NMR-D profiles with Eq. 4.3 we let the parameters A, P, Q, r and $\tau_{N,NMR}$ vary so that an estimation of the distance of minimum approach r and of the characteristic Néel relaxation time $\tau_{N,NMR}$ could be obtained as

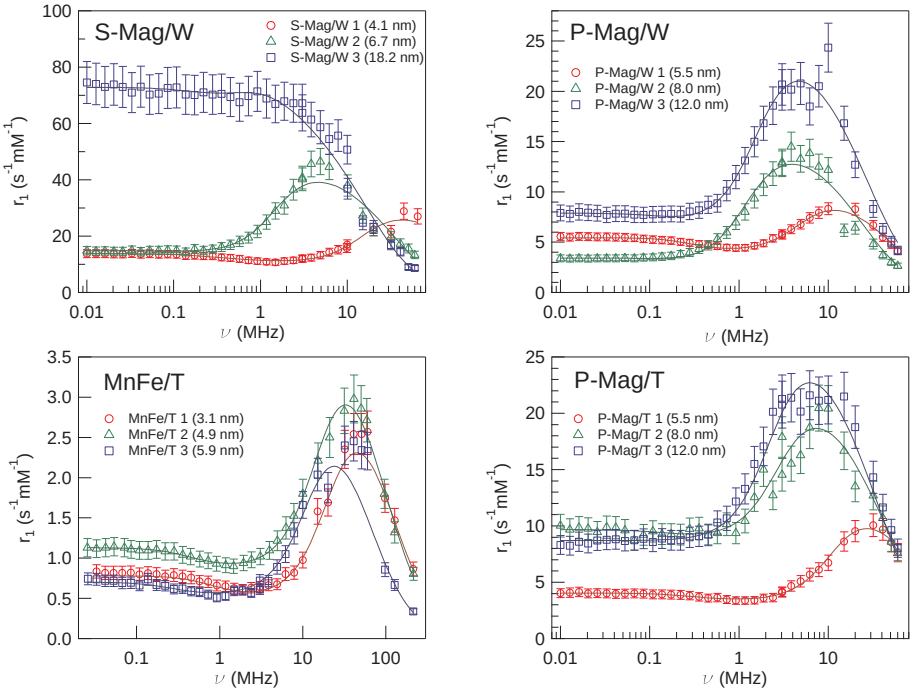

Figure 4.13 – Collection of longitudinal relaxivities r_1 (NMR-D profiles) sampled at room temperature between 0.01 MHz and 100 MHz for sample series S-Mag/W, P-Mag/T, P-Mag/W and MnFe/T. Solid lines between data points are the result of the data analysis with Roch's model (eq. 4.3).

	A	P	Q	$2r$ nm	d_{TEM} nm	$\tau_{N,NMR}$ s/rad
S-Mag/W-1	1.54	0.14	0.31	5.05	4.1	2.61×10^{-9}
S-Mag/W-2	0.30	0.08	0.91	11.25	6.7	2.16×10^{-9}
S-Mag/W-3	0.28	0.06	0.65	20.13	18.2	3.08×10^{-6}
P-Mag/W-1	0.45	0.34	0.66	9.17	5.5	2.82×10^{-9}
P-Mag/W-2	0.15	0.21	0.79	13.61	9.0	1.73×10^{-9}
P-Mag/W-3	0.40	0.18	0.86	13.13	12.0	2.33×10^{-9}
P-Mag/T-1	1.06	0.14	0.44	7.02	5.5	1.37×10^{-9}
P-Mag/T-2	0.57	0.08	0.87	10.52	9.0	2.75×10^{-9}
P-Mag/T-3	0.41	0.00	0.97	11.15	12.0	1.99×10^{-9}
MnFe/T-1	0.26	0.42	0.38	5.81	3	4.4×10^{-10}
MnFe/T-2	0.17	0.47	0.22	6.85	4.8	1.2×10^{-9}
MnFe/T-3	0.13	0.27	0.20	7.72	6.0	1.7×10^{-9}
CoFe/T-1	0.63	0.07	0.81	16.3	8.6	2.04×10^{-6}
CoFe/T-2	0.85	0.05	0.58	14.8	8.6	5.09×10^{-6}
CoFe/T-3	0.74	0.04	0.85	7.34	6.0	6.71×10^{-9}
CoFe/T-4	0.49	0.07	0.92	8.01	5.0	2.21×10^{-9}

Table 4.3 – Fit values from the analysis of ^{1}H-NMR-D profiles employing Roch's model. Refer to Fig. 4.14a for P/Q ratios.

well. Parameter D, which is the solvent self-diffusion coefficient, has been bound within the limits $2 - 3 \times 10^{-5} cm^2 s^{-1}$ to account for its variability due to the presence of superparamagnetic agents in the medium (see Ref. [171] for a dissertation on the role of the diffusion coefficient in the fitting of NMR-D profiles). The self-diffusion coefficient for toluene is similar to the one of water, being $2.7 \times 10^{-5} cm^2 s^{-1}$ at $T = 300K$, so the different medium does not undermine the evaluation of the NMR parameters from the samples dispersed in toluene.

Table 4.3 lists the output values for the main free parameters of Eq. 4.3 as obtained from the fitting procedure. Considering that r is a free parameter in the fitting procedure, the agreement between the particle diameters thus estimated and the corresponding values of d_{TEM} measured with the TEM is quite satisfactory, although far than perfect. Most notably, the $d_{NMR} = 2r$ values from NMR are always higher than their TEM counterparts. We believe that the difference is due to the diffusional motion of the solvent molecules: water (or toluene) molecules may diffuse only within a certain distance from the magnetic core since the organic coating partly blocks the brownian paths toward the core. Following this reasoning, d_{NMR} can be regarded as a distance of minimum approach that should tend to d in the limit cases of either naked magnetic particles or full penetration of water inside the coating. In the following, when discussing the effect of the particle size, we will refer to the magnetic core size d_{TEM}.

The free parameter P and Q have opposite trends as a function of d_{TEM}. Namely, as the core increases in volume, the total magnetic anisotropy energy increases as well, causing an enhancement in parameter Q, while P decreases. Since P and Q ultimately weight the contributions from the Zeeman energy and the magnetic anisotropy energy[32], the ratio P/Q should decrease with the particle size. This is indeed the general trend displayed by the P/Q ratios reported in Fig. 4.14a as a function d_{TEM}; a marked relative increase when the nominal diameter approaches $\sim$ 5 nm is present in all five investigated series but is the most pronounced in the MnFe/T and S-Mag/W series. This behavior is reflected by the curves in Fig. 4.13, showing for all samples a definite damping of the low-field dispersion when d_{TEM} increases over $\sim$ 10 nm, due to the increased anisotropy energy. The effect of the magnetic anisotropy energy increase with the average volume is the most dramatic for sample series S-Mag/W where the NMR-D profile for the largest particles loses the high-field peak, which merges into the low-field plateau. An analogous trend is found in P-Mag/T, P-Mag/W and MnFe/T series, also shown in Fig. 4.13, where the effect of magnetic anisotropy is still noticeable although less marked with respect to the S-Mag/W series since the effective magnetic anisotropy constant is lower in these samples with respect to the S-Mag sample.

An interesting remark can be made about the two P-Mag series: noticing that the corresponding P/Q values in Fig. 4.14a for samples P-Mag/W are shifted upwards with respect to the P-Mag/T series, lead to conclude that the transfer from the toluene solution to water had the effect of increasing the contribution from the Curie relaxation mechanism. We ascribe this phenomenon

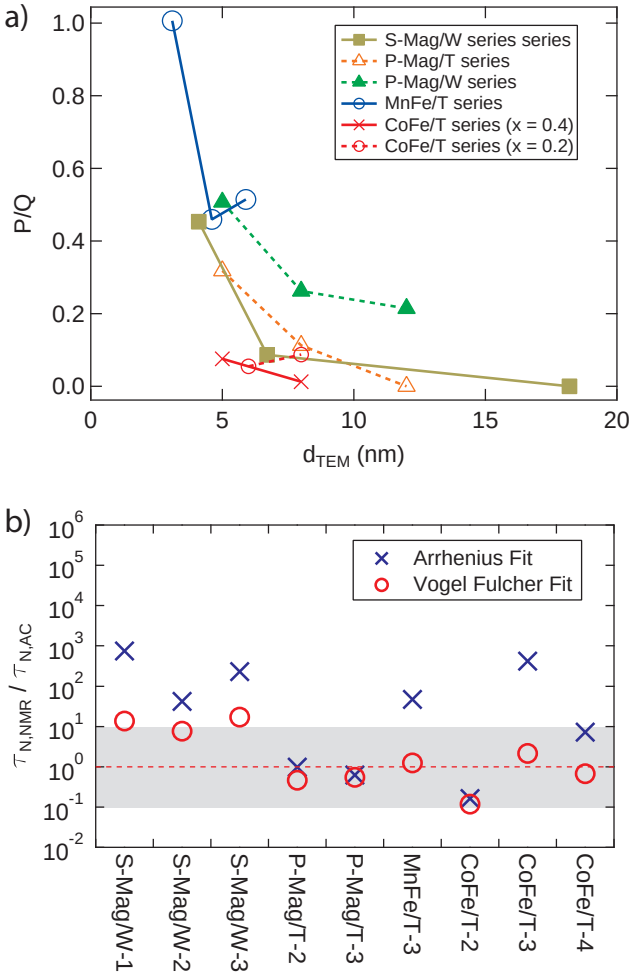

Figure 4.14 – a) P/Q ratios for all investigated samples. b) $\tau_{N,NMR}/\tau_{N,Arr}$ and $\tau_{N,NMR}/\tau_{N,VF}$ ratios for all investigated samples. The grey band in the graph covers the ratio range between 0.1 and 10, i.e. within one order of magnitude from value 1, indicated with a red dashed line. Points falling in this range identify a good agreement between AC susceptibility and NMR spectroscopy in evaluating Néel's relaxation time at room temperature.

to the lower distance of minimum approach of the solvent molecules in the P-Mag/T series with respect to the P-Mag/W samples (see the column for d_{NMR} in table 4.3), also considering that the P-Mag/W particles surface was further coated with an amphiphilic polymer for transfer in water, thus thickening the organic shell around the magnetic core. The case of Cobalt Ferrite is peculiar, because the increase in P/Q for the smaller particles is barely noticeable. The great enhancement in the anisotropy energy due to the Cobalt substitution is responsible for such a small difference between small and large particles: if we look at these results as a function of the Cobalt over Iron content in the magnetic material, no appreciable difference could be observed in the smaller particles when lowering the cobalt content from 15% (x = 0.4, in CoFe/T-1 and CoFe/T-3) to 7% (x = 0.2, in CoFe/T-2 and CoFe/T-4). A similar behavior

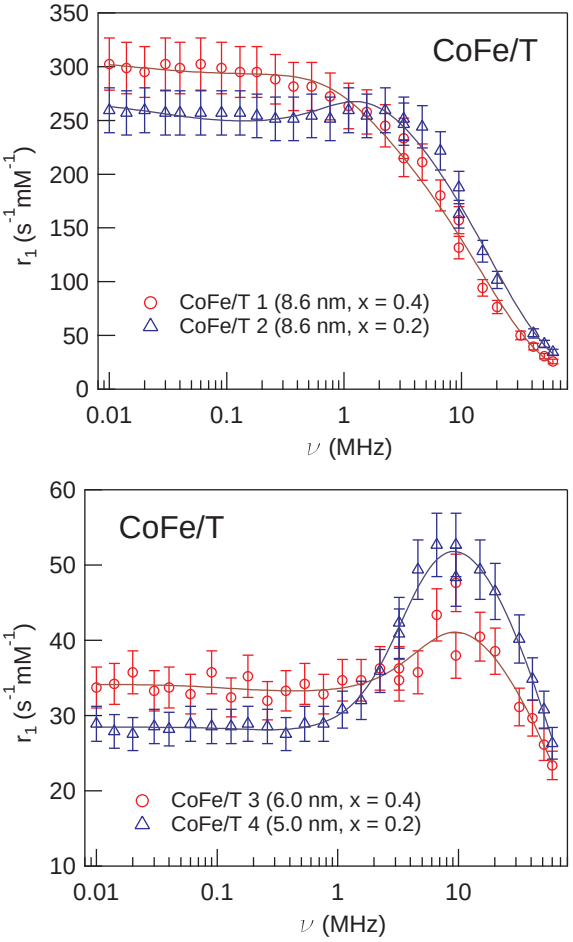

Figure 4.15 – NMR-D profiles and fitted curves for sample series CoFe/T between 0.01 MHz and 100 MHz.

was also reported by Roch *et al.* in Ref. [121]. This result was expected since the CoFe/T NMR-D profiles, displayed in Fig. 4.15, do not show any significant enhancement of the low field dispersion when halving the cobalt content. On the other hand, for the larger particles ($d \simeq 8.5$ nm), the difference between the magnetic anisotropy constant of $Co_{0.4}Fe_{2.6}O_4$ and that of $Co_{0.2}Fe_{2.8}O_4$[132] is enough to decrease the Q value in the latter with respect to the first, thus increasing the P/Q ratio by an appreciable amount.

To draw a comparison between the estimation of the Néel relaxation times at room temperature as extracted by NMR-D profiles and AC susceptibility analysis, in Fig. 4.14b we plotted the ratios $\tau_{N,NMR}/\tau_{N,Arr}$ and $\tau_{N,NMR}/\tau_{N,VF}$ for a selection of samples. As it can be noticed from the number of points falling within one order of magnitude from 1, there is a much nicer agreement between the NMR results with the AC results from the analysis with the VF law (7 out of 9 samples) than those extracted with the Arrhenius expression (4 out of 9 samples); in Fig. 4.14b the two outliers from the S-Mag/W series can actually be considered as good results, lying just on the border of the chosen

range. The need for inclusion of interparticle magnetic interaction in explaining the AC susceptibility data is then confirmed by the comparison with the NMR results.

Conclusions

We have systematically verified the excellent quality of the fitting results employing Roch's model for nuclear relaxation in SPM systems. We would like to stress that the importance of this experimental validation resides in the possibility of tracking the effect of the crystal's internal anisotropy energy, dampening the low-field dispersion, with the magnetic core-size of the particles. We successfully extracted the relative weights of Néel and Curie contributions to the ^{1}H nuclear magnetization relaxation and studied their dependence on magnetic core diameter and ion species, showing a marked decrease of the P/Q ratio as the magnetic anisotropy energy of the nanoparticle increases, as a consequence of both an increased core diameter and increased magnetic anisotropy energy density. The core diameters and Néel's relaxation times were also calculated through the fit of NMR-D data and compared with TEM and AC susceptibility measurements. As a result of the solvent molecules penetrating only to a certain extent into the organic coating of the particles, $d_{NMR}/2$ actually measures the distance of minimum approach to the center of the particle and thus d_{NMR} was found to be generally greater than d_{TEM}. Néel relaxation times, as measured by NMR, lie in the superparamagnetic range, as expected; a phenomenological Vogel-Fulcher law had to be applied for the AC susceptibility data analysis to recover a satisfactory agreement between NMR and AC data, since Néel's model breaks down in concentrated solutions and powders due to sizable dipolar interparticle interactions.

We would like to acknowledge Nanother Eu-FP7 project and PUR-2007 and PUR-2008 of Università degli Studi di Milano for funding support. The work was partly developed within the national FIRB project RINAME. We would also like to thank Prof. A. Roch for precious insights on the NMR-D heuristic model.

Redistribution of local spin density in Cr_7Ni antiferromagnetic molecular ring from ^{53}Cr-NMR

Status

Published on Journal of Physics: Condensed Matter.
ID: **J. Phys.: Condens. Matter. 24, 406002 (2012)**.

Authors

C. M. Casadei, *L. Bordonali*, Y. Furukawa, F. Borsa, E. Garlatti, A. Lascialfari, S. Carretta, S. Sanna, G. Timco, and R. Winpenny.

Abstract

We present ^{53}Cr-NMR spectra collected at low temperature in the heterometallic antiferromagnetic (AF) ring Cr_7Ni in the S=1/2 ground state with the aim of establishing the distribution of the local electronic moment in the ring. Due to poor S/N ratio we observed only one signal which is ascribed to three almost equivalent ^{53}Cr nuclei in the ring. The calculated spin density in Cr_7Ni in the ground state, with the applied magnetic field parallel and perpendicular to the plane of the ring, turns out to be AF staggered with the greatest component of the local spin $\langle s \rangle$ for the Cr^{3+} ions next to the Ni^{2+} ion. The ^{53}Cr-NMR frequency was found to be in good agreement with the local spin density calculated theoretically by assuming a core polarization field $H_{cp} = -11$ Tesla/μ_B for both orientations close to the value found previously in Cr_7Cd. The observed orientation-dependence of the local spin moments is well reproduced by the theoretical calculation and evidences the importance of single-ion and dipolar anisotropies.

Introduction

Antiferromagnetic molecular rings are an ideal playground for investigating magnetism at nanoscale. Recently there has been intense experimental and theoretical effort in the synthesis and investigation of nanoscale molecular magnetic systems, which are composed of a controllable number of transition metal ions [23]. A shell of organic ligands shields the individual molecular magnets from each other (steric hindrance) so that the magnetic interaction between the neighboring molecular magnets is negligibly weak and the observed magnetic properties of the bulk samples are considered to originate from intramolecular magnetic interactions only. This feature is particularly important because one can apply e.g. Nuclear Magnetic Resonance (NMR) techniques to investigate local properties of nanoscale individual objects, since the investigation of a

macroscopic quantity of material reproduces the properties of about 10^20 identical nanoscale entities [172]. Antiferromagnetic (AF) rings are wheel-shaped molecular magnets characterized by a number N of almost coplanar transition metal ions connected by means of bridging organic and inorganic ligands. Even number AF rings with N = 6, 8, 10, 12 and 18 are relatively common for transition metal ions composed by different spins e. g. Fe^{3+} ($s = 5/2$) [173, 174, 175, 176], Cr^{3+} ($s = 3/2$) [177], V^{3+} ($s = 1$) [178] and Cu^{2+} ($s = 1/2$) [179]. A common feature of all even number AF rings is to have a spin singlet $S_T = 0$ ground state due to the dominant antiferromagnetic Heisenberg exchange couplings between nearest neighbor spins. Due to the finite size effects, AF rings have a discrete energy spectrum and the lowest-lying excited states for the total spin S_T are known to be approximately given by the so-called Landes interval rule $E(S_T) = (2J/N)S_T(S_T + 1)$ where J is the antiferromagnetic exchange coupling constant [180].

The homometallic Cr^8 ring is formed by eight Cr^{3+} moments ($s = 3/2$) which display at low temperature a total $S_T = 0$ ground state with zero expectation value of the local spins [181]. When one Cr^{3+} ion is replaced by a diamagnetic ion (e.g. Cd^{2+}) or by a different magnetic ion (e.g. Ni^{2+} with $s = 1$) the ground state becomes magnetic and there is a redistribution of the local spin density which can be calculated theoretically. In a previous work we have measured the ^{53}Cr-NMR in Cr_7Cd and have determined unambiguously the local spin density in the ring with excellent agreement with the theory [182]. Somewhat surprisingly the local spin density in the ground state turned out to be rather uniformly distributed over the ring with the alternated staggered orientation due to the AF coupling when the Heisenberg interaction between nearest-neighbours magnetic centers on the polymetallic wheel is interrupted by the $s = 0$ Cd^{2+} ion. Thus it appears of interest to investigate how the single Cr^{3+} ion spin moment is distributed in an heterometallic ring where one Cr^{3+} ion is replaced by a different magnetic ion rather than a diamagnetic one. In this work we present the investigation of Cr_7Ni heterometallic ring. During the last years it has been shown that Cr_7Ni is a very promising system to encode a qubit [183]. Indeed, it behaves as an effective spin-1/2 at low T and can be manipulated in times much shorter than the measured decoherence time [184]. These molecular rings can be linked to each other either directly or through magnetic ions to form dimers: the resulting inter-ring magnetic coupling is sizeable and can be tuned by choosing the linker [185].

The site dependence of the local spin density plays a key role in the scheme proposed for obtaining time dependent qubit-qubit couplings in the presence of permanent exchange interactions [183]. We have succeeded in observing ^{53}Cr-NMR signals in Cr_7Ni in its $S = 1/2$ ground state, which gives a determination of the local spin density of each Cr^{3+} ion. However, due to intrinsic difficulties of the ^{53}Cr-NMR measurement (low gyromagnetic ratio and low senstivity), only one out of the three expected ^{53}Cr-NMR signals was detected down to 100 mK while the ^{61}Ni signal is too weak to be detected at any temperature. Nevertheless, the distribution of the local spin moments could be calculated theoretically

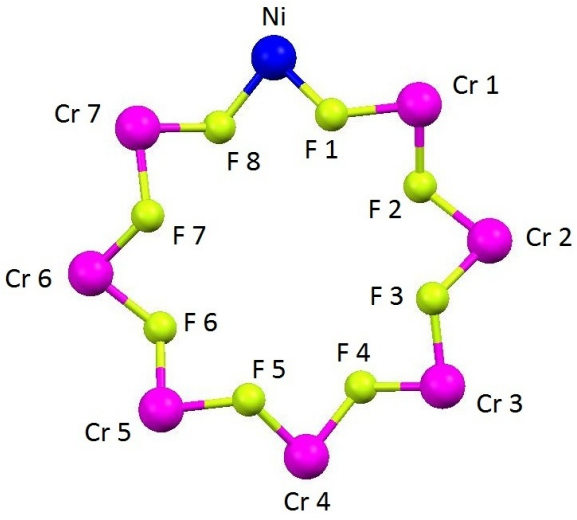

Figure 4.16 – Schematic representation of the Cr_7Ni heterometallic ring. Only the Cr^{3+} magnetic ions and the F^- bridging ligands are shown for simplicity.

as a function of the external magnetic field at low temperature and we could prove that the observed ^{53}Cr-NMR spectrum arises from three almost equivalent ^{53}Cr nuclei in the ring and the comparison with the theoretical results gave an excellent agreement by assuming a core polarization hyperfine field slightly smaller than the one observed in Cr_7Cd. This result gives total confidence about the theoretical calculations which show that the redistribution of the local spin density in the heterosubstituted Cr_7Ni ring is similar to the one observed in the heterometallic Cr_7Cd ring where the heterocenter is diamagnetic.

Experimental results and discussion

$(CH_3)_2NH_2[Cr_7NiF_8Piv_{16}]$ where Piv = $(CH_3)_3CCOO^-$ is the pivalate ion, Cr_7Ni in short, is an heterometallic AF ring constituted by eight transition metal ions connected by means of pivalate bridging ligands and fluoride bridging ions. Several single crystals were prepared as described in Ref. [186]. The ground state is magnetic with total spin $S_T = 1/2$. The zero-field energy gap between the ground state $S_T = 1/2$ and the first excited state $S_T = 3/2$ multiplets is about 13.7 K [187]. The intra-ring antiferromagnetic nearest neighbors exchange constants are J(Cr^{3+} - Cr^{3+}) = 16.9 K and J(Cr^{3+} - Ni^{2+}) = 19.6 K [188].

The ^{53}Cr-NMR spectrum was collected at 1.6 K with a pulsed homemade high power NMR spectrometer. Since the NMR line is very broad the spectrum is constructed point by point by integrating the whole Hahn (90° – 180°) echo while the external field is being swept at the fixed Larmor frequency ?L. Several attempts to detect the two missing ^{53}Cr-NMR signals were performed also by using a dilution refrigerator down to about 100 mK. The expected gain in sensitivity by lowering the temperature is unfortunately offset by a slight reduction of the sensitivity of the NMR probe in the dilution refrigerator set-up. Typical

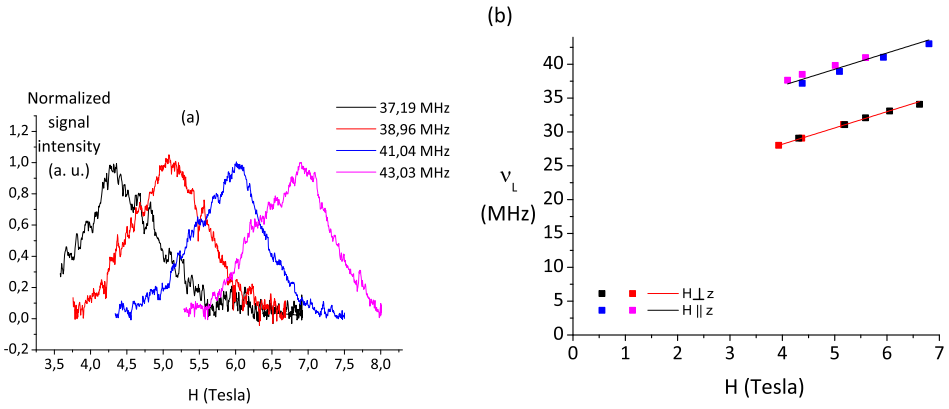

Figure 4.17 – (a) Representative ^{53}Cr-NMR spectra at 1.6 K obtained by sweeping the magnetic field at constant frequency. The field is applied perpendicular to the ring's plane. (b) Plot of the resonance frequency vs. magnetic field at the center of the NMR line. We plot the data for two orientations of the magnetic field with respect to the plane of the ring. The straight lines are the best fits used to determine the slope of the curve.

^{53}Cr-NMR spectra measured at several resonance frequencies and by applying the magnetic field perpendicular to the plane of the ring (H $\parallel$ z-axis) are shown in Fig. 4.17(a). With increasing resonance frequency the peak position in the spectrum shifts to higher magnetic field. In Fig. 4.17(b) the resonance frequency is plotted as a function of the peak position in terms of magnetic field given by a Lorentzian fit of the experimental peak. This figure reports the data collected by applying the magnetic field perpendicular to the plane of the ring (H $\parallel$ z-axis) and parallel to the plane of the ring (H $\perp$ z-axis). Different data sets are shown, corresponding to different experimental runs. The data for both orientations show a linear behavior with slope given by the gyromagnetic ratio of the ^{53}Cr nuclear isotope (9.54% abundance) i.e. $\gamma/2\pi = 2.406$ MHz/T.

The NMR line is very broad and the width slightly increases with increasing magnetic field (Fig. 4.17(a)). We measure the central line transition ($I_z = +1/2 \leftrightarrow -1/2$) of the ^{53}Cr ($I = 3/2$) NMR spectrum which is shifted only in second order by the quadrupolar interaction, whereby the shift is inversely proportional to the applied magnetic field [189]. Thus second order quadrupole broadening would be inversely proportional to the applied field. The observed slight increase of the NMR width in Fig.2(a) indicates that a magnetic rather than quadrupole broadening mechanism is dominant at high magnetic fields. The magnetic broadening mechanism is most likely due to non negligible contributions from the anisotropic hyperfine fields at the nuclear sites which can be different for the different ^{53}Cr sites in the ring and for different rings in the crystal. It is also possible that the broadening of the lines is due to a mosaic spread of our single crystals, often present in nanomagnets.

The NMR signal at 1.6 K can be observed only at high fields. In fact, at low temperatures Cr_7Ni behaves as an effective spin $S = 1/2$ and if a high external field is applied along the z axis only one level of the doublet $|S = 1/2, M = \pm 1/2\rangle$ is thermally populated [190]. Thus, low temperatures

and high fields are required to stabilize the local spin configuration and to observe the NMR signal in the magnetic ground state [182, 191]. The ^{53}Cr-NMR frequency is expected to be proportional to the vector sum of the external magnetic field H and the internal field due to the hyperfine interaction. By considering the case of the internal field being parallel (or antiparallel) to the external field and by considering only the dominant isotropic core polarization hyperfine contact term A one can write:

$$\nu_L = \frac{\gamma}{2\pi}(H + g\,\langle s\rangle\, A) \tag{4.6}$$

where γ is the ^{53}Cr nuclear gyromagnetic ratio, g is the Cr^{3+} Landé factor and $\langle s\rangle$ is the local expectation value of the Cr^{3+} electronic moment. If $\langle s\rangle$ is field independent, Eq.4.6 predicts the linear H dependence of the resonance frequency observed in Fig. 4.17(b). In order to compare the experimental data to the local spin density in the ring we turn now to the theoretical calculation of the local spin density $\langle s\rangle$ in the ground state of the ring. Low-temperature properties of the Cr_7Ni AF ring can be described by the following spin Hamiltonian:

$$\begin{aligned}\mathcal{H} \;=\; & \sum_{i=1}^{N} J_{i,i+1}\mathbf{s}_i\cdot\mathbf{s}_{i+1} + \sum_{i=1}^{N} d_i\left[s_{z,i}^2 - \frac{1}{3}s_i(s_i+1)\right] + \\ & + \sum_{i>j=1}^{N} D_{ij}\left[2s_{z,i}s_{z,j} - s_{x,i}s_{x,j} - s_{y,i}s_{y,j}\right] - \mu_B\sum_{i=1}^{N} g_i\mathbf{H}\cdot\mathbf{s}_i\end{aligned} \tag{4.7}$$

where $\mathbf{s}_i$ is the spin operator of the i-th magnetic ion ($s_i = 3/2$ for Cr^{3+} ions and $s_i = 1$ for the Ni^{2+} ion). The first term represents the Heisenberg nearest-neighbors exchange interaction, with the usual cyclic boundary condition $N + 1 = 1$, being N the number of ions in the molecule (here $N = 8$). The second term accounts for uniaxial local crystal fields (being z the axis perpendicular to the plane of the ring) and the third term is the axial contribution to the dipolar anisotropic intracluster spin-spin interaction, where Dij is evaluated within the point-dipole approximation. The last term is the Zeeman coupling to an external field. The parameters of the above Hamiltonian were determined by means of inelastic neutron scattering and thermodynamic measurements [192, 188, 193].

In AF rings the dimension of the spin Hilbert space is large (e.g., 49152 for Cr_7Ni). Thus, in order to diagonalize the Hamiltonian in Eq.4.7, we have followed a two-steps procedure [194]. The Heisenberg interaction represents the dominant contribution to the spin Hamiltonian and its energy spectrum consists of a series of level multiplets with a definite value of $|\mathbf{S}|$. In the first step of the diagonalization procedure only the first term in Eq.4.7 has been considered. By exploiting the rotational invariance of the Heisenberg term, the Heisenberg Hamiltonian matrix has been block factorized according to the total spin quantum number S and the corresponding eigenvalues and eigenvectors have been

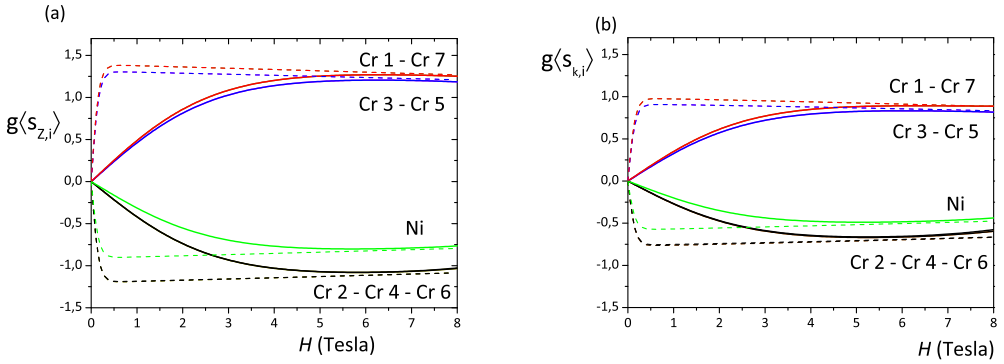

Figure 4.18 – Theoretical results regarding the local spin density in Cr_7Ni heterometallic ring at $T = 1.6$ K (solid lines) and at $T = 0.1$ K (dashed lines) obtained by assuming in the Hamiltonian Eq.4.7 the following parameters: J(Cr–Cr) = 16.9 K, J(Cr–Ni = 19.6 K, $d_{Cr} = -0.35$ K and $d_{Ni} = -4$ K. The numbering of the sites is shown in Fig. 4.16. Fig. 3(a) shows the local spin values in the case of the magnetic field oriented perpendicular to the plane of the ring while Fig. 3(b) refers to the case of the applied field oriented parallel to the plane of the ring.

calculated. However, the anisotropic terms in Eq.4.7 do not commute with the total squared spin operator S^2 and mix different total spin subspaces (S mixing) [195]. To obtain the total energy spectrum, the complete Hamiltonian in Eq.4.7 has been diagonalized using the two-steps perturbative technique described in Ref. [194]. Our calculations show that the reduction to the subspace spanned by the lowest spin exchange manifolds (up to 150 K) allows us to reproduce properly the low-temperature properties, reducing the computational effort. The calculated eigenstates and eigenvalues of the Hamiltonian in Eq.(1) have been used to evaluate the magnetic field dependence of the thermal averages of the local spin operators $s_{\alpha,i}$ ($\alpha = x, y, z$): (3)

$$\langle s_{\alpha,i} \rangle = \frac{1}{Z} \sum_{j=1}^{n} \langle j \, | s_{\alpha,i} | \, j \rangle \, e^{-\beta E_j(\mathbf{H})} \tag{4.8}$$

where the index i labels the Cr^{3+} (and Ni^{2+}) sites and the sum runs over the eigenstates and eigenvalues which depend on the applied field $\mathbf{H}$. If the magnetic field is applied along the z-axis perpendicular to the ring's plane ($\theta = 0$) only $\langle s_{z,i} \rangle \neq 0$ while if the magnetic field is applied parallel to the ring's plane ($\theta = \pi/2$) only $\langle s_{k,i} \rangle \neq 0$, where k denotes the magnetic field in-plane direction.

The theoretical calculations are summarized in Fig.4.18. The decrease of the local spin density at 1.6 K for fields below about 4 Tesla is due to the reduction of the Zeeman splitting and to the consequent increasing population of the higher-energy level of the $S = 1/2$ doublet ($|S = 1/2, M = -1/2\rangle$). The results at $T = 0.1$ K (see dashed lines in Fig.4.18) show a nearly constant $\langle s \rangle$ value down to low fields. From the inspection of Eq.4.6 and of the experimental data in Fig. 4.17 it is clear that the observed ^{53}Cr-NMR signal must be ascribed to the nuclear sites 2, 4, 6 of Fig.4.16. In fact the core polarization field is opposite

	$H \perp z$	$H \parallel z$
Cr 1	0,88	1,25
Cr 2	-0,67	-1,07
Cr 3	0,82	1,19
Cr 4	-0,66	-1,07
Cr 5	0,82	1,19
Cr 6	-0,67	-1,07
Cr 7	0,88	1,25
Ni	-0,49	-0,80

Table 4.4 – Theoretical electronic magnetic moment expectation values in Cr_7Ni at T = 1.6 K and $H = 5$ Tesla corresponding to Figure 3. The values listed are the electronic magnetic moments expressed in Bohr magnetons ($g = 1.98$ for the Cr^{3+} ions and $g = 2.2$ for the Ni^{2+} ion).

to the local spin direction (A is negative in Eq.4.6). Thus since the local field of the observed NMR line adds to the external field (Fig.4.17b) it must arise from a negative (i.e. opposite to **H**) $g\langle s\rangle$ value in Fig.4.18. Note that in the present convention $g\langle s\rangle$ (not $-g\langle s\rangle$) is the magnetic moment in Bohr magnetons (see Eq. 4.7).

The electronic magnetic moments $g\langle s\rangle$ expressed in Bohr magnetons at $T = 1.6$ K are reported in Table 1 for the case of magnetic field applied parallel and perpendicular to the molecular ring plane. The orientation-dependence of the local spin moment for each Cr^{3+} ion originates from single-ion and dipolar anisotropies (d and D_{ij} terms in the Hamiltonian) and reflects the mixing between different total spin multiplets (S mixing) [195]. Indeed, in the lack of S mixing the ground doublet of Cr_7Ni would be exactly isotropic. The anisotropy of each single Cr^{3+} (or Ni^{2+}) spin is found to be sizeable and of easy-axis type (see Table 4.4). It is worthwhile observing that this anisotropy does not lead to an anisotropy barrier hampering the reversal of the molecular magnetization at low temperatures, like e.g. in molecular nanomagnets such as Mn_{12} and Fe_8 [23].

In Fig.4.19 we have plotted the experimental results for the two orientations of the magnetic field by including the data obtained on different samples and in different runs. We also show the theoretical curves obtained by using Eq.4.6 (at two different temperatures) and the theoretical values of $\langle s\rangle$ in Fig.4.18. The only fitting parameter is the core polarization constant A. By choosing A = -11 T the agreement is very satisfactory for both field orientations.

The value of the core polarization field A = -11 Tesla / μ_B obtained for ^{53}Cr in Cr_7Ni can be compared to the one obtained in Cr_7Cd (i.e. $A = -11.05$ Tesla $/\mu_B$) by fitting the data of Ref. [182], in the case of the field being applied perpendicular to the plane of the ring , in the same way as done here. The two values are practically identical in agreement with the notion that the 3d wavefunction of the Cr^{3+} ion is not affected by the heterometallic substitution. It should be noticed that a higher value (i.e. $A = -12.38$ Tesla $/\mu_B$) was obtained [182] in Cr_7Cd directly from the NMR data without using the theoretical

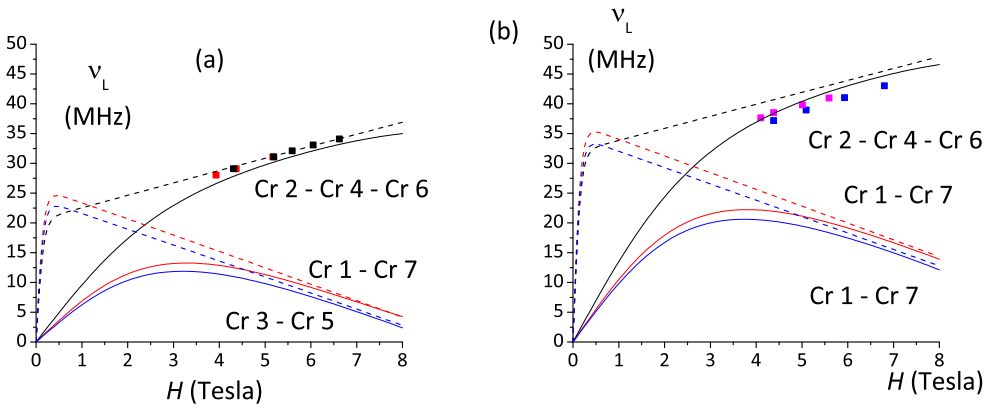

Figure 4.19 – ^{53}Cr-NMR of a Cr_7Ni single crystal at $T = 1.6$ K: resonance frequency vs. applied magnetic field. (a) The magnetic field is applied perpendicular to the crystallographic z-axis, namely parallel to the plane of the ring. (b) The magnetic field is applied parallel to the crystallographic z-axis, namely perpendicular to the plane of the ring. The solid lines show the theoretical predictions at $T = 1.6$ K obtained by using Eq.4.6 with $A = -11$ Tesla and the $g\langle s\rangle$ calculated in Fig.4.18. The dashed lines represent the theoretical predictions at $T = 0.1$ K.

results for the $\langle s\rangle$ distribution in the ring. This higher value is very close to the estimated theoretical value for a 3d core polarization field in the isolated Cr atom i.e. $A = -12.5$ Tesla/μ_B [196, 189]. We suggest that the smaller value (i. e. $A = -11.05$ Tesla) obtained by using the theoretically calculated spin densities is an indication of a slight delocalization of the 3d wavefunction of the Cr^{3+} ion in the ring.

By comparing the results for Cr 2, 4, 6 sites in the two different orientations of the magnetic field in Fig. 4.19, it is also possible to experimentally confirm the easy-axis anisotropy for the local spin moments of Cr^{3+}, predicted by theoretical calculations (Table 4.4). In fact, the ^{53}Cr-NMR frequency is higher when the magnetic field is applied parallel to the crystallographic z-axis, due to the larger absolute value of the local spin density (see Eq.4.6).

From the inspection of Fig.4.19 it is also clear that the signals due to sites 1, 7, 3, 5 (see Fig.4.16) are difficult to be detected at $T = 1.6$ K since the expected resonance frequency is low in the whole magnetic field range. At very low temperature, where the spin density $\langle s\rangle$ remains constant down to low values of H, the expected resonance frequency would be higher (see dashed lines in Fig.4.19). We did try to detect the signals at $T = 100$ mK by using a dilution refrigerator but the radiofrequency probe head had not sufficient sensitivity. Furthermore it would be interesting to be able to follow the NMR signal at low fields where the $\langle s\rangle$ values decrease due to the thermal population of the first excited level. Unfortunately, thermal fluctuations are likely to decrease the nuclear spin lattice, T_1, and spin-spin, T_2, relaxation times making the signal too broad to be observed. Also, second order quadrupole effects may shift and broaden the signal at low magnetic fields [189].

In conclusion we have shown that the ^{53}Cr-NMR signal observed at high

magnetic field values and at $T = 1.6$ K in Cr_7Ni is in excellent agreement with the local spin density distribution calculated theoretically. The core polarization hyperfine constant turns out to be almost the same in Cr_7Cd and in Cr_7Ni indicating that the heterometallic substitution in the Cr^8 ring does not affect the local 3d wavefunction at the Cr^{3+} site. The main result appears to be the fact that the local spin density redistribution in the heterometallic rings is rather uniform for both the diamagnetic substitution (i.e. Cr_7Cd) and the magnetic substitution (i.e. Cr_7Ni). However, although we have similar staggered spin moments distributions for both cases, the absolute values of the spin moments are different. In the case of Cd7Cd the spin moments of Cr^{3+} ions are slightly smaller ($\sim 2\mu_B$) than $3\mu_B$ which is the value expected for Cr^{3+} isolated ions[182]. On the other hand, for Cr_7Ni each Cr^{3+} spin moment is much smaller ($\sim \mu_B$) than $3\mu_B$. This indicates that the full disconnection of the magnetic interaction due to a magnetic ion leads to a larger perturbation that destroys the spin singlet coherent state of the mother material, i. e. Cr^8, with $S = 0$ ground state characterized by local $\langle s \rangle = 0$ values.

Acknowledgements

Ames Laboratory is operated for U.S. Department of Energy by Iowa State University under Contract No. DE-AC02-07CH11358. This work at Ames Laboratory was supported by the Office of Basic Energy Science. One of us (L.B.) thanks CNISM for travel fundings to perform experiments in Ames. PRIN Italian project no. 2008PARRTS_001 by MIUR is thanked for partly funding the present research.

Authors

Publications

L. Bordonali, Y. Furukawa, C. Sangregorio, M.F. Casula, and A. Lascialfari
^{1}H-*NMR study of the spin dynamics of fine superparamagnetic nanoparticles*, Physical Review B, 85, 174426 (2012).

M. Casadei, **L. Bordonali**, Y. Furukawa, F. Borsa, E. Garlatti, A. Lascialfari, S. Carretta, S. Sanna, G. Timco, R. Winpenny
Redistribution of local spin density in Cr_7Ni *antiferromagnetic molecular ring from* ^{53}Cr-*NMR*, J. Phys.: Condens. Matter, 24, 406002 (2012).

L. Bordonali, T. Kalaivani, K. P. V. Sabareesh, Y. Guari, M. F. Casula, C. Sangregorio, C. Innocenti and A. Lascialfari
Dependence of nuclear relaxation rates on magnetic core size in monodispersed nanoparticles, J. Phys.: Condens. Matter, 25, 066008 (2012).

P. Arosio, J. Thévenot, T. Orlando, F. Orsini, M. Corti, M. Mariani, **L. Bordonali**, C. Innocenti, C. Sangregorio, H. Oliveira, S. Lecommandoux, A. Lascialfari, O. Sandre
Hybrid Iron Oxide-Copolymer Micelles and Vesicles as Contrast Agents for MRI: Impact of the Nanostructure on the Relaxometric Properties, accepted by J. Mat. Chem. B, to be published.

C. Casadei, E. Garlatti, **L. Bordonali**, Y. Furukawa, F. Borsa, A. Lascialfari, G.Timco, R.Winpenny
Magnetic properties and hyperfine interactions in Cr_8, Cr_7Cd *and* Cr_7Ni *molecular rings from* ^{19}F-*NMR*, in preparation.

L. Bordonali, Y. Furukawa, M. Mariani, K.P.V. Sabareesh, S. Carretta, G.Timco, R. Winpenny, A. Lascialfari, F. Borsa
Low temperature spin dynamics in Cr_7Ni-*Cu*-Cr_7Ni *coupled molecular rings*, in preparation.

L. Bordonali, A. Lascialfari et. al.
Size dependent spin dynamics of coated maghemite nanoparticles: a ^{1}H-*NMR investigation.*, temporary title, in preparation.

F. Rossella, M.C. Mozzati, **L. Bordonali**, A. Lascialfari, C. Soldano, V. Bellani
Superspin glass-like ordering in metal-filled carbon nanotube arrays: towards novel magnetic metamaterials., in preparation, to be submitted.

Bibliography

[1] E. C. Stoner and E. P. Wohlfarth. *Philosophical Transactions of the Royal Society of London. Series A, Mathematical and Physical Sciences*, **240, 826** 599, 1948.

[2] G. Reiss and A. Htten. *Nature Materials*, **4, 10** 725, 2005.

[3] Z. Nie, A. Petukhova, and E. Kumacheva. *Nature Nanotechnology*, **5, 1** 15, 2010.

[4] J. L. Dormann, D. Fiorani, and E. Tronc. *Magnetic Relaxation in Fine-Particle Systems*, 283–494 (John Wiley & Sons, Inc.), 1997. ISBN 9780470141571.

[5] F. J. Himpsel, J. E. Ortega, G. J. Mankey, and R. F. Willis. *Advances in Physics*, **47, 4** 511, 1998.

[6] J. Frenkel and J. Doefman. *Nature*, **126** 274 , 1930.

[7] C. Kittel. *Phys. Rev.*, **70** 965, 1946.

[8] J.-P. Wang. *ChemInform*, **40, 24** no, 2009. ISSN 1522-2667.

[9] C. G. Montgomery. *Phys. Rev.*, **38** 1782, 1931.

[10] T. Jonsson, J. Mattsson, C. Djurberg, F. A. Khan, P. Nordblad, and P. Svedlindh. *Phys. Rev. Lett.*, **75** 4138, 1995.

[11] J. Dormann, R. Cherkaoui, L. Spinu, M. Nogus, F. Lucari, F. D'Orazio, D. Fiorani, A. Garcia, E. Tronc, and J. Jolivet. *Journal of Magnetism and Magnetic Materials*, **187, 2** L139 , 1998.

[12] H. Mamiya, I. Nakatani, and T. Furubayashi. *Phys. Rev. Lett.*, **82** 4332, 1999.

[13] D. Parker, V. Dupuis, F. Ladieu, J.-P. Bouchaud, E. Dubois, R. Perzynski, and E. Vincent. *Phys. Rev. B*, **77** 104428, 2008.

[14] H. Kachkachi, A. Ezzir, M. Nogues, and E. Tronc. *Eur. Phys. J. B*, **14, 4** 681, 2000. ISSN 1434-6028.

[15] T. N. Shendruk, R. D. Desautels, B. W. Southern, and J. van Lierop. *The effect of surface spin disorder on the magnetism of γ-Fe 2 O 3 nanoparticle dispersions*, 2007.

[16] M. P. Morales, S. Veintemillas-Verdaguer, M. I. Montero, C. J. Serna, A. Roig, L. Casas, B. Martínez, and F. Sandiumenge. *Chem. Mater.*, **11** 3058, 1999.

[17] S. Odenbach. *Journal of Physics: Condensed Matter*, **16, 32** R1135, 2004.

[18] M. W. Szyndler and R. M. Corn. *The Journal of Physical Chemistry Letters*, **3, 0** 2320, 2012.

[19] M. Marinescu, J. F. Liu, M. J. Bonder, and G. C. Hadjipanayis. *Journal of Applied Physics*, **103, 7** 07E120, 2008.

[20] M.-H. Phan and S.-C. Yu. *ChemInform*, **38, 8** no, 2007. ISSN 1522-2667.

[21] Q. Pankhurst, J. Connolly, S. Jones, and J. Dobson. *Journal of Physics D: Applied Physics*, **36, 13** R167, 2003. ISSN 0022-3727.

[22] Q. Pankhurst, N. Thanh, and S. Jones. *Journal of Physics D:*, **42, 22** 224001, 2009. ISSN 0022-3727.

[23] D. Gatteschi, R. Sessoli, and J. Villain. *Molecular Nanomagnets* (Oxford University Press), 2006.

[24] M. Fittipaldi, L. Sorace, A.-L. Barra, C. Sangregorio, R. Sessoli, and D. Gatteschi. *Phys. Chem. Chem. Phys.*, **11** 6555, 2009.

[25] B. Pilawa, R. Boffinger, I. Keilhauer, R. Leppin, I. Odenwald, W. Wendl, C. Berthier, and M. Horvatić. *Phys. Rev. B*, **71** 184419, 2005.

[26] Y. Furukawa, K. Kumagai, A. Lascialfari, S. Aldrovandi, F. Borsa, R. Sessoli, and D. Gatteschi. *Phys. Rev. B*, **64** 094439, 2001.

[27] Y. Furukawa, K. Aizawa, K.-I. Kumagai, A. Lascialfari, S. Aldrovandi, F. Borsa, R. Sessoli, and D. Gatteschi. *Mol. Cryst. Liq. Cryst.*, **379, 1** 191, 2003.

[28] M. Affronte, J.C. Lasjaunias, and A. Cornia. *Eur. Phys. J. B*, **15, 4** 633, 2000.

[29] E. Micotti, D. Procissi, A. Lascialfari, A. Carretta, P. Kgerler, F. Borsa, M. Luban, and C. Baines. *J. Magn. Magn. Mater.*, **272-276, Part 2** 1099 , 2004. ISSN 0304-8853.

[30] S. H. Baek, M. Luban, A. Lascialfari, E. Micotti, Y. Furukawa, F. Borsa, J. van Slageren, and A. Cornia. *Phys. Rev. B*, **70** 134434, 2004.

[31] D. Gatteschi, M. Fittipaldi, C. Sangregorio, and L. Sorace. *Angewandte Chemie International Edition*, **51, 20** 4792, 2012. ISSN 1521-3773.

[32] A. Roch, R. Muller, and P. Gillis. *The Journal of chemical physics*, **110, 11** 5403, 1999. ISSN 00219606.

[33] R. Massart. *IEEE Trans. Magn.*, **M, 2** 1980, 1981. ISSN 1558-2639.

[34] M. F. Casula, P. Floris, C. Innocenti, A. Lascialfari, M. Marinone, M. Corti, R. a. Sperling, W. J. Parak, and C. Sangregorio. *Chemistry of Materials*, **22, 5** 1739, 2010. ISSN 0897-4756.

[35] E. Umut, F. Pineider, P. Arosio, C. Sangregorio, M. Corti, F. Tabak, A. Lascialfari, and P. Ghigna. *Journal of Magnetism and Magnetic Materials*, **324, 15** 2373 , 2012. ISSN 0304-8853.

[36] H. Amiri, R. Bustamante, A. Milln, N. J. Silva, R. Piol, L. Gabilondo, F. Palacio, P. Arosio, M. Corti, and A. Lascialfari. *Magn. Reson. Med.*, **66** 1715, 2011.

[37] A. H. Morrish. *The Physical Principles of Magnetism* (Wiley-IEEE Press), 2001.

[38] C.-R. Lin, Y.-M. Chu, and S.-C. Wang. *Materials Letters*, **60, 4** 447 , 2006. ISSN 0167-577X.

[39] O. Iglesias and A. Labarta. *Phys. Rev. B*, **63** 184416, 2001.

[40] P. V. Hendriksen, S. Linderoth, and P.-A. Lindgård. *Phys. Rev. B*, **48** 7259, 1993.

[41] F. Liu, M. R. Press, S. N. Khanna, and P. Jena. *Phys. Rev. B*, **39** 6914, 1989.

[42] X. Batlle and A. Labarta. *Journal of Physics D: Applied Physics*, **35** R15, 2002.

[43] M. Hansen and S. Mrup. *Journal of Magnetism and Magnetic Materials*, **203, 13** 214 , 1999. ISSN 0304-8853.

[44] O. Iglesias and A. Labarta. *Phys. Rev. B*, **70** 144401, 2004.

[45] F. Tournus and E. Bonet. *Journal of Magnetism and Magnetic Materials*, **323, 9** 1109 , 2011. ISSN 0304-8853.

[46] D. Serantes, D. Baldomir, M. Pereiro, J. Arias, C. Mateomateo, M. Bujannunez, C. Vazquezvazquez, and J. Rivas. *Journal of Non-Crystalline Solids*, **354, 47-51** 5224, 2008. ISSN 00223093.

[47] O. Iglesias and A. Labarta. *Journal of Applied Physics*, **91, 7** 4409, 2002. ISSN 00218979.

[48] J. Dormann, L. Bessais, and D. Fiorani. *Journal of Physics C: Solid State Physics*, **21** 2015, 1988.

[49] B. Martínez, X. Obradors, L. Balcells, A. Rouanet, and C. Monty. *Phys. Rev. Lett.*, **80, 1** 181, 1998.

[50] G. F. Goya and M. P. Morales. *J. Metastable Nanocryst. Mater.*, **20** 673, 2004. ISSN 1422-6375.

[51] J. R. L. de Almeida and D. J. Thouless. *Journal of Physics A: Mathematical and General*, **11, 5** 983, 1978.

[52] J. Myrdosh. *Spin Glasses: An Experimental Introduction* (CRC Press), 1993.

[53] L. E. Wenger and J. A. Mydosh. *Phys. Rev. B*, **29** 4156, 1984.

[54] S. Mørup. *EPL (Europhysics Letters)*, **28, 9** 671, 1994.

[55] W. Luo, S. R. Nagel, T. F. Rosenbaum, and R. E. Rosensweig. *Phys. Rev. Lett.*, **67** 2721, 1991.

[56] N. Mikuszeit, E. Y. Vedmedenko, and E. Y. xOepen. *Journal of Physics: Condensed Matter*, **16, 49** 9037, 2004.

[57] E. Leite, J. Coaquira, W. Viali, P. Sartoratto, R. Almeida, P. Morais, and S. Malik. In *Journal of Physics: Conference Series*, volume 200, 072060 (IOP Publishing), 2010.

[58] C. Djurberg, P. Svedlindh, P. Nordblad, M. Hansen, F. Bø dker, and S. Mø rup. *Physical review letters*, **79, 25** 5154, 1997. ISSN 0031-9007.

[59] S. Sahoo, O. Petracic, W. Kleemann, P. Nordblad, S. Cardoso, and P. P. Freitas. *Phys. Rev. B*, **67** 214422, 2003.

[60] M. Sasaki, P. E. Jönsson, H. Takayama, and H. Mamiya. *Phys. Rev. B*, **71** 104405, 2005.

[61] N. Pérez, P. Guardia, a. G. Roca, M. P. Morales, C. J. Serna, O. Iglesias, F. Bartolomé, L. M. García, X. Batlle, and A. Labarta. *Nanotechnology*, **19, 47** 475704, 2008. ISSN 0957-4484.

[62] M. Hansen. *Beilstein Journal of*, **1** 182, 2010. ISSN 2190-4286.

[63] D. Petit, L. Fruchter, and I. A. Campbell. *Phys. Rev. Lett.*, **88** 207206, 2002.

[64] P. Jönsson, S. Felton, P. Svedlindh, P. Nordblad, and M. Hansen. *Physical Review B*, **64, 21** 212402, 2001. ISSN 0163-1829.

[65] S. Mørup, M. Hansen, and C. Frandsen. In D. L. Andrews, G. D. Scholes, and G. P. Wiederrecht, editors, *Comprehensive Nanoscience and Technology*, 437 – 491 (Academic Press, Amsterdam), 2011. ISBN 978-0-12-374396-1.

[66] R. S. de Biasi and T. C. Devezas. *Journal of Applied Physics*, **49, 4** 2466, 1978.

[67] E. de Biasi, C. Ramos, and R. Zysler. *Journal of Magnetism and Magnetic Materials*, **262, 2** 235 , 2003. ISSN 0304-8853.

[68] N. Noginova, T. Weaver, M. King, A. Bourlinos, E. Giannelis, and V. Atsarkin. *J. Phys.: Condens. Matter.*, **19, 7** 076210, 2007. ISSN 0953-8984.

[69] C. Mitsumata, S. Tomita, M. Hagiwara, and K. Akamatsu. *Journal of Physics: Condensed Matter*, **22, 1** 016005, 2010. ISSN 0953-8984.

[70] F. Gazeau, J. Bacri, F. Gendron, R. Perzynski, Y. Raikher, V. Stepanov, and E. Dubois. *Journal of Magnetism and Magnetic Materials*, **186, 12** 175 , 1998. ISSN 0304-8853.

[71] M. Vasilakaki and K. N. Trohidou. *Journal of Physics D: Applied Physics*, **41, 13** 134006, 2008.

[72] N. Noginova, T. Weaver, E. Giannelis, A. Bourlinos, V. Atsarkin, and V. Demidov. *Physical Review B*, **77, 1** 014403, 2008. ISSN 1098-0121.

[73] M. Noginov, N. Noginova, O. Amponsah, R. Bah, R. Rakhimov, and V. Atsarkin. *J. Magn. Magn. Mater.*, **320, 18** 2228, 2008. ISSN 03048853.

[74] M. Fittipaldi, C. Innocenti, P. Ceci, C. Sangregorio, L. Castelli, L. Sorace, and D. Gatteschi. *Phys. Rev. B*, **83, 10** 104409, 2011. ISSN 1098-0121.

[75] A. M. Portis and R. H. Lindquist. In G. T. Rado and S. Suhl, editors, *Magnetism IIA* (Academic, New York), 1965.

[76] E. Turov and M. Petrov. *Nuclear magnetic resonance in ferro-and antiferromagnets* (Israel Program for Scientific Translations), 1972. ISBN 9780706511055.

[77] A. C. Gossard, A. M. Portis, M. Rubinstein, and R. H. Lindquist. *Phys. Rev.*, **138** A1415, 1965.

[78] H. Yasuoka and R. T. Lewis. *Phys. Rev.*, **183** 559, 1969.

[79] V. Scarani, H. D. Riedmatten, and J.-P. Ansermet. *Applied Physics Letters*, **76, 7** 903, 2000.

[80] M. Shiraishi, H. Kusai, R. Nouchi, T. Nozaki, T. Shinjo, Y. Suzuki, M. Yoshida, and M. Takigawa. *Applied Physics Letters*, **93, 5** 053103, 2008.

[81] S. Ogawa and S. Morimoto. *Journal of the Physical Society of Japan*, **16, 10** 2065, 1961.

[82] J. H. Shim, S. Lee, J. H. Park, S.-J. Han, Y. H. Jeong, and Y. W. Cho. *Phys. Rev. B*, **73** 064404, 2006.

[83] H. Stepankova, K. Kouril, V. Chlan, P. Görnert, R. Müller, and J. Stepanek. *Journal of Magnetism and Magnetic Materials*, **322, 912** 1323 , 2010. ISSN 0304-8853. ¡ce:title¿Proceedings of the Joint European Magnetic Symposia¡/ce:title¿.

[84] A. C. Gossard and A. M. Portis. *Phys. Rev. Lett.*, **3** 164, 1959.

[85] E. L. Boyd. *Phys. Rev.*, **129** 1961, 1963.

[86] T. Mizoguchi and M. Inoue. *Journal of the Physical Society of Japan*, **21, 7** 1310, 1966.

[87] M. Mizoguchi. *Journal of the Physical Society of Japan*, **44, 5** 1501, 1978.

[88] P. Novák, H. Štěpánková, J. Englich, J. Kohout, and V. A. M. Brabers. *Phys. Rev. B*, **61** 1256, 2000.

[89] M. Matsuura, H. Yasuoka, A. Hirai, and T. Hashi. *Journal of the Physical Society of Japan*, **17, 7** 1147, 1962.

[90] A. Hirai, J. A. Eaton, and C. W. Searle. *Phys. Rev. B*, **3** 68, 1971.

[91] S.-J. Lee, H. Jung, S. Lee, and J. Dho. *New Journal of Physics*, **11, 2** 023020, 2009.

[92] S. Ogawa and S. Morimoto. *Journal of the Physical Society of Japan*, **17, 4** 654, 1962.

[93] J. H. Shim, S. Lee, and B. I. Min. *Phys. Rev. B*, **75** 134406, 2007.

[94] S.-J. Lee and S. Lee. *New Journal of Physics*, **8, 6** 98, 2006.

[95] T. Bastow and A. Trinchi. *Solid State Nuclear Magnetic Resonance*, **35, 1** 25 , 2009. ISSN 0926-2040.

[96] T. Bastow, A. Trinchi, M. Hill, R. Harris, and T. Muster. *Journal of Magnetism and Magnetic Materials*, **321, 17** 2677 , 2009. ISSN 0304-8853.

[97] T. Daou, J. Greneche, and S. Lee. *J. Phys. Chem. C*, 8794–8799, 2010.

[98] M. Fardis, a. P. Douvalis, D. Tsitrouli, I. Rabias, D. Stamopoulos, T. Kehagias, E. Karakosta, G. Diamantopoulos, T. Bakas, and G. Papavassiliou. *Journal of physics. Condensed matter : an Institute of Physics journal*, **24, 15** 156001, 2012. ISSN 1361-648X.

[99] E. Tronc, D. Fiorani, M. Noguès, A. M. Testa, F. Lucari, F. D'Orazio, J. Grenèche, W. Wernsdorfer, N. Galvez, and C. Chanéac. *J. Magn. Magn. Mater.*, **262, 1** 6, 2003. ISSN 03048853.

[100] D. Fiorani. *Surface Effects in Magnetic Nanoparticles*. Nanostructure Science and Technology (Springer), 2011. ISBN 9781441935977.

[101] R. J. Abraham, editor. *Nuclear Magnetic Resonance*, volume 8 of *SPR - Nuclear Magnetic Resonance* (The Royal Society of Chemistry), 1979. ISBN 978-0-85186-322-1.

[102] T. Moriya. *Progress of Theoretical Physics*, **16, 1** 23, 1956.

[103] C. P. Slichter. *Principles of Magnetic Resonance (Springer Series in Solid-State Sciences)* (Springer Verlag GmbH), 1996.

[104] P. Jnsson, M. Hansen, P. Svedlindh, and P. Nordblad. *Journal of Magnetism and Magnetic Materials*, **226230, Part 2, 0** 1315 , 2001. ISSN 0304-8853. ¡ce:title¿Proceedings of the International Conference on Magnetism (ICM 2000)¡/ce:title¿.

[105] G. Goya, T. Berquo, F. Fonseca, and M. Morales. *J. Appl. Phys.*, **94, 5** 3520, 2003.

[106] G. Goya, S. L. Gomez, and S. M. Shibli. *Journal of Metastable and*, **22** 33, 2004.

[107] F. Bødker, M. F. Hansen, C. B. Koch, K. Lefmann, and S. Mørup. *Phys. Rev. B*, **61** 6826, 2000.

[108] S. Chakraverty, M. Bandyopadhyay, S. Chatterjee, S. Dattagupta, A. Frydman, S. Sengupta, and P. A. Sreeram. *Phys. Rev. B*, **71** 054401, 2005.

[109] L. Rebbouh, R. P. Hermann, F. Grandjean, T. Hyeon, K. An, A. Amato, and G. J. Long. *Phys. Rev. B*, **76** 174422, 2007.

[110] P. P. Vaishnava, U. Senaratne, E. C. Buc, R. Naik, V. M. Naik, G. M. Tsoi, and L. E. Wenger. *Phys. Rev. B*, **76** 024413, 2007.

[111] M. F. Hansen, C. B. Koch, and S. Mørup. *Phys. Rev. B*, **62** 1124, 2000.

[112] C. Frandsen and S. Mørup. *Phys. Rev. Lett.*, **94** 027202, 2005.

[113] G. C. Papaefthymiou, E. Devlin, A. Simopoulos, D. K. Yi, S. N. Riduan, S. S. Lee, and J. Y. Ying. *Phys. Rev. B*, **80** 024406, 2009.

[114] F. Bødker, S. Mørup, and S. Linderoth. *Phys. Rev. Lett.*, **72** 282, 1994.

[115] C. R. Alves, R. Aquino, J. Depeyrot, T. A. P. Cotta, M. H. Sousa, F. A. Tourinho, H. R. Rechenberg, and G. F. Goya. *Journal of Applied Physics*, **99, 8** 08M905, 2006.

[116] E. C. Sousa, H. R. Rechenberg, J. Depeyrot, J. A. Gomes, R. Aquino, F. A. Tourinho, V. Dupuis, and R. Perzynski. *Journal of Applied Physics*, **106, 9** 093901, 2009.

[117] D. H. Jones and K. K. P. Srivastava. *Physical Review B*, **34, 11**, 1986.

[118] M. A. Chuev. *Journal of physics. Condensed matter : an Institute of Physics journal*, **23, 42** 426003, 2011. ISSN 1361-648X.

[119] A. G. Roca, D. Niznansky, J. Poltierova-Vejpravova, B. Bittova, M. A. González-Fernández, C. J. Serna, and M. P. Morales. *Journal of Applied Physics*, **105, 11** 114309, 2009.

[120] NanoCon 2001. *Spin canting of γ-Fe_2O_3 nanoparticles and its evaluation employing a statistical approach*, 2011.

[121] A. Roch, P. Gillis, A. Ouakssim, and R. Muller. *Journal of magnetism and magnetic materials*, **201, 1-3** 77, 1999. ISSN 03048853.

[122] J. Cheon and J.-H. Lee. *Accounts of Chemical Research*, **41, 12** 1630, 2008.

[123] U. Pison, B. Paulke, S. Pietschmann, L. Kaufner, H. Bruhn, R. Cartier, and S. Schumacher. In O. Dssel and W. Schlegel, editors, *World Congress on Medical Physics and Biomedical Engineering, September 7 - 12, 2009, Munich, Germany*, volume 25/2 of *IFMBE Proceedings*, 931–931 (Springer Berlin Heidelberg), 2009. ISBN 978-3-642-03878-5.

[124] D.-E. Lee, H. Koo, I.-C. Sun, J. H. Ryu, K. Kim, and I. C. Kwon. *Chem. Soc. Rev.*, **41** 2656, 2012.

[125] P. Cherukuri, E. S. Glazer, and S. A. Curley. *Advanced Drug Delivery Reviews*, **62, 3** 339 , 2010. ISSN 0169-409X. ¡ce:title¿Targeted Delivery Using Inorganic Nanosystem¡/ce:title¿.

[126] Q. Wang and J. Liu. In A. Prokop, editor, *Intracellular Delivery*, volume 5 of *Fundamental Biomedical Technologies*, 567–598 (Springer Netherlands), 2011. ISBN 978-94-007-1248-5.

[127] Z. Amoozgar and Y. Yeo. *Wiley Interdisciplinary Reviews: Nanomedicine and Nanobiotechnology*, **4, 2** 219, 2012. ISSN 1939-0041.

[128] L. Lartigue, C. Innocenti, T. Kalaivani, A. Awwad, M. D. M. Sanchez Duque, Y. Guari, J. Larionova, C. Guérin, J.-L. G. Montero, V. Barragan-Montero, P. Arosio, A. Lascialfari, D. Gatteschi, and C. Sangregorio. *Journal of the American Chemical Society*, **133, 27** 10459, 2011. ISSN 1520-5126.

[129] L. Lartigue, K. Oumzil, Y. Guari, J. Larionova, C. Gue?rin, J. Montero, V. Barragan-Montero, C. Sangregorio, A. Caneschi, C. Innocenti, and Others. *Organic Letters*, **11, 14** 2992, 2009. ISSN 1523-7060.

[130] A. Boni, M. Marinone, C. Innocenti, C. Sangregorio, M. Corti, A. Lascialfari, M. Mariani, F. Orsini, G. Poletti, and M. Casula. *Journal of Physics D: Applied Physics*, **41, 13** 134021, 2008. ISSN 0022-3727.

[131] E. Kang, J.-G. Park, Y. Hwang, M. Kang, J. Park, and T. Hyeon. *The Journal of Physical Chemistry B*, **108, 37** 13932, 2004. ISSN 1520-6106.

[132] E. Fantechi, G. Campo, D. Carta, A. Corrias, C. de Julin Fernndez, D. Gatteschi, C. Innocenti, F. Pineider, F. Rugi, and C. Sangregorio. *The Journal of Physical Chemistry C*, **116, 14** 8261, 2012.

[133] M. H. Levitt. *Spin Dynamics: Basics of Nuclear Magnetic Resonance* (John Wiley & Sons), 2008.

[134] M. E. Haacke, R. W. Brown, M. R. Thompson, R. Venkatesan, M. E. Haacke, R. W. Brown, M. R. Thompson, and R. Venkatesan. *Magnetic resonance imaging : physical principles and sequence design* (Wiley), 1st edition, 1999. ISBN 0471351288.

[135] I. Solomon. *Phys. Rev.*, **99** 559, 1955.

[136] N. Bloembergen. *The Journal of Chemical Physics*, **27, 2** 572, 1957.

[137] J. H. Freed. *Journal of Medical Physics*, **68, 9** 4034, 1978.

[138] Y. Ayant, E. Belorizky, J. Aluzon, and J. Gallice. *Journal de Physique*, **36, 10** 991, 1975.

[139] Q. L. Vuong, J.-F. Berret, J. Fresnais, Y. Gossuin, and O. Sandre. *Advanced Healthcare Materials*, **1, 4** 502, 2012. ISSN 2192-2659.

[140] D. Forge, Y. Gossuin, A. Roch, S. Laurent, L. V. Elst, and R. N. Muller. *Contrast Media & Molecular Imaging*, **5, 3** 126, 2010. ISSN 1555-4317.

[141] G. M. Lanza, P. Winter, S. Caruthers, A. Schmeider, K. Crowder, A. Morawski, H. Zhang, M. J. Scott, and S. A. Wickline. *Current Pharmaceutical Biotechnology*, **5, 6** 495, 2004.

[142] M. Atri. *J Clin Oncol*, **24, 20** 3299, 2006.

[143] T. Neuberger, B. Schpf, H. Hofmann, M. Hofmann, and B. von Rechenberg. *Journal of Magnetism and Magnetic Materials*, **293, 1** 483 , 2005. ISSN 0304-8853. ¡ce:title¿Proceedings of the Fifth International Conference on Scientific and Clinical Apllications of Magnetic Carriers¡/ce:title¿.

[144] M. Cho, W.-S. Cho, M. Choi, S. J. Kim, B. S. Han, S. H. Kim, H. O. Kim, Y. Y. Sheen, and J. Jeong. *Toxicology Letters*, **189, 3** 177 , 2009. ISSN 0378-4274.

[145] G. Fontana, M. Licciardi, S. Mansueto, D. Schillaci, and G. Giammona. *Biomaterials*, **22, 21** 2857 , 2001. ISSN 0142-9612.

[146] A. S. Zahr, C. A. Davis, and M. V. Pishko. *Langmuir*, **22, 19** 8178, 2006. PMID: 16952259.

[147] S. Weitman, R. Lark, L. Coney, D. Fort, V. Frasca, V. Zurawski Jr, and B. Kamen. *Cancer Res*, **52, 12** 3396, 1992.

[148] L. Coney, A. Tomassetti, L. Carayannopoulos, V. Frasca, B. Kamen, M. Colnaghi, and V. Zurawski Jr. *Cancer Res*, **51, 22** 6125, 1991.

[149] A. C. Antony. *Blood*, **79, 11** 2807, 1992. ISSN 0006-4971.

[150] J. Alexandre, Y. Hu, W. Lu, H. Pelicano, and P. Huang. *Cancer Res*, **67, 8** 3512, 2007.

[151] R. Meier, T. Henning, S. Boddington, S. Tavri, S. Arora, G. Piontek, M. Rudelius, C. Corot, and H. Daldrup-Link. *Radiology*, **255, 2** 527, 2010.

[152] H. Cui, Y. Feng, W. Ren, T. Zeng, H. Lv, and Y. Pan. *Recent Patents on Nanotechnology*, **3, 1** 32, 2009. ISSN 1872-2105.

[153] K. L. Krycka, R. A. Booth, C. R. Hogg, Y. Ijiri, J. a. Borchers, W. C. Chen, S. M. Watson, M. Laver, T. R. Gentile, L. R. Dedon, S. Harris, J. J. Rhyne, and S. A. Majetich. *Phys. Rev. Lett.*, **104, 20** 207203, 2010. ISSN 0031-9007.

[154] E. Lima Jr, A. Brandl, A. Arelaro, and G. Goya. *J. Appl. Phys.*, **99, 4** 083908, 2006. ISSN 00218979.

[155] R. D. Desautels, E. Skoropata, and J. van Lierop. *J. Appl. Phys.*, **103, 7** 07D512, 2008. ISSN 00218979.

[156] P. Panissod. *NMR of Nanosized Magnetic Systems, Ultrathin Films, and Granular Systems, in Magnetism: Molecules to Materials III: Nanosized Magnetic Materials* (Wiley-VCH Verlag GmbH, Weinheim), 2001.

[157] N. Bloembergen, E. M. Purcell, and R. V. Pound. *Phys. Rev.*, **73, 7** 679, 1948.

[158] A. H. Morrish. *The physical principles of magnetism* (IEEE Press), 1980.

[159] T. Chatterji. *Neutron Scattering from Magnetic Materials* (Elsevier), 2005.

[160] T. Moriya. *Progress of Theoretical Physics*, **28, 2** 371, 1962.

[161] N. Noginova, T. Weaver, M. King, a. B. Bourlinos, E. P. Giannelis, and V. a. Atsarkin. *Journal of Applied Physics*, **101, 9** 09C102, 2007. ISSN 00218979.

[162] N. Noginova, T. Weaver, A. Andreyev, A. Radocea, and V. Atsarkin. *J. Phys.: Condens. Matter.*, **21, 25** 255301, 2009. ISSN 0953-8984.

[163] L.-M. Lacroix, D. Ho, and S. Sun. *Current Topics in Medicinal Chemistry*, **10, 12** 1184, 2010.

[164] S. Laurent, D. Forge, M. Port, A. Roch, C. Robic, L. Vander Elst, and R. Muller. *Chemical reviews*, **108, 6** 2064, 2008. ISSN 0009-2665.

[165] D.-E. Lee, H. Koo, I.-C. Sun, J. H. Ryu, K. Kim, and I. C. Kwon. *Chem. Soc. Rev.*, **41** 2656, 2012.

[166] R. Hergt, S. Dutz, R. Mller, and M. Zeisberger. *Journal of Physics: Condensed Matter*, **18, 38** S2919, 2006.

[167] M. Arruebo, R. Fernndez-Pacheco, M. R. Ibarra, and J. Santamara. *Nano Today*, **2, 3** 22 , 2007. ISSN 1748-0132.

[168] A. Bjrnerud and L. Johansson. *NMR in Biomedicine*, **17, 7** 465, 2004. ISSN 1099-1492.

[169] S. L. C. Pinho, S. Laurent, J. Rocha, A. Roch, M.-H. Delville, S. Mornet, L. D. Carlos, L. Vander Elst, R. N. Muller, and C. F. G. C. Geraldes. *The Journal of Physical Chemistry C*, **116, 3** 2285, 2012.

[170] L. Néel. *Annales Gophys.*, **5** 99, 1978.

[171] L. Vander Elst, A. Sessoye, S. Laurent, and R. Muller. *Helvetica chimica acta*, **88, 3** 574, 2005. ISSN 0018-019X.

[172] F. Borsa, Y. Furukawa, and A. Lascialfari. *Novel NMR and EPR Techniques*, chapter NMR in Magnetic Molecular Rings and Clusters, 297–349 (Springer (Berlin Heidelberg)), 2006.

[173] K. L. Taft, C. D. Delfs, G. C. Papaefthymiou, S. Foner, D. Gatteschi, and S. J. Lippard. *Journal of the American Chemical Society*, **116, 3** 823, 1994.

[174] A. Caneschi, A. Cornia, A. C. Fabretti, S. Foner, D. Gatteschi, R. Grandi, and L. Schenetti. *Chemistry A European Journal*, **2, 11** 1379, 1996. ISSN 1521-3765.

[175] S. P. Watton, P. Fuhrmann, L. E. Pence, S. J. Lippard, A. Caneschi, A. Cornia, and G. L. Abbati. *Angewandte Chemie*, **109, 24** 2917, 1997. ISSN 1521-3757.

[176] A. Caneschi, A. Cornia, A. C. Fabretti, and D. Gatteschi. *Angewandte Chemie*, **111, 9** 1372, 1999. ISSN 1521-3757.

[177] J. van Slageren, R. Sessoli, D. Gatteschi, A. A. Smith, M. Helliwell, R. E. P. Winpenny, A. Cornia, A.-L. Barra, A. G. M. Jansen, E. Rentschler, and G. A. Timco. *Chemistry A European Journal*, **8, 1** 277, 2002. ISSN 1521-3765.

[178] R. H. Laye, M. Murrie, S. Ochsenbein, A. R. Bell, S. J. Teat, J. Raftery, H.-U. Gdel, and E. J. L. McInnes. *Chemistry A European Journal*, **9, 24** 6215, 2003. ISSN 1521-3765.

[179] G. A. Ardizzoia, M. A. Angaroni, G. La Monica, F. Cariati, M. Moret, and N. Masciocchi. *J. Chem. Soc., Chem. Commun.*, 1021–1023, 1990.

[180] J. Schnack and M. Luban. *Phys. Rev. B*, **63** 014418, 2000.

[181] F. Troiani, M. Affronte, S. Carretta, P. Santini, and G. Amoretti. *Phys. Rev. Lett.*, **94** 190501, 2005.

[182] E. Micotti, Y. Furukawa, K. Kumagai, S. Carretta, A. Lascialfari, F. Borsa, G. A. Timco, and R. E. P. Winpenny. *Phys. Rev. Lett.*, **97, 26** 267204, 2006. ISSN 1079-7114.

[183] C. J. Wedge, G. A. Timco, E. T. Spielberg, R. E. George, F. Tuna, S. Rigby, E. J. L. McInnes, R. E. P. Winpenny, S. J. Blundell, and A. Ardavan. *Phys. Rev. Lett.*, **108** 107204, 2012.

[184] G. A. Timco, S. Carretta, F. Troiani, F. Tuna, R. J. Pritchard, C. A. Muryn, E. J. L. Mcinnes, A. Ghirri, A. Candini, P. Santini, G. Amoretti, M. Affronte, and R. E. P. Winpenny. *Nature Nanotechnology*, **4** 173, 2009.

[185] F. Troiani, A. Ghirri, M. Affronte, S. Carretta, P. Santini, G. Amoretti, S. Piligkos, G. Timco, and R. E. P. Winpenny. *Phys. Rev. Lett.*, **94** 207208, 2005.

[186] F. K. Larsen, E. J. L. McInnes, H. E. Mkami, J. Overgaard, S. Piligkos, G. Rajaraman, E. Rentschler, A. A. Smith, G. M. Smith, V. Boote, M. Jennings, G. A. Timco, and R. E. P. Winpenny. *Angewandte Chemie*, **115, 1** 105, 2003. ISSN 1521-3757.

[187] Y. Furukawa, K. Kiuchi, K.-i. Kumagai, Y. Ajiro, Y. Narumi, M. Iwaki, K. Kindo, A. Bianchi, S. Carretta, G. A. Timco, and R. E. P. Winpenny. *Phys. Rev. B*, **78** 092402, 2008.

[188] R. Caciuffo, T. Guidi, G. Amoretti, S. Carretta, E. Liviotti, P. Santini, C. Mondelli, G. Timco, C. A. Muryn, and R. E. P. Winpenny. *Phys. Rev. B*, **71** 174407, 2005.

[189] G. C. Carter, L. H. Bennet, and D. J. Kahan. *Progress in MAterial Sciece Vol. 20*, 1977.

[190] S. Carretta, P. Santini, G. Amoretti, T. Guidi, J. R. D. Copley, Y. Qiu, R. Caciuffo, G. Timco, and R. E. P. Winpenny. *Phys. Rev. Lett.*, **98** 167401, 2007.

[191] Y. Furukawa, Y. Nishisaka, K.-i. Kumagai, P. Kögerler, and F. Borsa. *Phys. Rev. B*, **75** 220402, 2007.

[192] P. Carretta and A. Lascialfari. *NMR-MRI, μSR and Mössbauer Spectroscopies in Molecular Magnets* (Springer Verlag Italia), 2007.

[193] S. Carretta, P. Santini, G. Amoretti, M. Affronte, A. Ghirri, I. Sheikin, S. Piligkos, G. Timco, and R. E. P. Winpenny. *Phys. Rev. B*, **72** 060403, 2005.

[194] S. Carretta, J. van Slageren, T. Guidi, E. Liviotti, C. Mondelli, D. Rovai, A. Cornia, A. L. Dearden, F. Carsughi, M. Affronte, C. D. Frost, R. E. P. Winpenny, D. Gatteschi, G. Amoretti, and R. Caciuffo. *Phys. Rev. B*, **67** 094405, 2003.

[195] E. Liviotti, S. Carretta, and G. Amoretti. *The Journal of Chemical Physics*, **117, 7** 3361, 2002.

[196] A. J. Freeman and R. E. Watson. In G. T. Rado and S. Suhl, editors, *Magnetism IIA* (Academic, New York), 1967.